# OBSERVATION AND STUDY OF GeV SOLAR ENERGETIC PARTICLES USING THE MILAGRITO EXTENSIVE AIR SHOWER DETECTOR

BY

Abraham Falcone

B.S., Virginia Tech (1995)
M.S., University of New Hampshire (1998)

DISSERTATION

Submitted to the University of New Hampshire
in partial fulfillment of
the requirements for the degree of

Doctor of Philosophy
in
Physics

May 2001

# DEDICATION

I'd like to dedicate this thesis to that guy over there. No, not him, the other guy standing next to him.

# ACKNOWLEDGEMENTS

The Milagro and Milagrito Observatory would not exist if it had not been for the efforts of many people. In particular, I would like to point out the extraordinary work of Scott Delay and Neil Thompson, who were technicians for the project. I am grateful for the expert knowledge that was passed on to me by many collaborators. Those that were particularly helpful with regards to this thesis were Stefan Westerhoff, David Williams, Andy Smith, Gaurang Yodh, and Rich Miller. I would like to acknowledge Todd Haines for his critical eye and helpful discussions. Also deserving of recognition are Don Coyne, Tony Shoup, and Chad Young for lending their hands during the construction of the prototype outrigger array. Morgan Wascko and Joe McCullough deserve recognition for opening their house and their beer supply to me and all the other graduate students who stayed in Los Alamos for extended, yet intermittent, times. The entire Milagro collaboration, including the students, the senior collaborators and the technicians, worked together (both in and out of harmony) to make this experiment run. They all deserve recognition.

I would like to thank my advisor, Jim Ryan, for giving me the opportunity to work on this project. While Jim did provide some direction, his manner of advising fostered an atmosphere in which I had the freedom to achieve my own successes and learn from my own mistakes. I continue to feel that this is the best way to learn. I am also grateful to the members of my committee for their useful comments.

Most importantly, I would like to thank my friends and family who have been at my side throughout this time in my life. My parents, Carl and Dorothy

Falcone, have offered support in many forms, as well as friendship, throughout my entire life. Indirectly, their wise choices during my youth helped to bring about the completion of this thesis, and I only hope that I can give to them even a small fraction of what they have given to me. My sister, Melissa Falcone, has also been at my side to offer support through many hard, yet important, times. I am also very grateful that my life and work has been enriched by the friendship and conversation that I share with Chris Lenart and Jeff Büechler. Finally, I would like thank the woman who will always share my love, Shelley Roderick, and our new son, Sequoia (who is 3 weeks old at the time of this writing). Shelley's strength, wisdom, and love has made my life immeasurably more complete and full. Sequoia, as a mere infant, has managed to inspire me in new ways so I can only imagine what he will be capable of as he grows and his individual personality develops.

# TABLE OF CONTENTS

# LIST OF FIGURES

## ABSTRACT


**OBSERVATION AND STUDY OF GeV SOLAR ENERGETIC PARTICLES USING THE MILAGRITO EXTENSIVE AIR SHOWER DETECTOR**

by

Abraham Falcone

University of New Hampshire, May, 2001

Measurements of high energy emission from solar events can lead to an understanding of the solar energetic particle acceleration mechanism(s). Although the energy source of these mechanisms is known to reside in the solar magnetic field, the details of the acceleration process(es) have continued to elude researchers. By observing the particle emission at the upper limits of the spectrum, essential information about the location and the nature of the acceleration mechanism(s) can be obtained.

Milagrito was an extensive air shower observatory which operated as a prototype for the larger Milagro instrument. It operated from February 1997 to May 1998. Although Milagrito was originally designed as a high energy (>100 GeV) water-Cherenkov gamma ray observatory, it could also be used to study solar energetic particles (SEPs). In a scaler mode, it was sensitive to muons and small showers from hadronic primary particles above ~3 GeV. Simultaneously, Milagrito also operated in a shower mode which had increased sensitivity due to its ability to reconstruct event directions, but this mode required primary particles of higher energy. In its scaler mode, Milagrito registered a ground level

enhancement associated with the 6 November 1997 SEP event and X9 solar flare. At its peak, the enhancement was 22× background RMS fluctuations. Based on comparisons to neutron monitor and satellite data, we conclude that the differential flux of energetic protons from this event followed a rigidity-power-law spectrum which became steeper above a few GeV, and that the acceleration site was at ~2 solar radii. This altitude is relatively low in the corona, but it is well above the flare site.

# CHAPTER 1

# INTRODUCTION

Early research in the field of energetic particle acceleration was carried out from a perspective defined by researchers whose experience ranged over many fields, including nuclear physics, atomic physics, astrophysics, and plasma physics (Fermi 1949). As the various fields of physics have progressed, researchers have become increasingly specialized within their respective fields. In spite of this approach, which has led to narrow fields, the natural world will not allow the links between the myriad of fields to be severed. The physics of energetic particle acceleration is one example of this. Wherever strong electric fields, shocks, or variable magnetic fields that can produce reconnection exist, energetic particle acceleration becomes likely. Thus, the mechanisms of energetic particle acceleration become important for both man-made projects such as accelerators and tokomaks and for astrophysical sites of acceleration. Energetic particle acceleration is a process common to many astrophysical sources, such as supernova remnants, active galactic nuclei, the unknown accelerators of ultra high energy cosmic rays, and the Sun. Due to its proximity, the Sun and its associated activity can be studied in far more detail than sources outside of our solar system. Therefore, by studying the Sun, we can make considerable contributions to our understanding of the general processes of particle acceleration.

In addition to providing an excellent laboratory for the study of energetic particle acceleration in a plasma environment, the Sun provides us with reasons to study it in its own right. At some level, nearly all processes on Earth receive, or have received, their energy supply from the Sun. Radiation from the Sun warms the Earth environment, affects the dynamics of Earth's atmosphere and magnetosphere, affects global weather patterns on the surface of the Earth, and buffets orbiting spacecraft with potentially damaging radiation. The extremely turbulent and complex atmosphere of the Sun creates a daunting problem for researchers to solve. Magnetic fields become twisted within the highly conductive plasma that makes up the solar environment. The dynamics of this plasma is coupled, in ways that are not well understood, with the convective motion below the visible surface of the Sun. All of these motions lead to multiple sites of explosive energy release through magnetic reconnection, shock acceleration, and / or direct electric field acceleration. Exactly how these mechanisms combine to create the observed energy releases and massive structures that extend to distances well beyond the orbit of Earth is still a young and thriving topic of study.

Most of the research that has been done on solar energetic particles has concentrated on energies below ~ 1 GeV. This is due to the fact that there are very few particles to detect at higher energies since the spectra are usually characterized by a power-law form, which drops rapidly with increasing energy. As a result of the low fluxes above ~ 1 GeV, satellites are not capable of providing the necessary effective area requirements to study transient sources. Ground-based detectors, which utilize the ability of the Earth's atmosphere to interact with incident particles, are required to observe these very high energy

particles. Although these high energy particles are poorly studied, it is in this energy regime that some of the most interesting and important research can be done since it is here that the limits of the acceleration mechanism/s are tested. Milagro is, and Milagrito was, capable of observing particles in this poorly sampled energy region, thus spanning the gap defined by satellites and neutron monitors on the low energy end and traditional extended air shower arrays on the upper energy end. Milagrito was sensitive to particles from ~5 GeV to several TeV, and its effective area was ~3 orders of magnitude greater than that of a neutron monitor at 10 GeV. This places Milagrito in an excellent position to explore the limits of the acceleration mechanisms and to search for the existence of an energy cutoff in the SEP spectrum.

# CHAPTER 2

# SOLAR PHYSICS OVERVIEW

## Characteristics of the Quiet Sun

The Sun is a massive (~$2\times10^{30}$ kg) sphere of hot, gaseous plasma with a thermonuclear fusion reactor in its core and an atmosphere permeated by a large-scale, turbulent magnetic field that is coupled to the plasma dynamics. Thus, it is easy to see why this ordinary type G2 star is extremely active and dynamic. Before going into the detail of some of these dynamics, it should be useful to outline some of the features of the "quiet Sun."

The interior of the Sun is generally considered to be the region below the visible surface, which is the relatively thin layer referred to as the photosphere. From the center of the Sun to about $0.25R_{Sun}$ is the core, which has an average temperature of ~$1.5\times10^{7}$ K and an average density of ~$1.6\times10^{5}$ kg $m^{-3}$. These conditions allow fusion to take place, converting the abundant (~90%) hydrogen to helium, positrons, neutrinos, and gamma radiation. At the basic level, this process provides all of the energy necessary for the myriad of solar processes to take place, while providing a constant flux of radiation, and it provides the pressure required to support the mass of the Sun. As one proceeds to higher radii, the radiative zone of the Sun extends from the edge of the core up to its

boundary with the convective zone at ~0.86 $R_{Sun}$. In the radiative zone, the primary means of energy transport is through radiative diffusion, while in the convective zone, energy is transported primarily by means of convective instabilities. As bulk quantities of plasma rise to the surface of the convective zone and give off their heat before falling back down to be reheated at lower depths, the scene is set for the dynamic nature of the coupled solar magnetic field. Above the convective zone, lies the photosphere at a temperature of ~6000 K. By the time the gamma rays from the core have reached the photosphere they have been absorbed and emitted so many times that they have taken ~$10^7$ years to complete their journey, which would have taken ~2 seconds in the absence of interactions. As a result of this journey, these photons are shifted to the visible realm of the spectrum, thus we observe the visible light that comes from the region we call the photosphere.

The photosphere of the Sun, the layer from which most of the observed wavelengths of light are emitted, is only ~500 km thick. As a result of this thinness, the Sun appears to have a well-defined edge, in spite of its gaseous state. When one observes the Sun at different wavelengths, a different depth is observed. Viewed at visible wavelengths, the photosphere appears to be dotted by cells at a variety of scales. These cells, which range from granulation to super granulation to giant cells, are thought to be a result of the processes occurring in the underlying convection zone. At the photosphere, the temperature has dropped to about 6000 K, which is a fall in excess of three orders of magnitude from the core temperature. The effective temperature of the Sun, if it is considered to be a blackbody, is ~5785 K.

Beyond the photosphere, the temperature of the Sun begins to rise as one proceeds radially outward. The upper boundary of the photosphere is commonly defined as the radial distance at which the solar temperature hits its minimum. The mechanism by which the layers above the photosphere are heated is not well understood. Most solutions to this problem, known as "coronal heating," involve the release of energy through resonant waves and dynamics of the solar magnetic field. Above the photosphere lies the chromosphere, which is ~2000 km thick. This layer is visible in a variety of lines, such as Hα and Ca II, and granulation can be observed throughout this region. The temperature rises with radial distance in the chromosphere, and in a region referred to as the transition region, the temperature increases rapidly before it begins to level off in the next layer known as the corona. At the lower boundary of the corona, the temperature has reached nearly $10^7$ K, while the density has decreased by many orders of magnitude to a value of ~$10^{-11}$ kg $m^{-3}$.

The corona is a vast layer of the Sun that extends far beyond Earth to the unknown distance (maybe ~80 AU) at which solar system material meets interstellar material. So, in a sense, the Earth is immersed within the outer layer of the Sun. The corona can be observed during eclipses when the moon blocks out the bright central light of the Sun that would otherwise outshine the low-density, high-temperature coronal material emission. This view can be artificially achieved through the use of a coronagraph, which is a telescope with an occulting disc used to block out the bright photospheric light. Coronagraphs have been operated on the ground, such as that at Mauna Loa, as well as in space such as those flown on board Skylab, SMM, and more recently SOHO. When one observes the corona, many structures are found to be present. Prominences

of bright higher density plasma can be seen extending out from the low corona for many solar radii. These prominences can remain stable for several solar rotations, or they can erupt into massive transient events that extend for many AU in the corona. Streams of dense plasma can also be observed to flow outward from the Sun through the corona. Regions of relatively low density can also be observed in X-rays as dark areas in the low corona. These regions, referred to as coronal holes, tend to occur near the polar regions of the Sun. While many solar features, such as coronal holes, persist as 'non-transient' structures for long periods of time, their structure and properties do vary over timescales in excess of years. This will be explained more thoroughly in the discussion of the solar cycle.

## The Solar Wind and Plasma Motions

When looking at the motion of charged particles in the solar environment, it is important to understand the interaction between motions in a highly conductive plasma and the magnetic field. When bulk motions of plasma occur, the magnetic field will be dragged along with the plasma. Similarly, motions of the magnetic field lines will affect the plasma. This positive feedback relationship can be quantified by looking at Ohm's Law along with a suitable combination of Maxwell's equations. One can start with the generalized Ohm's Law and apply Faraday's Law, Ampere's Law, and the divergence equation.

After combining the generalized Ohm's Law, $\vec{J} = \sigma_0\left(\vec{E} + \vec{V} \times \vec{B}\right)$, and Faraday's Law, $\nabla \times \vec{E} = -\frac{\partial \vec{B}}{\partial t}$, one obtains:

$$\frac{\partial \vec{B}}{\partial t} = \nabla \times \left( \vec{V} \times \vec{B} - \vec{J} \big/ \sigma_0 \right).$$

From this, one can apply Ampere's Law and the divergence equation to obtain:

$$\frac{\partial \vec{B}}{\partial t} = \nabla \times \left(\vec{V} \times \vec{B}\right) + \frac{1}{\sigma_0 \mu_0} \nabla^2 \vec{B}$$

From this equation, it is evident that the magnetic field can vary through bulk motions of the plasma with the first term on the right hand side (RHS) of the equation, and **B** can vary through diffusion defined by the second term on the RHS. If $\sigma_0 \to \infty$ or the characteristic length scale becomes large, then the second term on the RHS approaches zero. When these conditions hold in a collisionless, cold plasma, then the magnetic field is considered to be "frozen in" to the plasma.

In addition to considering bulk plasma dynamics in the presence of a magnetic field, one can consider the effect of the magnetic field on individual charged particles. Charged particles with gyroradii significantly less than the characteristic length scale tend to remain bound to the field line they are on, in the absence of collisions and cross-field drifts. This effect is a result of the Lorentz force, which tends to bind charged particles into a helical orbit about the field line they are on. One can speak of the connection of a particular point in space to another point in space as a result of the tracing of one field line through these points. Thus, for a charged particle, the path from the Sun to the Earth is determined by the magnetic field geometry, unlike the path for neutral particles which can travel directly along the line of site. For charged particles with very

large gyro radii, such as cosmic rays whose kinetic energies exceed many GeV, this effect becomes negligible as the particles are no longer "confined" by the magnetic field.

It was once thought that the solar corona was a static atmosphere of the Sun (Chapman 1957), but it is now understood that there is a "wind" of plasma that blows radially throughout the corona. The model for this wind and the associated solar magnetic field was initially introduced by Parker (1958), although the concept of continuous streams of plasma emission from the Sun was proposed earlier (Biermann 1951). Parker modeled the solar coronal environment as a spherically symmetric isothermal plasma acted on by a pressure gradient and the gravitational field. The model could correctly predict the pressure and density in the solar corona, unlike the static atmosphere model, and it qualitatively produced the velocity distribution of the solar wind. Later models would incorporate higher order effects to obtain a quantitative solution for the velocity distribution. Additionally, Parker's model led to a picture of the solar magnetic field, known as the "Parker Spiral," which is considered to be the standard today. Observations of comet tails provided early evidence for the solar wind, and recent observations of the wind properties have been carried out by the Ulysses spacecraft.

The solar wind blows approximately radially from the Sun at an average velocity of ~450 km / s. The plasma that comprises this wind is composed of mostly hydrogen ions and electrons, although many other ions are present in small quantities including ~3% ionized helium. The solar wind is usually separated into the fast stream and the slow stream. The fast wind comes primarily from coronal holes, which contain an array of open field lines (i.e. field

lines that extend far out into the corona before turning back in on themselves as any finite universe without monopoles requires). The slow wind, which tends to flow at speeds less than ~450 km/s, flows primarily from the lower latitudes where there are more field lines in loop structures. Given the typical coronal densities and the typical coronal **B** field strength of ~5-10 nT, it is evident that the solar wind speed is generally both supersonic and super-Alfvenic, where the Alfven speed is defined by $V_A = B/(4\pi\rho)^{1/2}$.

It is the presence of the solar wind and the rotation of the Sun that makes the geometry of the background solar interplanetary magnetic field (IMF) so interesting. As the solar wind transports plasma radially outward from the Sun,

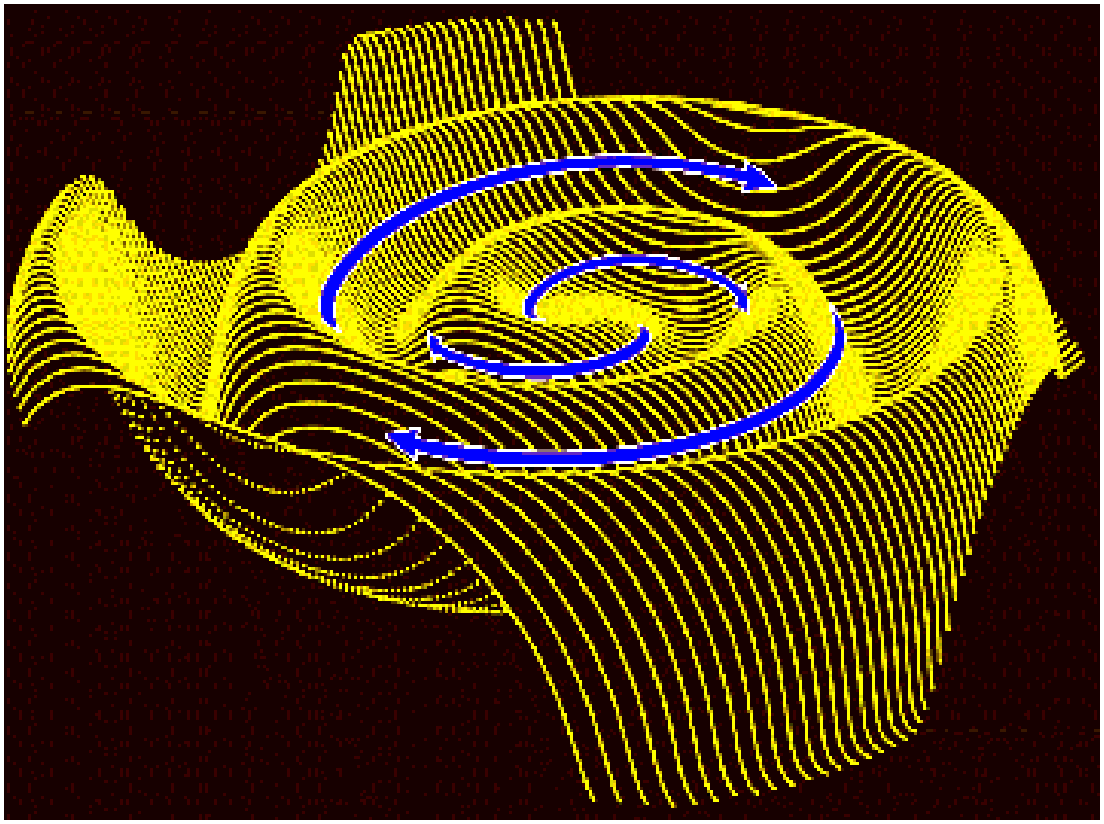

Figure 2.1 - Schematic diagram of magnetic field structure in the heliosphere. Magnetic field lines extend outward from the Sun in an Archimedean spiral form. The wavy "ballerina skirt" plane defines the neutral current sheet that separates the north and the south solar **B**.

the magnetic field geometry is also transported with it due to the fact that the **B** field is frozen into the highly conductive plasma. The **B** field lines, which are effectively attached to the surface of the Sun, are then curved as a result of the rotation of the Sun about its axis within the radially expanding plasma. This curvature, which is illustrated in **figure 2.1**,takes the form of an Archimedean spiral, which is referred to as the Parker Spiral. Under quiet conditions, this leads to the ambient IMF being tilted at an angle of ~45 degrees at 1 AU. This feature of the IMF is important when one considers the path that charged particles traverse from the Sun to the Earth. Since the charged particles prefer to travel along magnetic field lines, they do not necessarily travel along the line of site that is traveled by photons from the Sun. For example, a proton whose gyro radius is much less than 1 AU and is emitted from the center of the Sun may travel in a curved path that does not intersect the Earth, while a proton with the same gyroradius emitted from the west limb of the Sun may travel along the spiral curve that brings it to Earth. This will also lead to a path length in excess of the naively expected distance of 1 AU, thus the travel time will be correspondingly longer.

## The Solar Cycle

Some of the most exciting properties of the Sun are its multiple forms of transient activity. Solar flares are evident on the surface of the Sun when viewed at a variety of wavelengths including visible, radio, and gamma ray. Sunspots, which are cooler than the surrounding photospheric plasma (**figure 2.2**), come

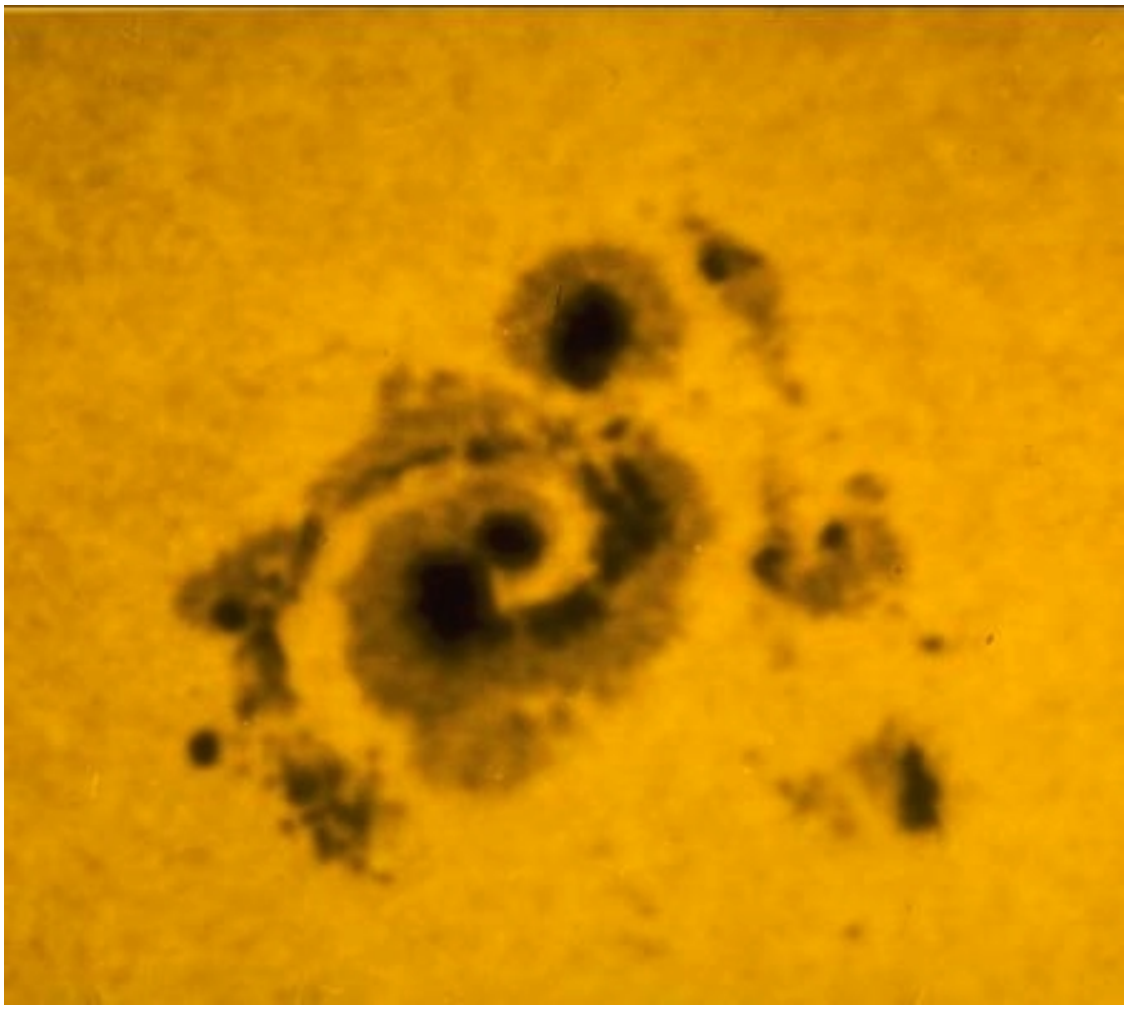

Figure 2.2 - Example of a group of sunspots on the solar photosphere.

and go throughout the photosphere as a result of magnetic flux tubes emerging from below the photosphere. Networks of sunspots also exhibit fluctuations. Huge amounts of plasma are launched from the Sun when coronal mass ejections launch themselves into space. Ribbons and plages can be observed moving along the surface of the Sun, while filaments can be observed in the low corona, sometimes erupting into the outer corona. All of these processes come and go on different timescales, but there are some recurrent timescales that persist.

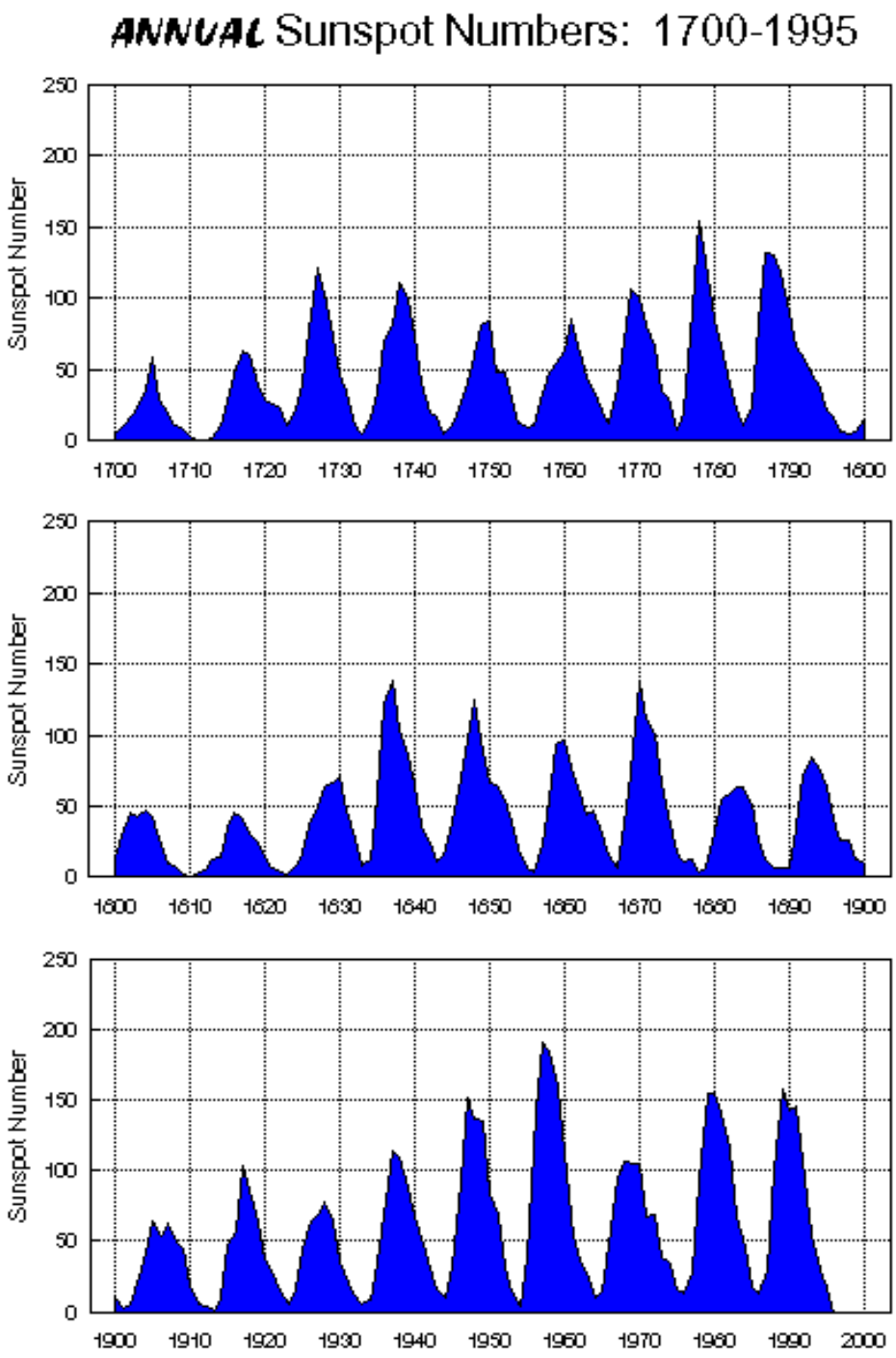


Figure 2.3 - Sunspot number as a function of time. (Figure courtesy of Nat. Geophys. Data Center.

The Sun exhibits an 11 year cycle of activity. This cycle can be tracked in a variety of ways, but the most traditional method is to record the number of

sunspots on the surface (**figure 2.3**). The number that is generally recorded is the Wolf sunspot number, which combines the number of sunspots, s, and the number of sunspot groups, g, into one number using the following relationship: $R_W = K(10s+g)$, where K is a factor used to correct for observer and instrumental differences. The number of sunspots exhibited by the Sun is a good indicator of magnetic activity, which is linked to nearly all, if not all, forms of activity on the Sun. For instance, as the sunspot number increases, the frequency and magnitude of flares also increases. From **figure 2.4**, which is referred to as a "butterfly diagram," it is also evident that the range of solar latitudes at which active regions appear varies with the solar cycle. During an 11 year period, the frequency of sunspots and solar activity progresses from a minimum to a maximum and back down to a minimum value. During this 11 year period, the solar magnetic field reverses its polarity, as do the sunspots seen on the surface. Since the following 11 year period will see another reversal of the magnetic field back to its prior orientation, it is apparent that the 11 year cycle is actually a subcycle of the longer cycle that has a 22 year period. It has been proposed that there are other longer periods to the cycle of solar activity.

In addition to these longer period cycles of solar activity, there is the more obvious cycle due to the rotation of the Sun. Since the Sun is not a solid body, it exhibits differential rotation. In the equatorial regions, the Sun rotates with an apparent period of ~27 days, while at the poles, the rotation period is ~37 days. (It is interesting to note that sunspots rotate a bit faster. This is probably due to the fact that the emerging flux is anchored to regions below the photosphere that are rotating faster than the overlying material.) Due to this rotation, active regions of the Sun are in constant motion. An observer at the Earth may see

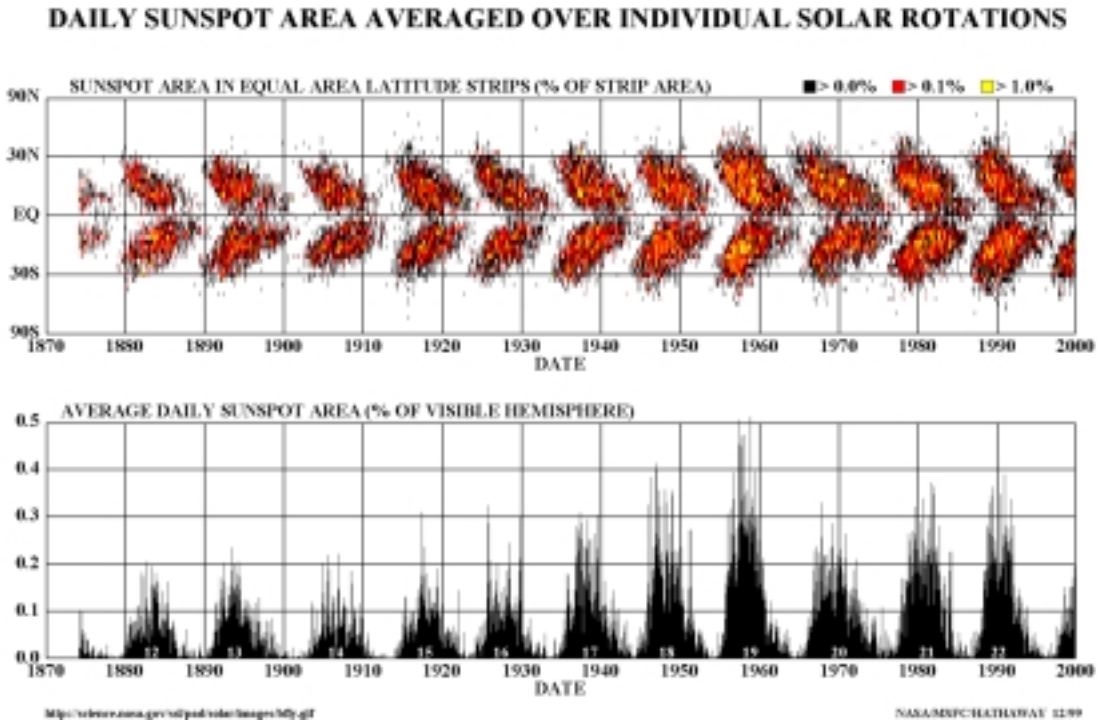


Figure 2.4 - Locations of solar activity regions as a function of solar cycle time. (Graph courtesy of Hathaway at NASA-MSFC)

emission from a flare that subsequently rotates to the backside of the Sun. This active region may still be present when it rotates back into view after ~2 weeks. For some forms of emission, this relationship is not quite that simple since some interactions can occur above the limb and charged particles can travel from the backside of the Sun along the IMF.

## CMEs and Flares

Although the processes that lead to increased energy release during the peak of the solar cycle arise from a variety of mechanisms, not all of which are well understood, the solar magnetic field provides the basis for many common features and correlations. The exact mechanisms that lead to the acceleration of

particles and ejection of matter are frequently debated, but nearly all mechanisms require a release of energy stored in the solar magnetic field. It was demonstrated as early as 1957 that only the solar magnetic field had the energy to accelerate observed fluxes and energies of particles from the February 1956 event (Parker 1957). Furthermore, all of the mechanisms must take place within the ambient solar **B** field, and any charged energetic particles must move through the spiral structure of the solar **B** field, while obeying the laws of a highly conductive plasma in an extended magnetic field. It is easy to see why these processes of energy release, which have many overlapping properties, were frequently assigned incorrect cause and effect relationships in the history of the field.

During no other transient solar process, do we see such a dramatic energy release as that observed during a coronal mass ejection (CME). CMEs can eject > $10^{13}$ kg of mass at speeds ranging from 10 km / s to > 2000 km / s. This equates to a kinetic energy release that can be > $4 \times 10^{32}$ erg simply to lift the material out of the gravitational field of the Sun. An example of a CME observed by the coronograph on the Solar Maximum Mission (SMM) is shown in **figure 2.5**. During this process, initially closed field lines that are frozen into the ejected plasma are stretched out into the corona. One can observe the bulky bright features of these events extending out for many solar radii during an eclipse or with the aid of a coronograph. After several days, the plasma from the coronal mass ejection can travel past the Earth, sometimes creating disturbances of the geomagnetic field, and it may continue to propogate for many AU.

While solar flares and coronal mass ejections (CMEs) are both well known processes by which energy is released in the form of energetic particles, and / or

radiation, it is the solar flare phenomena that received the most attention during the early years of research in the field. This was primarily a result of the fact that evidence for solar energetic particles (SEPs) preceded the observation of CMEs by many years (Forbush 1946), whereas the flares had already been known to exist. This historical situation led to an inaccurate view of the respective roles played by flares and CMEs, which is only beginning to dissipate today. In 1859, Carrington observed a visible brightening on the surface of the Sun, now known as a white-light flare (Carrington 1860). It was further noted that a large geomagnetic storm occurred within a day of this flare. In the following years, more observations of solar flares were made (Hale 1931, Newton 1943, Hudson &

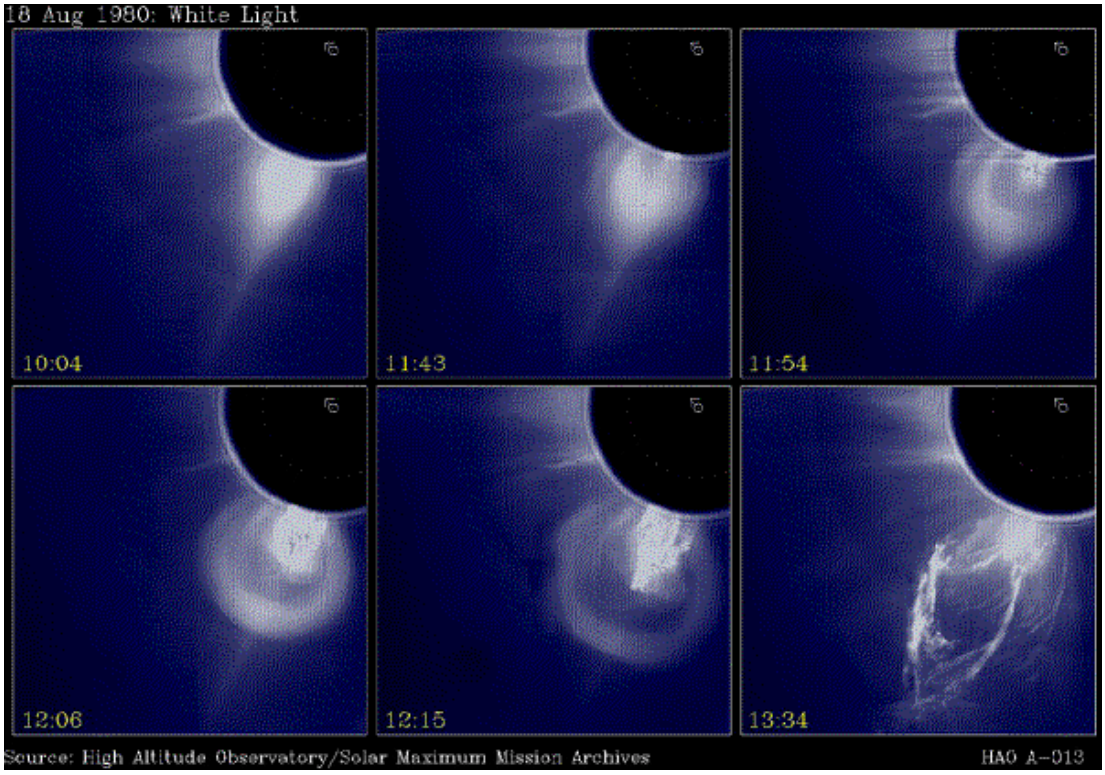


Figure 2.5 - Series of coronograph images that track the launch of a CME that ocurred on 18 August 1980. These white light images wre obtained with a coronograph of the Solar Maximum Mission. (Images courtesy of HAO)

Ryan 1995). Some of these flares were accompanied by what appeared to be associated geomagnetic storms., while others were not. It was suggested (Hale 1931, Chapman 1950) that the geomagnetic storms accompanying flares were caused by streams of plasma, which were emitted from the solar flares, that interacted with Earth's magnetic field. This idea dominated most of the ensuing research in the field of solar eruptive energy release until very recently.

The paradigm shift from considering solar flares to be the prime accelerators of large energetic particle events to placing coronal mass ejections in a more prominent role began when Kahler et al. (1978, 1984) and Cliver et al. (Cliver 1983) began looking at the correlations between SEP events, flares, and CMEs. It was found that there was a high correlation (~96%) between large SEP events and CMEs, while these events were not well correlated with X-ray flares. This also implies another shift that was occurring. It had previously been thought that CMEs were launched by solar flares, but this was certainly not true since many CMEs did not have any associated solar flare. The development of this so called "solar flare myth" has been outlined by Gosling (1993) and Reames (1999). Based on observations of SEP abundances and ionization states, as well as associations between and spatial distributions of the various solar processes, the role of CMEs in the heliosphere is beginning to be understood. Two key points have been realized. CMEs can, and do, occur independently of solar flares, and CMEs, not flares, are the dominant cause of the highest energy SEP events.

Coronal mass ejections can occur in conjunction with solar flares, but this is not always the case. The early belief was that hard X-ray events at the Sun were required for effective proton acceleration (Lin & Hudson 1976), but it was

found by Cliver et al. (1983) that this was not the case when he studied proton acceleration from "weak" impulsive events. It has also been thought in the past that long duration soft X-ray flares were the drivers for both SEPs and CMEs. Work by Pallavicini et al. (1977) on flares separated soft X-ray events into two categories, designated inpulsive and long-duration, and the long duration events were subsequently asociated with CMEs. While observations by Sheeley et al. (1975) using Skylab and the SOLRAD spacecraft suggest that all long duration (> 4.5 hours) soft X-ray flares are accompanied by a CME, the CMEs that have no associated flare activity must also be considered. It has been found that only ~ 1/3 of CMEs occur in conjunction with long duration soft X-ray flares (Gosling 1993, Sheeley et al. 1975, Sheeley et al. 1983). It should be expected that some flaring activity will be associated with CMEs since both processes involve reconfigurations of the solar magnetic field. As the CME launches, by whatever mechanism, one should expect field lines to get twisted and reconnected and for new loops to be formed. So, it seems natural to observe some associations, as has been found, but to stretch these mild associations to the point of a cause and effect relationship is unjustified based on current observations.

## Gradual and Impulsive SEP Events

It was noticed by Kahler et al. (1978, 1987) that there was a 96% correlation between large SEP events and CMEs. This was the first major evidence that coronal mass ejections were the driver of what would later be called gradual SEPs.

SEP events are generally separated into two generic categories that are referred to as "gradual" events and "impulsive" events. The nomenclature is actually related to the historical association of the events with gradual and impulsive flares, but in some respects it is still applicable. Gradual events tend to have energetic particle flux time profiles that rise above background and then exhibit a broad peak that may last for days. In contrast, impulsive events tend to have time profiles that are sharply peaked, although they may take days to actually reach pre-event flux levels. Two relatively "pure" examples of these two types of events can be seen in **figure 2.6** (Reames 1999).

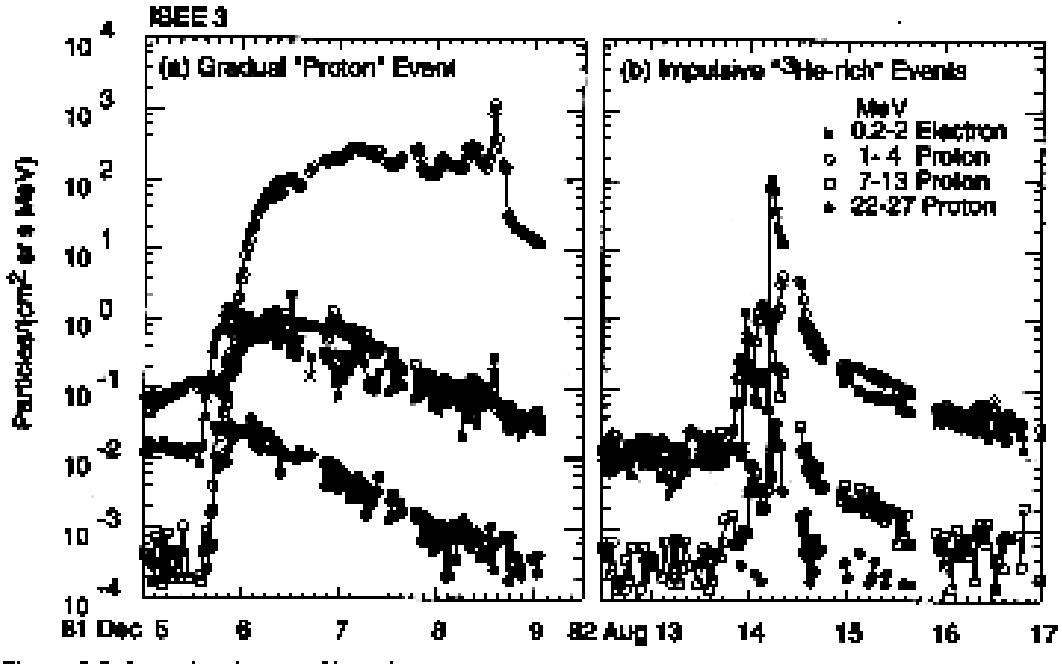


Figure 2.6 - Example of a model gradual SEP event is shown in the left panel, while an example of a model impulsive SEP event is shown in the right panel. The gradual event was associated with a CME and a filament, with no impulsive flare. The impulsive event was from flaring with no associated CME. (Reames 1999)

The larger and more energetic events usually fall into the gradual event category. These are the events that can be observed at ground-based stations, such as neutron monitors, that require protons to exceed several GeV in order to

pass through the Earth's magnetic field. Gradual events generally exhibit greater fluxes of SEPs over long time scales. They also tend to be associated with long-duration type II/IV radio emission. Type II metric radio emission is indicative of plasma emission from coronal shocks, while the associated type IV emission is usually associated with electron gyrosynchrotron or plasma emission from well within the CME (Robinson et al. 1986, Kahler 1992). Gradual events are also associated with fast moving (>400 km/s) CMEs that are capable of driving shocks in front of the mass of plasma. The SEP abundances and ionization states during gradual events are characteristic of coronal values, and low electron-to-ion ratios are generally present.

Impulsive events typically exhibit smaller fluxes of SEPs over shorter time scales. They also tend to be associated with large electron-to-ion ratios and enhancements in heavy ions and $^3$He relative to coronal values. For instance, a typical value for $^3$He/$^4$He during an impulsive event is ~1, while the $^3$He/$^4$He ratio for gradual events is usually < 0.01. These ionization states and abundances are indicative of a lower source region for the accelerated ions from impulsive events. Another interesting feature of impulsive versus gradual events is indicated by their longitudinal distribution, shown in **figure 2.7**. Although the error is large due to the difficulty in determining source locations of the extended structure of a CME, it is evident that gradual events can originate from anywhere across the solar disk, while impulsive events observed at Earth must originate at western longitudes. This is presumably due to a requirement upon impulsive SEPs that they originate on a field line that is well connected to the Earth-based observer. This also implies a lower corona or photospheric origin and more point-like nature of the acceleration mechanism for impulsive SEPs.

Fast (v>400 km/s) CME driven interplanetary (i.e. coronal) shocks are generally thought to be the acceleration mechanism for the gradual events (Lee 1997, Kahler 1992), while the impulsive events are frequently thought to originate at, or near, a flare site (Reames 1999). The general line of thinking is that CMEs drive a shock wave in front of the mass of plasma. This shock is capable of accelerating particles throughout the corona. Thus, it is not surprising that fast CMEs (>450 km/s) are far more likely to accelerate particles to high energies. It is also not surprising that the abundances observed for gradual SEP events are representative of coronal abundances, rather than photospheric abundances as one would expect from acceleration at the site of a flare. Studies by Cliver (1996) have suggested that the distinction between the two classes of events is fuzzier than previously thought. Cliver has painted a picture that includes a class of events that are a hybrid of impulsive and gradual SEP events.

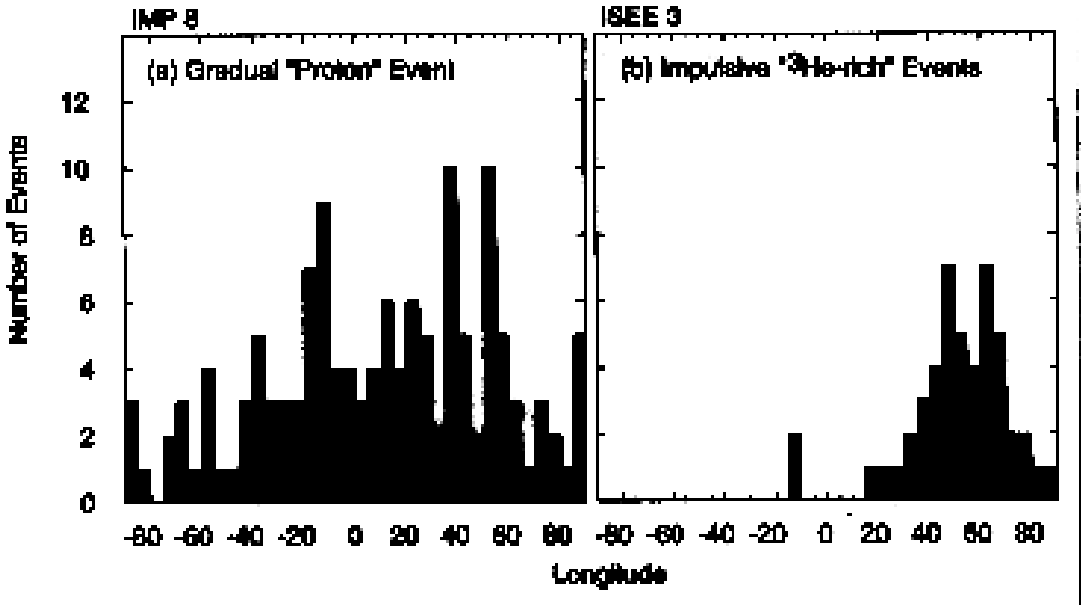


Figure 2.7 - Histograms of the longitudes of the solar active regions associated with gradual SEP events (left panel) and impulsive SEP events (right panel). (Reames 1999)

This picture may also blur the distinction between SEP acceleration mechanisms and the locations of the particle acceleration.

## Shock Acceleration by CMEs

Shocks are thought to accelerate energetic particles from several sources throughout the heliosphere. At the shock front where the fast solar wind overtakes the slow solar wind, particles are accelerated in the so called corotating interaction region. Anomalous cosmic rays are thought to be the result of acceleration at the heliospheric termination shock of ions that enter the heliosphere from interstellar space and are subsequently transported back to the termination shock by the solar wind. Particles are also accelerated in the low corona by solar flares and CMEs, and shocks play a role in many of these proposed processes. Most pertinent to this work are the particles that are thought to be accelerated in interplanetary space by fast shocks driven by CMEs moving at velocities in excess of the ambient solar wind.

Diffusive shock acceleration at fast shocks driven by a CME is presently considered by many researchers to be the mechanism by which SEPs from gradual events are accelerated (Lee 1997, Reames 1999, Kahler 1992). In this model, the ions gain energy whenever they traverse the shock. Multiple shock traversals are necessary to reach the observed energies, particularly for the GeV ions observed by ground-based detectors such as Milagrito and neutron monitors. In order to traverse the shock many times, efficient scattering must be achievable. This scattering occurs to some degree as a result of the irregularities

of the magnetic field, but it is also thought that much of this scattering is from resonant waves. These waves can be excited by the low energy particles, thus increasing their acceleration potential in a recursive process on up to GeV energies (Reames 1999).

Injection energy at the shock will also play an important role in the ability of the shock to accelerate particles to GeV energies. The solar atmosphere is a dynamic region, and it is not uncommon for several events to occur within days of each other during periods of high solar activity. It is obviously easier for a shock to accelerate a proton from 100 MeV to 10 GeV than it is to accelerate a proton of 1 MeV to 10 GeV. This can be seen in a blast wave shock model produced by Lee and Ryan (1986), for which acceleration times for a variety of injection energies are calculated. Although this model does not take into account the driving mechanism of the CME, it is sufficient to illustrate the dependence on injection energy.

One should expect there to be a cutoff in the energy spectrum of shock accelerated particles. This cutoff should arise as a result of physical constraints such as finite size, finite time and number of shock traversals, and available injection energies. Currently, observations with neutron monitors above a few GeV seem to show a gradual softening (i.e. rollover of the spectrum) of the power-law spectrum relative to satellite measurements at lower energies. This is in agreement with current theory, but one might expect to see the cutoff in the spectrum at energies just above several GeV. The sensitivity of neutron monitors has not been sufficient enough to allow for an unambiguous detection of this proposed spectral cutoff.

During the days when the solar flare myth dominated, the typical method used in the transport models for the gradual SEP events was that of diffusion in the heliosphere. Many of these events were observed to have isotropic distributions. Particles had been observed to come from solar flare events that had no apparent field-line connection to the Earth-based observatories that measured intensity increases, but this did not daunt the modelers. Diffusion theories were incorporated to allow the particles to diffuse along magnetic field lines sufficiently to explain the observations. This contrived model is not necessary, and probably not correct, now that it is understood that CMEs are the primary accelerators of gradual SEP events. Based on SMM observations, the distribution of the apparent angular widths of CMEs peaks between 40 and 50 degrees and extends to > 120 degrees (Hundhausen 1999). Thus, the shocks that are driven by these broad structures and the CME associated magnetic field geometry extend over many degrees, as well. Coronal diffusion models are no longer necessary.

## Solar Modulation of Cosmic Rays

Interplanetary space is filled with charged particles called cosmic rays, which will be described in the following chapter. When these charged particles move through the heliosphere, they must interact with the ambient magnetic field and the local plasma. This fact leads to a variation of the intensity of the observed cosmic ray flux. This effect is known as solar modulation. This modulation of cosmic rays has been observed to vary with the solar cycle, as

shown in **figure 2.8**. This figure displays an anticorrelation between the solar cycle and the local intensity of cosmic ray flux. An anticorrelation of the cosmic ray intensity can also be seen when it is compared to the aa index, which is a measure of geomagnetic activity that is correlated with solar activity. As solar activity increases, magnetic turbulence and solar wind velocity also increase. Thus, the cosmic rays that enter the heliosphere must overcome the barrier that is presented to them by the local magnetic field. If the gyroradii of the cosmic rays

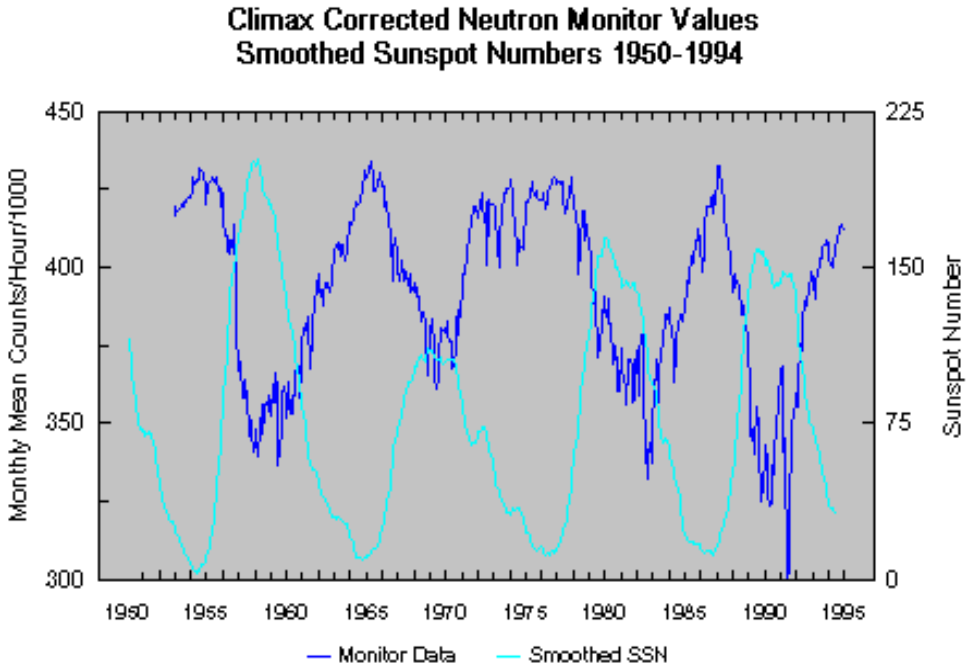


Figure 2.8 - The lower curve is the smoothed sunspot number over the past four solar cycles. The other curve is a measure of the local cosmic ray intensity above a few GeV based on the monthly count rate at the Climax neutron monitor. An anticorrelation due to solar modulation of cosmic rays is evident. (Courtesy of Univ. of Chicago and Nat. Geophys. Data Center)

are significantly smaller than the distances over which they travel, then their trajectory will be affected by the magnetic field. Above ~10 GeV/nuc, this modulation effect becomes small.

In addition to the long timescale solar modulation of cosmic rays described above, there are also shorter timescale variations of cosmic ray

intensity due to solar activity. One can simultaneously glean information about the interplanetary magnetic field and the CME structure by observing the decrease in cosmic ray intensity associated with the passage of a CME. These decreases of cosmic ray intensity are known as "Forbush decreases" (Forbush 1946). They occur due to the fact that cosmic rays below a particular rigidity are partially "shielded" by the closed magnetic field structure of the CME. The observation of these events has, in fact, been used as evidence for the closed magnetic field structure of CMEs, rather than the open structure that was postulated by some early theorists. As the large-scale magnetic field structure of a CME passes the Earth, decreases in cosmic ray intensity can be observed in ground-level detectors. These Forbush decreases tend to last hours, and typically occur after the passage of the CME shock front.

# CHAPTER 3

# COSMIC RAYS AND EXTENSIVE AIR SHOWERS

## Cosmic Rays

In 1912 Victor Hess ascended through the atmosphere in a balloon and measured the ionization of the atmosphere as a function of altitude, thus recording the first evidence for radiation from extraterrestrial sources (Hess 1913). Initially this radiation, which was dubbed "cosmic rays" by Millikan in 1925, was thought to be due to some exotic form of gamma radiation that had an increased penetration depth from that observed previously. It was not until 1929 that the charged particle nature of this radiation was realized. In subsequent work, Auger (1939) indirectly measured cosmic ray particles at the highest energies by observing the shower particles created when the cosmic rays interact with atmospheric material. Simpson (1948) also carried out pioneering work on the nucleonic component of these showers. His work led to the development of the neutron monitor network, which has been used extensively for studies of solar cosmic rays in the GeV energy regime. Since these times, much has been learned from and about cosmic rays and their sources, but several important problems remain unsolved.

## Composition

In the energy range observed by satellites (i.e. below ~1 GeV), cosmic rays are almost entirely composed of protons and higher Z ions. Protons make up ~85% of observed cosmic rays, He ions contribute ~12%, and higher Z ions contribute ~1%. The remaining 2% comes from electrons. In **figure 3.1** the abundances of cosmic ray nuclei relative to those of the solar system are shown. A review of these data is available by Simpson (1983). There is a remarkable

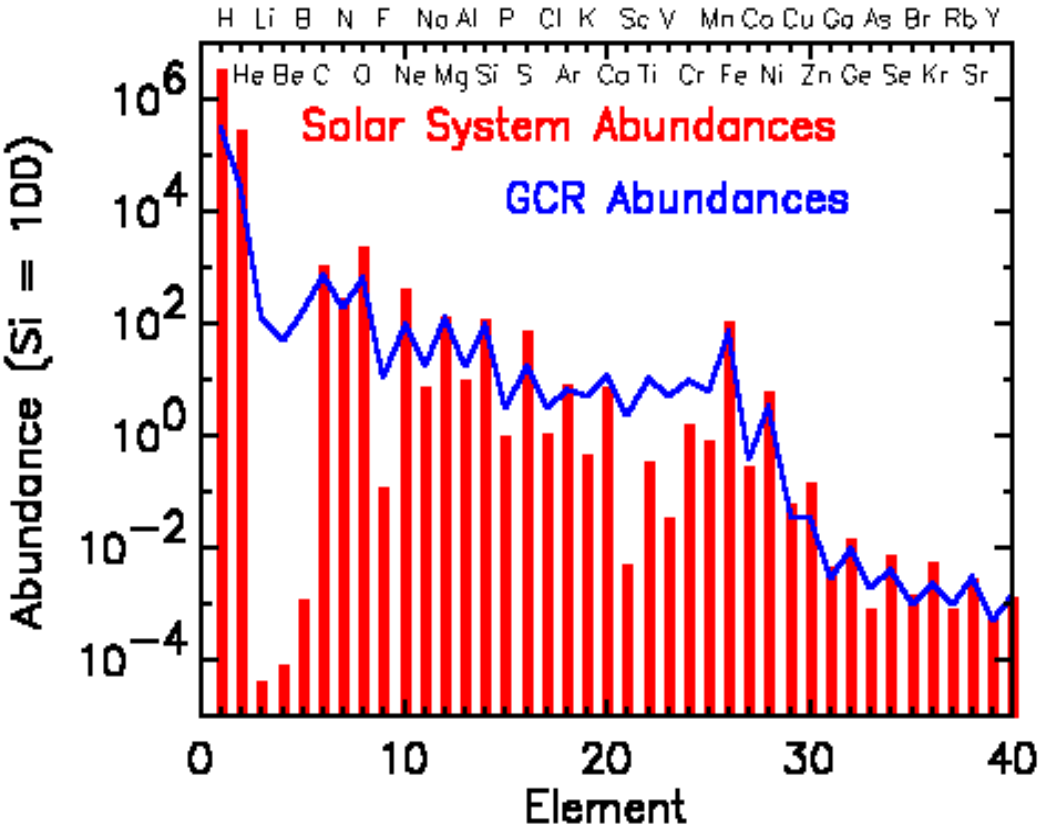


Figure 3.1 - Comparison of observed cosmic ray abundances (curve) to the solar system abundances (histogram) of elements. Abundances have been normalized to silicon.

correlation between the chemical abundances present locally and those of the cosmic rays, but there are also some striking differences. In particular, there is an obvious overabundance of Li, Be, and B, as well as for several elements immediately below Fe. These cosmic ray elemental overabundances are thought to be due to spallation reactions between primary cosmic rays and ambient interstellar gas (Weber 1983, Longair 1992).

## Spectrum

One of the most remarkable properties of cosmic rays is the continuity of the observed spectra. The energy spectrum of cosmic ray protons is shown in **figure 3.2**. The differential intensity spectrum is well fit by a single power law extending from ~$5\times10^{9}$ eV to $3\times10^{15}$ eV. For cosmic ray protons, the spectrum takes the form : $I = C\times E(GeV)^{-2.7}$ [particles $m^{-2}$ $s^{-1}$ $sr^{-1}$ $GeV^{-1}$]. The observations of cosmic ray nuclei at Earth follow this power law closely over six orders of magnitude. Below a few GeV / nucleon, the spectrum is significantly influenced by solar modulation. Solar activity, with its associated magnetic turbulence, tends to "bend" the cosmic rays propagating through the interplanetary medium. This causes the spectrum of cosmic rays to rollover below a few GeV / nucleon. Above ~$3\times10^{15}$ eV, the cosmic ray spectrum follows a softer power law of the form: $I = C\times E(GeV)^{-3.1}$ [particles $m^{-2}$ $s^{-1}$ $sr^{-1}$ $GeV^{-1}$]. The region where the spectrum takes this downward turn is referred to as the "knee" of the spectrum. This form, with the spectral index of ~3.1, describes the observed spectrum up to ~$10^{19}$ eV. Above ~$10^{19}$ eV, the spectrum appears to flatten out, thus this region has been

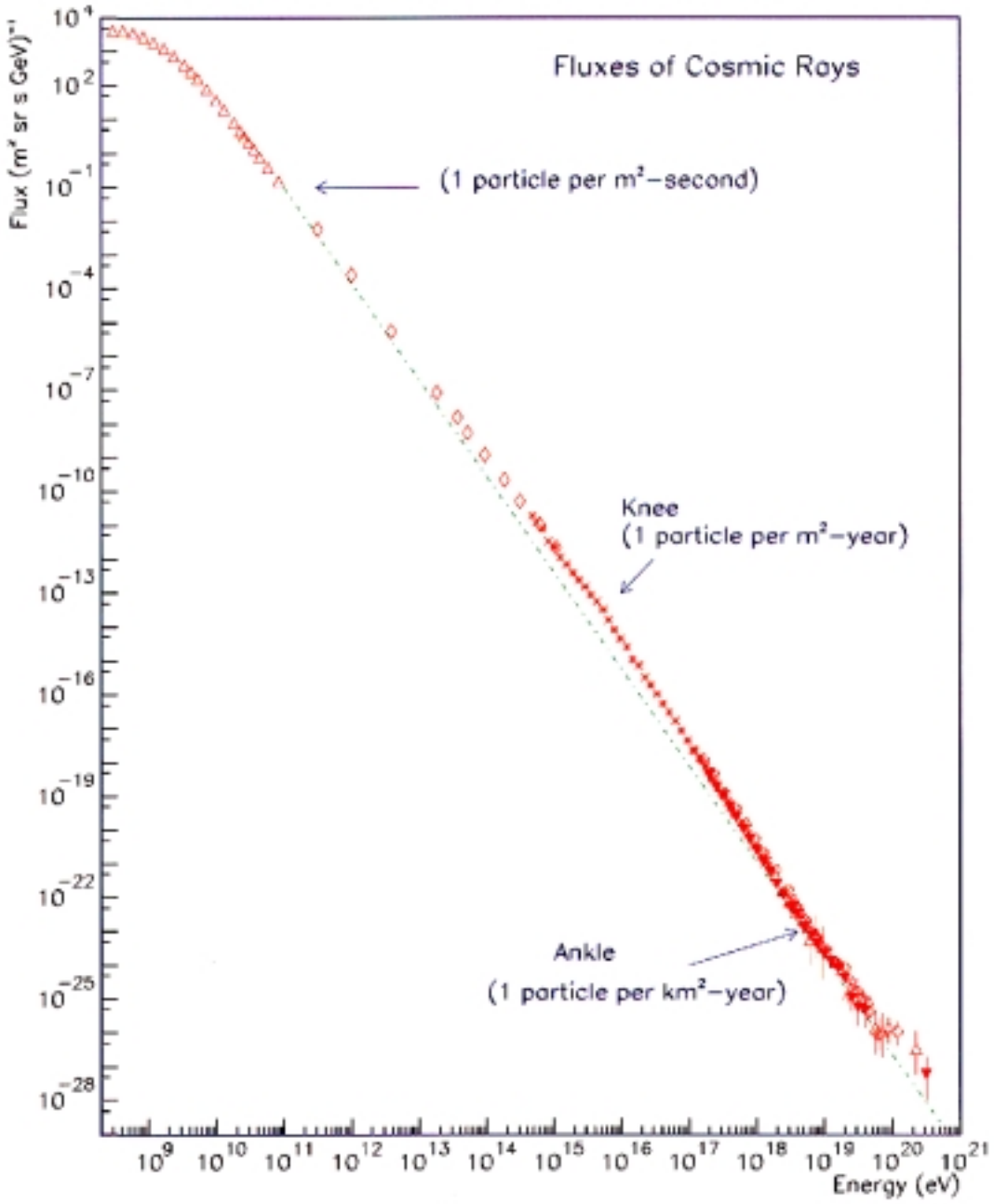


Figure 3.2 - Differential flux spectrum of cosmic ray protons over more than twelve orders of magnitude. A power law fits the spectrum well. Below ~10 GeV the effects of modulation can be seen. The spectral steepening at ~$10^{15}$ eV is also evident.

dubbed the "foot" of the cosmic ray spectrum. The error bars are large in this region due to the small number of detected particles, so the true nature of the spectrum in this region is still a lively topic of research at this time.

## Sources

There are several known sources of cosmic rays, and there is at least one unknown source of cosmic rays. Among the cosmic ray populations with known sources are anomalous cosmic rays (ACRs) and solar cosmic rays, while galactic cosmic rays (GCRs) have several source candidates. Solar cosmic rays are the energetic particles of direct solar origin, such as those accelerated by interplanetary shocks and at flare sites, that were discussed in the previous chapter. The dominant contribution to the cosmic ray spectrum comes from what are commonly referred to as the GCRs. As the name implies, these cosmic rays are widely believed to originate within our galaxy. Acceleration mechanisms involving fast shocks within supernova remnants are generally incorporated to explain the observed power law energy spectrum. This is probably the dominant source of cosmic rays below ~$10^{15}$-$10^{17}$ eV.

Below ~60 MeV, there is a turn up in the spectrum of $^{4}$He. These cosmic rays, which have been dubbed ACRs, are now understood to be accelerated in the outer heliosphere. It was noticed that the flux of these particles increases with increasing distance from the Sun. The flux of these particles was also subject to the effects of solar modulation, as was indicated by their 11-year periodicity that inversely followed that of solar activity. The general idea for the acceleration of these ACRs is that they are a result of interstellar neutral particles that enter the heliosphere, get turned around by the solar wind after being

ionized, and are subsequently accelerated at the heliospheric termination shock (Cummings & Stone 1998).

The total flux of particles above ~$10^{17}$ eV, referred to as ultra high energy cosmic rays (UHECRs), is insignificant relative to that of the GCRs, but the importance of understanding the acceleration mechanism/s of these particles cannot be understated. The source of these particles is still unknown, although there are numerous theories. Some theories consider sources for these UHECRs in the local super cluster of galaxies or in the galactic plane, while other theories consider exotic mechanisms such as cosmic string annihilation. The difficulty lies in the process of explaining the deposition of such a massive amount of energy into one single particle. It is difficult to explain the high energy of these particles if they are accelerated by some diffusive mechanism within the galaxy since charged particles above ~$10^{15}$ eV are not effectively trapped by the galactic magnetic field. This results in a situation in which multiple scatterings from magnetic field irregularities are rare. Furthermore, if these particles are extragalactic, they must propagate through the extragalactic medium, where they should interact with background 2.7 K microwaves. This photo-pion production interaction with the relic background microwaves should lead to an attenuation of the cosmic ray flux above ~$5\times10^{19}$ eV, referred to as the GZK cutoff (Greisen 1966, Zatsepin & Kuzmin 1966). The observations of the spectrum do not indicate such a cutoff, but the data is still too sparse to draw any conclusions.

## Distribution

The angular distribution of GCRs has been well studied. Below ~$10^{15}$ eV, the distribution is relatively isotropic, with the degree of anisotropy $\delta \sim 0.001$ as shown by Linsley (1983). This should be expected since ions with kinetic energy below ~$10^{15}$ eV tend to travel along the magnetic field structure of the galaxy, thus they are subject to multiple scatterings due to irregularities in the field geometry. At higher energies, the directions of the particles can also be measured using the extensive air shower techniques that will be discussed more later, but the small flux does not provide good statistics on the anisotropy measurements. The trend does seem to show an increase in anisotropy as the energy of the cosmic ray is increased, but this is not well determined. Additionally, there is some evidence, with questionable statistics, for clusters of two or three events from the same region (Medina-Tanco 2001). Although some researchers analysis seem to indicate that the anisotropy of the UHECRs points towards the local supercluster of galaxies and / or towards the galactic plane, the results are not clear due to the sparse number of detections available for statistical analysis.

## Air Showers

Above ~1-10 GeV, satellite-based detectors are no longer efficient at detecting the flux of cosmic rays. This is a result of two factors. The fast, power-law decline in the cosmic ray spectrum provides very few particles to detect, and

the practical aspects of launching satellites into space does not allow for the launch of large area detectors. There is, however, an alternative to deploying massive detectors in space. The atmosphere of the Earth can be, and has been, used as an effective detector of primary cosmic rays that collide with particles in the atmosphere and produce cascades of particles. This cascade of particles produced by high energy primary particles is referred to as an extensive air shower (EAS). Work on this was pioneered by Auger (1939) when he detected coincidences of less than 1 μs in detectors spread out over hundreds of meters at ground level. He correctly concluded that he was detecting air shower particles from cosmic ray primaries with energies in excess of $10^{15}$ eV. So, to detect cosmic rays with energies in excess of those observable by satellite-based detectors, one can use ground-based detectors that can register signals from the secondary cascade particles of the EAS initiated by the primary cosmic ray.

## Development in Atmosphere

EASs propagate to ground level in a manner defined by the characteristics of the atmosphere and the primary cosmic ray, thus one can use the observed properties of the EAS in the atmosphere and at ground level to deduce characteristics about the initiating primary particle. EASs develop when a primary cosmic ray has enough energy (~ 1 GeV) to initiate multiple pion production **(see figure 3.3)**. These pions are then free to continue the cascade in a manner dependent upon the charge of the pion, while the scattered primary particle will continue to interact if it retains enough energy. Neutral pions that

are produced will decay into gamma rays, which may subsequently pair produce. The resulting electrons and positrons can then produce high energy gamma rays through the Bremsstrahlung process, thus completing one of many

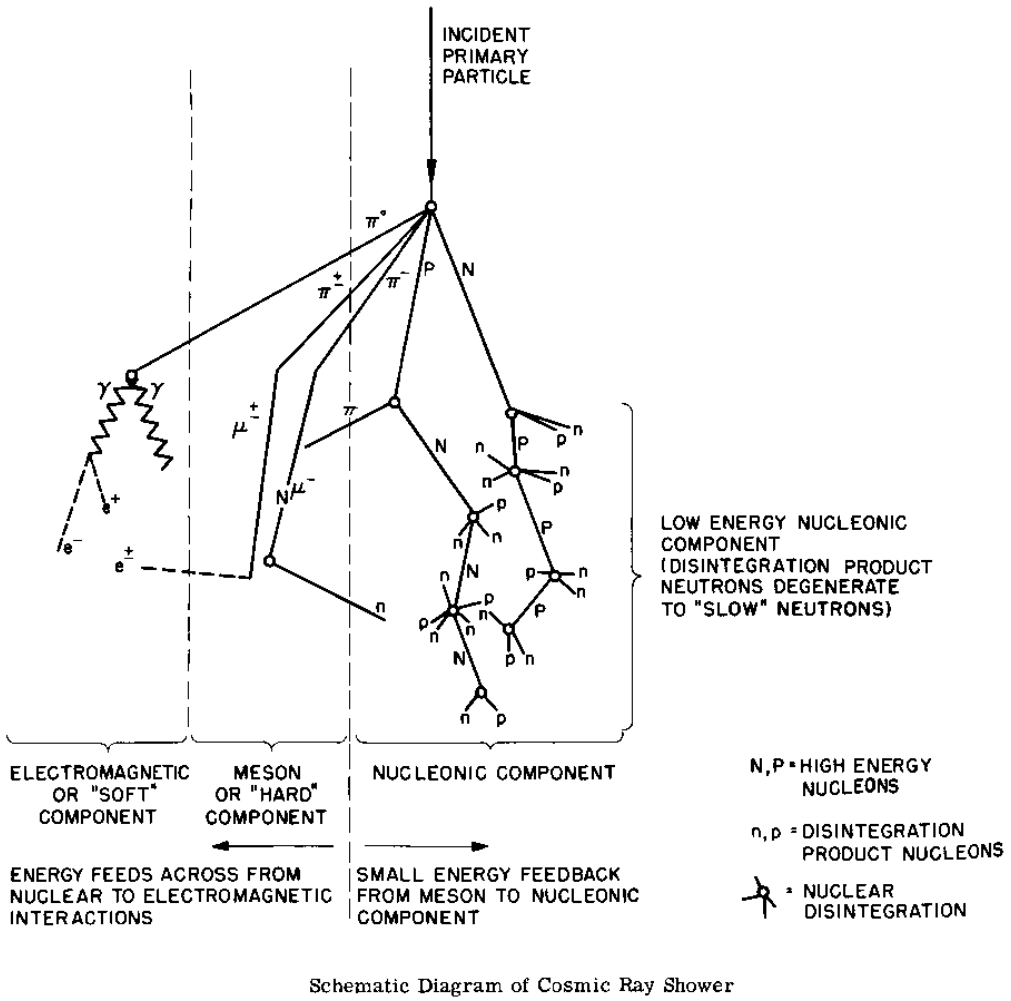


Schematic Diagram of Cosmic Ray Shower

Figure 3.3 - Develoment of a nucleonic cascade cosmic ray shower. (courtesy of J. Simpson, Univ. of Chicago)

cycles of an electromagnetic cascade. The charged pions that are produced may decay into muons, electrons, and neutrinos, by means of the reactions listed below:

$\pi^+ \rightarrow \mu^+ + \nu_\mu$

$\pi^- \rightarrow \mu^- + \text{anti-}\nu_\mu$

$\mu^+ \rightarrow e^+ + \nu_e + \text{anti-}\nu_\mu$

$\mu^- \rightarrow e^- + \text{anti-}\nu_e + \nu_\mu$

Some of the high energy muons have enough penetrating power to reach the ground-level with no further reactions, while others decay into electrons, positrons, neutrinos, and anti-neutrinos. Charged air shower particles that are travelling faster than $c/n_{air}$ will also produce photons through the Cherenkov emission process, which will be discussed in more detail in chapter 4. As this series of interactions continues the particles will lose energy through ionization and reactions. As long as enough energy remains for the propagation of the shower and the production of additional cascade particles, the shower will continue down to lower levels of the atmosphere until it ultimately reaches ground level.

The maximum number of particles produced in the EAS and the distribution of particles as a function of depth in the atmosphere are related to the energy of the initiating primary particle. Primary particles of higher energy will penetrate farther into the atmosphere before initiating their first interaction, and they will eventually produce far more total shower particles (see **figure 3.4** ) A useful rule of thumb is that the energy of the primary particle is approximately (to within ~25%) equal to the total number of particles at shower maximum multiplied by 1.4 GeV (Longair 1992). One can also observe, as should be expected for a primary with a higher mean free path, that the depth of shower

maximum will occur farther into the atmosphere for a higher energy primary particle.

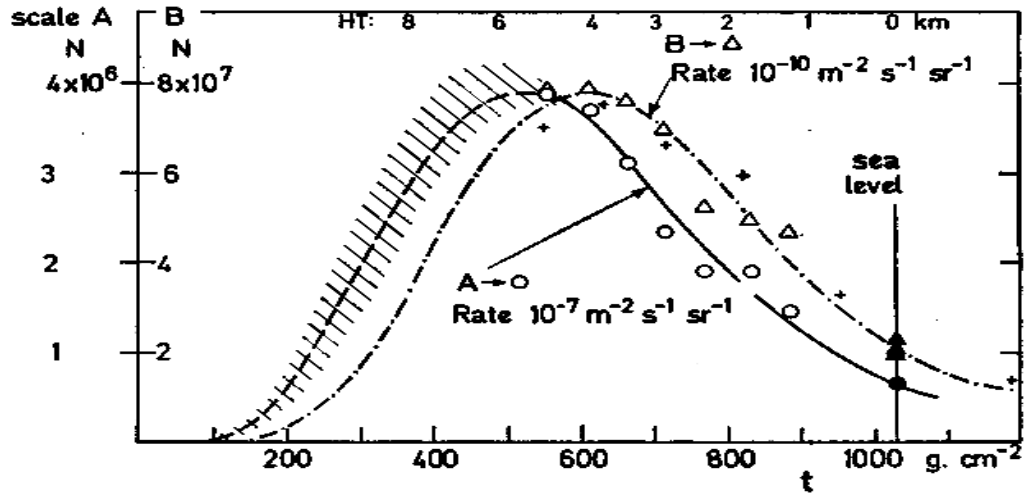


Figure 3.4 - The number of shower particles present as a function of depth in the atmosphere for two different showers. Shower A on the left has an estimated total energy of ~$5.6\times10^{15}$ eV and has ~$3.9\times10^{6}$ particles in the shower at maximum development. Shower B, the curve to the right, has an estimated total energy of ~$11.3\times10^{16}$ eV and has ~$7.8\times10^{7}$ particles in the shower at maximum development. The extension of the curves below 5200 kg $m^{-2}$ is based upon theoretical calculations. (Hillas 1972)

As a result of the various interaction timescales and mean free paths, the fractional composition of the myriad of particles produced in the EAS is a function of altitude. This can be seen for the major constituents of the EAS in **figure 3.5**. On a side note, one can see from this figure, as well as **figure 3.4** that it is advantageous to place detectors of EAS particles at high altitude since shower maximum typically occurs many kilometers above sea level. It is evident that most of the energy at ground level is in the form of muons, while most of the energy at the altitude of shower maximum is in the form of electrons.

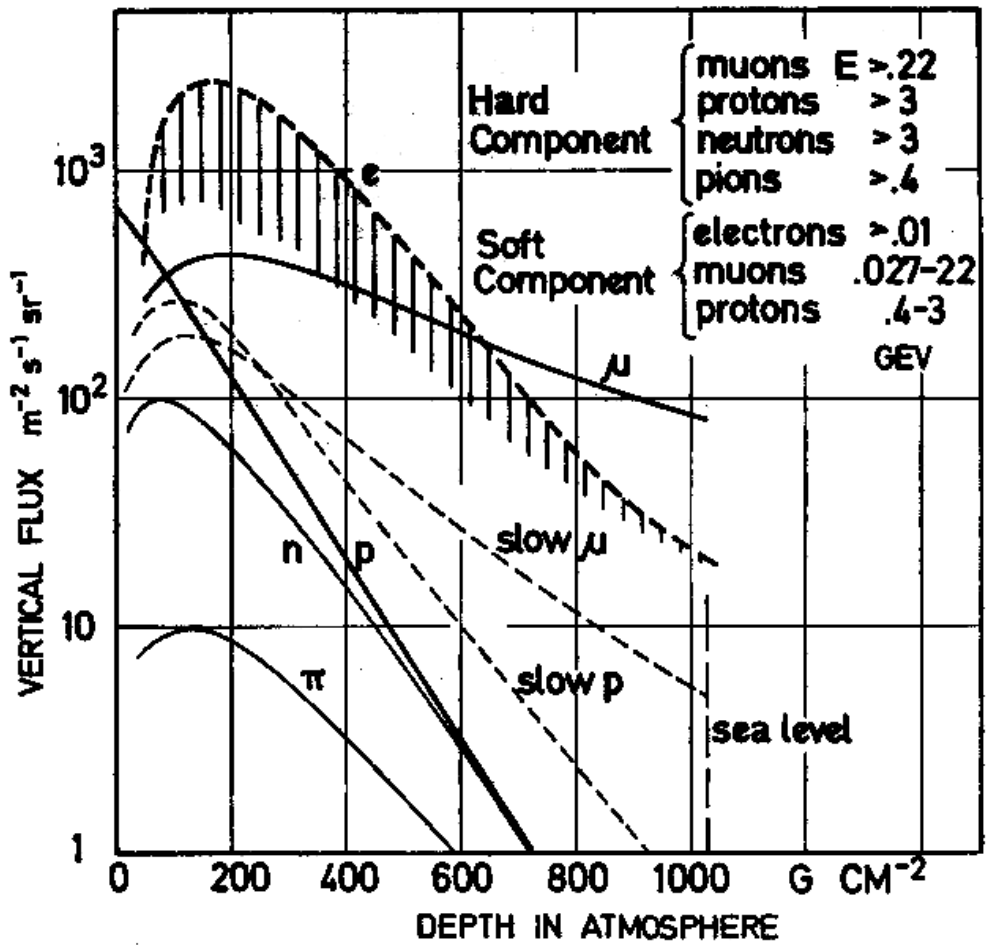


Figure 3.5 - Vertical flux of air shower particles of a nucleonic cascade as a function of atmospheric depth. (Hillas 1972)

The secondary and higher order particles of the EAS tend to move through the atmosphere as a relatively uniform, thin front. This is referred to as the "pancake" structure of the shower. Typically, this pancake has a thickness of several meters. The lighter particles will generally arrive first in a thin pancake of ~1-2 meters, while the muons may arrive in a pancake with a thickness up to ~4 meters. The more massive hadrons may trail behind the initial shower front by a few meters. The shower front is not actually a perfectly flat pancake. Showers have some curvature, which is a function of energy. This curvature is a result of the increased scattering experienced by lower energy shower particles. As a result of the increased scattering, these particles have a longer flight path.

As one moves laterally away from the core of the shower, a delay in the arrival time of the shower particles can be observed.

The lateral extent of the shower is determined primarily by the amount of transverse momentum that is transferred to the shower particles. The lateral extent of the electron-photon cascades, as well as the transverse scattering of muons, contribute significantly to the lateral size of the shower. In particular,

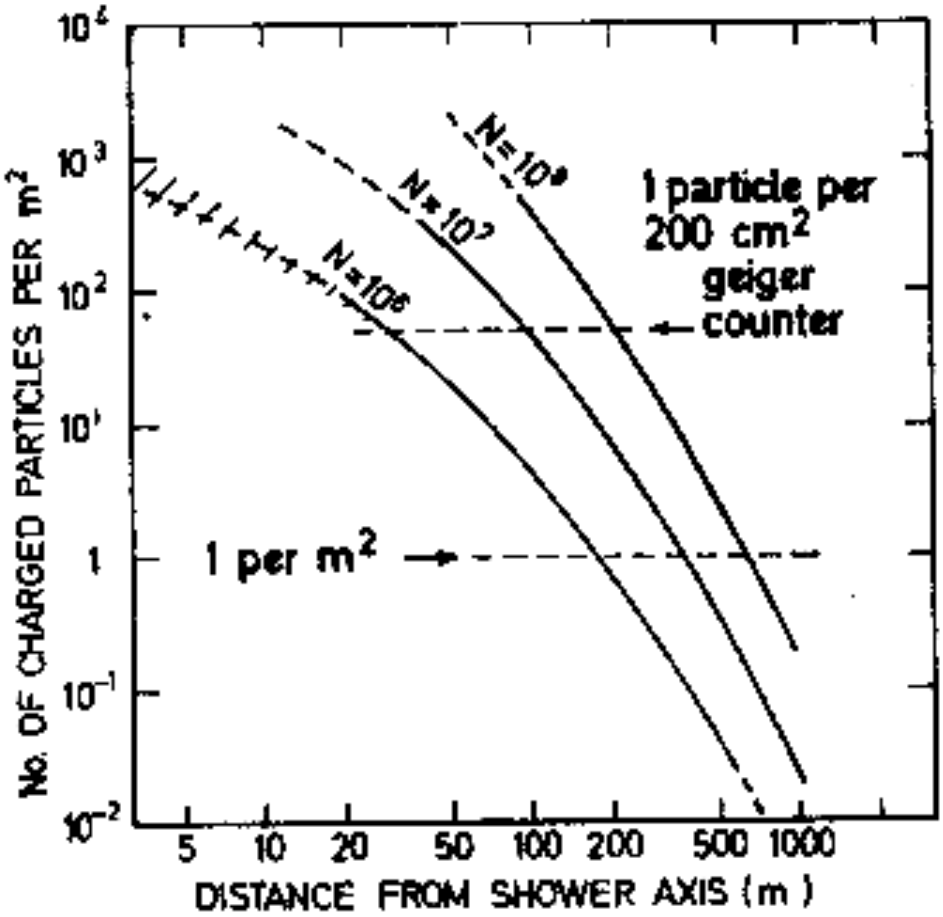


Figure 3.6 - The lateral extent of a typical EAS can be seen in these plots of shower particle flux density as a function of distance from the shower core. The three curves corrsepond to three independent showers of different numbers of particles at shower maximum. (Hillas 1972)

muons may be scattered by as much as ~3 degrees. For the electromagnetic cascade portion of air showers, the photons are scattered to large angles more than the electrons and positrons. The lateral extent of the shower, which is a function of the total number of particles in the shower, can reach distances many kilometers from the core of the shower (**see figure 3.6)**, but the particle density is much larger close to the core of the shower.

## Gamma Ray Initiated Showers

So far, this discussion has concentrated primarily on atmospheric showers produced by hadronic primary particles, but gamma rays also induce showers in the atmosphere. This is important to our discussion for two major reasons. First of all, it is desirable to distinguish between the two types of showers if one is trying to study only one of the populations of astrophysical particles. This does not present nearly as much of a problem for cosmic ray physics as it does for gamma ray physics, since the cosmic rays contribute dominantly to the flux. Thus, for gamma ray air shower physics, it is extremely important to utilize a technique for distinguishing the gamma ray induced showers from the more numerous cosmic ray showers. The second reason to consider gamma ray induced showers is that many of the same physics principles and detection techniques are used for both gamma ray and cosmic ray air shower observations.

One of the most important and distinguishing features of gamma ray showers is their lack of muons relative to cosmic ray induced showers. Although there is a small probability for muon production in high energy gamma ray

initiated showers, the cross sections for these processes are several orders of magnitude smaller than the cross section for pair production (Aid et al. 1995). A gamma ray initiated shower is almost entirely an electromagnetic shower that is comprised of electrons, positrons, and photons, whereas cosmic ray induced showers have many muons as a result of pion decay. Another related feature is the fact that a cosmic ray shower will be "clumpier" as a result of the non-uniform mini-particle-showers and the penetrating muons that propagate to the ground, while the electromagnetic cascade will develop in a relatively uniform manner. This absence of muons in electromagnetic showers and, as well as the penetrating characteristics and clumpiness of muons from hadron induced showers, can be used to separate cosmic ray showers from gamma ray showers.

## Air Shower Detection Instruments

There are several techniques that are used to detect air showers and to characterize their primary particles. In some cases, the air shower particles are detected directly, while other instruments utilize indirect methods that detect signatures of the air shower. Some of these techniques are concerned primarily with observing gamma rays over the cosmic ray background, while others are designed for the purpose of detecting cosmic ray induced showers.

## Air Fluorescence

One interesting technique that has been used to observe the highest energy cosmic rays is the air fluorescence technique. By observing the fluorescence light emitted when the relativistic electrons of the air shower excite molecules in the atmosphere, one can infer properties of the initiating primary particle. At shower maximum, electrons are the most abundant particles in the shower. By measuring the energy loss of the relativistic electrons of the shower, one can obtain an estimate for the energy of the shower. In addition to the

Figure 3.7 - Mirrors of the Fly's Eye air fluorescence detector, which are each viewed by an array of PMTs, can be pointed in a variety of directions in the sky. In this way, the development of the air shower is imaged. (Picture courtesy of HiRes collaboration)

energy estimate, this technique allows one to obtain an absolute lower limit to the energy of the shower based on the integrated energy. The Fly's Eye cosmic

ray detector, located at the Dugway Proving Grounds in Utah (**figure 3.7**), has successfully utilized the air fluorescence technique to detect > $10^{20}$ eV primary particles, with one event estimated to have an energy of ~$4\times10^{20}$ eV. This instrument utilized multiple telescopes that detected the optical fluorescence emission from a shower. In this way, the geometry of the shower development could be determined, and a measurement of the propagation direction could be obtained. HiRes, which is the next generation air fluorescence instrument, has recently been constructed in Utah.

## Air Cherenkov Telescopes

Air Cherenkov telescopes (ACTs) are actually designed to measure gamma rays in the TeV regime, rather than cosmic rays. Nevertheless, it makes sense to mention them here since they are related to Milagrito in this way. Both Milagrito and ACTs were designed to measure gamma radiation, but they are both dominated by the cosmic ray background. ACTs detect the optical Cherenkov light emitted by the relativistic air shower particles as they move through the atmosphere (Cherenkov light will be discussed in the next chapter). This is done by focusing the Cherenkov light, which is incident on one or more mirrors, onto PMTs with fast readout systems. The image on the focal plane of the reflecting mirrors can be analyzed to determine information such as shower energy and direction of incidence.

Background reduction is a primary concern for ACTs. Cosmic rays provide a large source of background. This is dealt with by applying some

gamma-hadron separation based on observed shower properties, such as lateral spread and muon content. For point sources, it can also be dealt with by imaging the shower direction accurately since cosmic rays are a relatively isotropic source. Angular resolution of ACTs can be as good as ~0.1˚. Another source of

Figure 3.8 - The Whipple Imaging Air Cherenkov Telescope. (Picture Courtesy of Whipple Collaboration)

background for ACTs are off-source gamma rays. ACTs are limited to operating on dark, moonless nights, and they must limit their field of view in order to minimize background contributions. Fast readout electronics (<10-20 ns), such

as flash-ADCs, are desirable in order to minimize the background signal that is present even on dark nights.

The leader in the field of ACTs has been the Whipple telescope (**figure 3.8**). This 10 meter instrument is located in southern Arizona at an altitude of 2300 m. It operates with a threshold of ~200 GeV, has a field of view of ~3.5˚, and has a resolution of ~0.2˚ (Weekes 1996, Weekes et al. 1989). Since the development of this technique by T. Weekes and collaborators, many more detectors have been built. Summaries of instruments and observations are available in reviews by Hoffman et al. (1999), Ong (1998), and Cronin et al. (1993). The next generation of ACTs is on its way with the proposed construction of Veritas. Veritas will be an array of 10 meter telescopes, including the present Whipple telescope.

## Extended Air Shower Arrays

Traditional EAS arrays are instruments that incorporate many detectors spread over a large area at ground level. By detecting shower particles at the ground, both gamma ray and hadronic cosmic ray primaries can be reconstructed. EAS arrays are typically spread over large areas so they do not sample a large fraction of the shower particles (typically < 1%). This generally leads to a high threshold energy (> 1 TeV). The Tibet array, which has a relatively low threshold due to its relatively dense detector spacing, has a peak trigger energy of ~2 TeV. This array is composed of 109 detectors spread over an area of 5000 $m^2$. In contrast, the Cygnus array operated from 1986 to 1996 with a

peak trigger energy of ~50 TeV and was comprised of 204 detectors spread over an area of 86000 $m^2$. In order to maximize the potential signal, it is favorable to locate EAS arrays as close to shower maximum as possible. This translates to high mountain altitudes, which can present practical problems such as accessibility. Due to the pancake-like structure of air showers, EAS arrays are capable of reconstructing the primary particle direction. By using the timing difference from one detector to another, the plane of the shower front can be reconstructed, thus the primary particle direction is determined.

Currently, there are several EAS arrays operating, including the HEGRA array in the Canary Islands, the Tibet array, and the AGASA array in Japan. For a list of many of these arrays, refer to a review article by Hoffman et al. (1999). A new large array, Auger, will probably be constructed soon. The plans for this array, which will be sensitive to the highest energy showers, include two separate arrays that will each consist of 1600 detectors spread over 3000 $km^2$.

## Neutron Monitors

Neutron monitors have made many contributions to the fields of solar energetic particles and cosmic ray physics. The concept of the neutron monitor and its initial design can be credited to J. Simpson (Simpson 1948, Simpson 1957). Based on studies of the latitude variation of the secondary nucleonic component of cosmic ray induced showers, Simpson devised a technique for detecting primary cosmic ray protons above ~1 GeV and primary neutrons above ~500 MeV. His basic design, which is referred to as an IGY (international geophysical

year was 1957/1958) neutron monitor was later expanded into the larger NM64 neutron monitor (Carmichael 1964). The basic design of the neutron monitor consists of tubes containing Boron Triflouride, surrounded by 2 cm of polyethylene and ~14 cm of lead, as shown in **figure 3.9**. When the secondary nucleonic component of a cosmic ray shower interacts with the lead, neutrons are produced. The polyethylene slows these neutrons to energies at which they can be detected by the $BF_3$ tubes. Once the neutrons enter the tubes, there is a ~0.057 chance that they will undergo a reaction defined by: $^{10}B_5 + n \rightarrow {}^{7}Li_3 + {}^{4}He_2$. The counter then detects the electrical discharge caused by the Li nucleus and the $\alpha$ particle. The entire counter is also surrounded by a thick (~7.5 cm) layer of polyethylene that acts to reflect and moderate the neutrons from the lead, as well as absorb the low energy neutron produced in surrounding material external to the counter.

By placing neutron monitors at various latitudes, a sampling of the proton spectrum can be obtained. This is a result of the fact that each location on the Earth has a characteristic cutoff rigidity for charged particles due to the geomagnetic field. Rigidity is used in this discussion, rather than energy, since particles with the same rigidity will have the same dynamics in a magnetic field. Rigidity is defined as : P[Volts] = pc/Ze, where pc is momentum times the velocity of light and Ze is electric charge. For vertically incident particles, this cutoff rigidity is given by $P_c$ [GV] = (14.9/e) $\cos^4(\lambda)$, where $\lambda$ is the geomagnetic latitude (Longair 1992). These cutoff rigidities range from ~1 GV to ~14 GV for high latitudes and equatorial latitudes, respectively. Another effect of the geomagnetic field on charged particles is that the particles are deflected from

their original direction. Thus, one can define asymptotic directions for a particular neutron monitor location that determines the original (i.e. external to the magnetosphere) direction of a particle that hits the atmosphere vertically. This effect is, of course, a function of particle rigidity.

While a single neutron monitor acts as an integral counter above a threshold defined by the geomagnetic field, it is evident that a series of neutron monitor stations at a variety of locations could act as a spectrometer. The world-wide network of neutron monitors operates in this way. The intensity of a signal at one station can be compared to the intensity of that signal at another station with a different response and cutoff rigidity to determine characteristics of the spectrum. A great deal of spectral information can be gleaned for solar proton

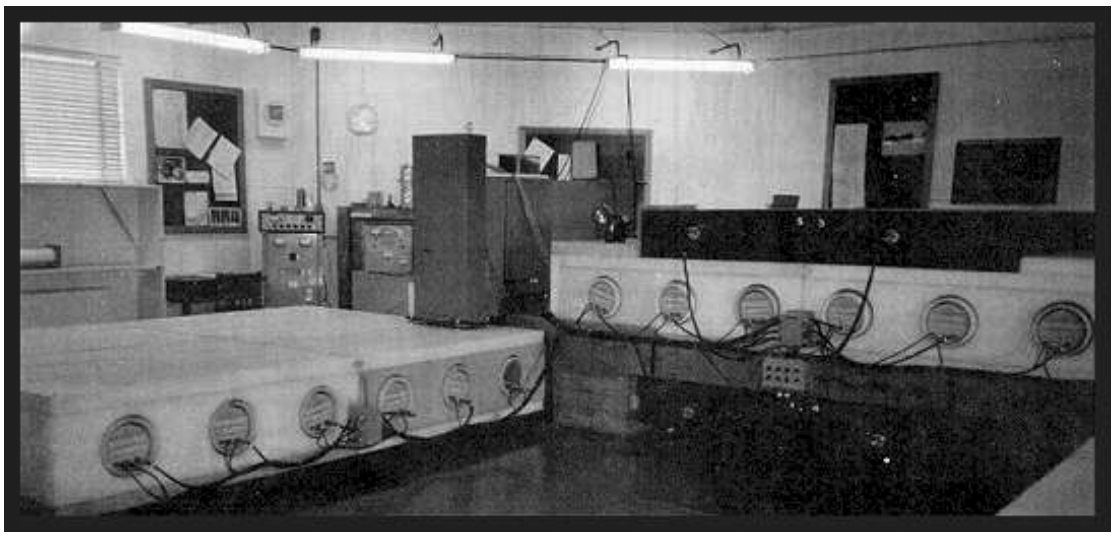

Figure 3.9 - The Inuvik neutron monitor. The ends of the sealed tubes containing Boron Triflouride can be seen. (Picture courtesy of Bartol Research Institute)

events by using many monitors in this way (Lockwood et al. 1999, Lovell et al. 1998, Debrunner 1994). While neutron monitors are nominally sensitive to protons up to ~30 GV, the effective areas are typically too low to obtain

significant measurements of solar proton events above ~10 GV. The relative signals in neutron monitors may also be used to differentiate between solar proton and neutron events. Neutrons will not experience the deflections in the magnetic field that cause the characteristic station to station intensity variation. Additionally, solar neutron events are not visible to neutron monitors on the night-side Earth, while proton events frequently reach a degree of isotropy that allows them to be seen by many monitors on the night-side of the Earth.

# CHAPTER 4

# THE MILAGRITO INSTRUMENT

Milagrito operated in the Jemez Mountains near Los Alamos, New Mexico as a prototype for the Milagro instrument from 8 February 1997 to 7 May 1998 (Atkins et al. 2000; McCullough et al. 1999). The detector, which was built in a pond that was previously used by a geothermal research group, utilized the water Cherenkov technique to detect EAS particles. Although it was operated as an engineering model for the fully-instrumented Milagro gamma ray observatory, Milagrito accumulated useful data of its own with a novel detection technique. Both Milagro and Milagrito were designed as TeV gamma ray observatories, but this work will concentrate on Milagrito's abilities as a SEP and cosmic ray observatory.

## Cherenkov Emission

Cherenkov emission occurs when charged particles travel faster than the speed of light in the medium that they are traversing. This process is roughly analogous to the sound waves that are emitted at the shock produced by an object, such as an airplane, travelling faster than the speed of sound in the medium being traversed. For Cherenkov emission to occur, the velocity of the charged particle must exceed a threshold given by $v_{th} > c/n$, where n is defined

as the index of refraction in the medium. Otherwise, the energy loss of the particle is deposited in the local dielectric medium, rather than escaping to infinity in the form of Cherenkov radiation. From the previous condition, one can see that there is a threshold for total particle energy given by $E_{th} = m_0 c^2 \Big/ \sqrt{1 - n^{-2}}$. In water, this leads to a Cherenkov emission threshold energy of 0.775 MeV for electrons and 160 MeV for muons.

There is also a characteristic emission angle for Cherenkov radiation. The radiation will propagate in the direction of **E**×**B**, which leads to an emission angle given by $\cos(\theta_c) = 1/n\beta$. Thus, the radiation is emitted symmetrically, in a pattern referred to as the Cherenkov cone, about the particle trajectory. Since the index of refraction is a function of frequency, there is a frequency dependence for the threshold energy and the angle of the Cherenkov light cone. For water with an index of 1.34, the angle of Cherenkov emission will be 42˚ for highly relativistic particles. In air, the Cherenkov angle for highly relativistic particles will be approximately 1.4˚. This narrow cone of Cherenkov emission in air contributes to the air shower in the atmosphere and can be observed by air Cherenkov telescopes at the ground level. However, the index of refraction of the atmosphere is a function of altitude, so the opening angle of the light cone will vary as the shower propagates to lower levels. In Milagrito, the large opening angle of the Cherenkov light in water leads to the capability for many PMTs to view the signature of a single particle traversal.

## Physical Parameters

The Milagrito detector was composed of 228 upward-facing photomultiplier tubes (PMTs) submersed under 1-2 meters of "clean" water. These PMTs were placed within a pond with surface dimensions of 80×60×8 m. The cross-section of the pond, as shown in **figure 4.1**, was actually a trapezoid with bottom dimensions of 50×30 m. Within the pond, the PMTs were attached to a grid composed of sand-filled PVC pipe and placed in a square grid pattern with 3 m spacing between each PMT. On the surface of the pond, there was a polyethylene cover (this cover could be inflated for the purpose of entering and working within the pond) that provided a light-impermeable environment, thus allowing the detector to operate free of background light throughout the day and night. When an energetic hadronic particle or gamma ray is incident on the Earth's atmosphere, it can trigger an EAS that propagates downward in the form of a thin ( ~1-3 m) "pancake-like" plane of secondary particles. Upon entering the water of the Milagrito pond, the charged particles from the EAS produce Cherenkov light in characteristic 42˚ light cones. These Cherenkov photons are then detected by the PMT array (**figure 4.1**). The gamma rays in the EAS

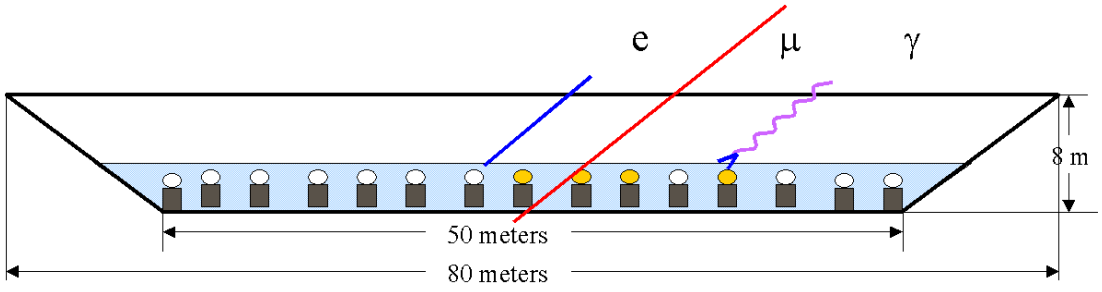


Figure 4.1 - Cross-sectional view of the Milagrito detector.

Figure 4.2 - Aerial view of Milagrito/Milagro pond. The cover is inflated in this picture so that work can be done under the cover for installation of the Milagrito hardware. The telephone poles that can be seen surrounding the pond are part of the lightning protection system.

undergo both Compton scattering and pair production when they enter the water, thus contributing to the Cherenkov photons detected in the pond. With this water-Cherenkov technique, a large fraction of the shower particles can be detected, and a low threshold energy is achievable.

Milagrito was located in the Jemez mountains near Los Alamos, NM at an elevation of 2650 m (**figure 4.2 & 4.3**). This corresponds to an atmospheric overburden of ~750 $g/cm^2$. Since protons have a mean free path of ~62 $g/cm^2$ for nuclear collisions, the altitude of the detector corresponds to ~12 mean free paths. Thus, the detector was located well below the location of shower

maximum for nearly all showers detected. This situation, in which one is observing on the tail of a distribution, is common in the fields of high energy gamma ray and cosmic ray air shower physics. This is a characteristic that guides much of the design of the detectors of these showers. It would, of course, be desirable to locate the detector at a higher altitude, but high altitude locations can be difficult due to practical considerations, such as access to the site. Milagrito approached this situation with another method. Rather than placing the detector closer to shower maximum, Milagrito attempted to detect more of the shower particles at ground level. Traditional EAS arrays spread relatively small detectors over a large area, thus detecting only a small fraction of the shower particles from an EAS. By utilizing one large detector, Milagrito was able to detect a large fraction of the shower particles that fell within its active area. In this way, the energy threshold was significantly lowered.

Another location-related factor that contributed to Milagrito's threshold

Figure 4.3 - View under the cover of the pond. The PVC frame to which the positively buoyant PMTs are mounted can be seen.

energy was the geomagnetic field. As discussed earlier, in the section related to neutron monitors, the geomagnetic field deflects charged particles whose rigidity is not large enough to overcome the bending caused by the field. The threshold rigidity for deflection is a function of the location of the detector within the geomagnetic field. Milagrito is located at a geographic latitude of 35.9˚N, which corresponds to a geomagnetic latitude of 44.5˚N. This places the vertical cutoff rigidity of Milagrito at ~3.86 GV, neglecting variations in the Earth's geomagnetic field. This geomagnetic cutoff, along with atmospheric attenuation at low energies, will determine the threshold of the detector.

In order to collect the Cherenkov light in the water of the Milagrito pond, sensitive PMTs with a large photocathode area are desirable. Other desirable characteristics for the Milagrito PMTs are fast rise time and minimal transit time jitter, in order to obtain good time resolution. Charge resolution that allows for the resolution of the single photoelectron peak is a necessity for calibration purposes. In order to avoid misidentification of pulses, a PMT with minimal prepulsing and after-pulsing is also desirable. The model of PMT chosen for use in Milagrito was the 20 cm diameter, 10-stage Hamamatsu R5912SEL. The PMTs, as well as the bases, were encapsulated in a PVC housing that protected the electronics from the water of the pond. Additionally, the base was coated with a silicon conformal coating that protected the components from humidity. The positive high voltage was connected to the PMTs through nominally watertight coaxial connectors and bulkhead connectors made by W.W. Fischer that were connected to the PMT housings. The PMT signal was carried on the same RG-59 cable used to supply the high voltage to the PMT. Several PMTs that are mounted within their encapsulation are shown in **figure 4.4**.

The water in Milagrito was initially obtained from a fresh water well at the site of the detector. It was then pumped through a filtration system and recirculated throughout the lifetime of the detector. The water was pumped through a pump at the bottom of the pond at a nominal rate of 725 l/min. The water filtration system was composed of a series of stages including a 1 μm filter, a carbon filter, a UV lamp, and a 0.2 μm filter. The attenuation length of 350 nm light in the pond water was measured to be ~5 meters.

Figure 4.4 - Photomultiplier tubes mounted to their encapsulation hardware. These tubes are actually in the pond during the time frame between Milagrito operations and Milagro operations. They are tethered to the PVC grid. When the water fills the pond, the positive buoyancy of the tubes will cause them to float to a pre-determined level and point upward.

Since Milagrito was located within one of the most lightning prone areas in the United States, a system to protect the observatory and the associated electronics was necessary. The lightning protection system used to protect

Milagrito was a 12,500 $m^2$ Faraday cage that enclosed the entire observatory site. The cage was essentially composed of a mesh of wires that were suspended by telephone poles above the entire site, including the buildings containing the electronics hardware. This system was devised to intercept, rather than avoid, the lightning strikes in the area. Once the lightning was intercepted, the charge was shunted to ground, thus dangerous voltage gradients were avoided within the site enclosed by the Faraday cage.

## Electronics and Data Acquisition System

The cables from the PMTs were routed out of the pond, and they were subsequently fed into a patch panel. From there the signals traveled through underground conduit to the house containing the electronics, known as the counting house. Once the signals from the PMTs reached the counting house, it was necessary to obtain timing and pulse height information, as well as make triggering decisions. Custom made front end electronics (FEEs) boards were used to distribute high voltage to the PMTs and to process the signals prior to readout and storage.

Before describing the path taken by the signal through the Milagrito electronics, the time-over-threshold (TOT) technique, which was used by Milagrito, should be described briefly. The TOT technique can be used to replace much of the functionality of analog-to-digital-converters (ADCs). The TOT technique makes a measurement of the time a pulse spends above a defined threshold, as shown in **figure 4.5**. This time is then related to the size of the

signal in the PMT. Milagrito used an ADC to calibrate the conversion of photoelectrons to TOT. With the exception of this calibration, ADCs were not required for the operation of Milagrito. The advantages of the TOT technique are primarily a result of this absence of ADCs in the processing. Since there are no ADCs, which slow down the processing, there is less dead time. The event size, and consequently the amount of data that needs to be handled, is reduced since the TDCs contain the pulse height and the timing information without the need of the ADC data. There is also a financial savings when the TOT technique is used, since the need to purchase an ADC channel for each PMT is eliminated. A disadvantage to using the TOT technique is that it will not provide as good a measurement of the pulse size as an ADC. This is due to the fact that typical pulses rise and fall at an exponential rate with time. This problem is countered

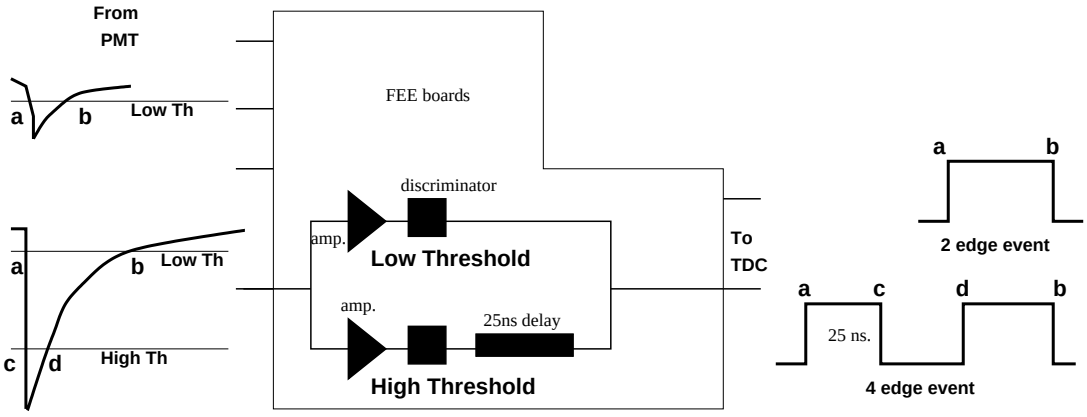


Figure 4.5 - Milagrito's front end electronics (FEE) boards measured the time that a signal pulse spent with its voltage in excess of two predetermined thresholds. This time could then be correlated with the amplitude of the pulse by calibrating with an ADC.

somewhat by the fact that the dynamic range of the TOT technique is superior to that of standard, commercially-available ADCs. Another problem with the TOT technique is that prepulses and after-pulses can lead to mismeasurements of

signal durations. In an attempt to alleviate this problem, Milagrito had two independent thresholds that could be used to differentiate between large events, which are more likely to have associated prepulses, and small events.

An analog FEE board did the initial signal processing. These boards distributed high voltage to two groups containing 8 channels each, such that one board could supply high voltage for up to 16 PMTs. Each channel contained a resistor that could be adjusted to vary the high voltage supplied to an individual PMT. The analog signal came into this board through the same cable that supplied the high voltage. The PMT signal was AC coupled to the amplifier inputs by a high voltage capacitor on the analog board. The signal was split, and both branches were passed through their own respective amplifiers with different gains. One of these branches was fed through a high threshold discriminator, while the other branch was sent to a low threshold discriminator. The amplifier gain and the discriminator threshold were set so that a signal with ~1/4 photoelectrons would pass the low threshold discriminator, while a signal with ~7.6 photoelectrons would pass the high threshold discriminator. The output of the amplifier associated with the low threshold was actually split into two parts so that one part could be sent to an ADC, which was used only for calibration. Both of these discriminators generated TOT pulses **(see figure 4.5)**. The discriminator outputs were sent to the custom made digital FEE boards that performed the digital signal processing.

The digital FEE boards multiplexed the low and high threshold discriminator signals and provided triggering information. Each PMT signal crossing a discriminator threshold generated a 300 ns pulse with a 25 mV amplitude. Multiplicity triggering information is provided by the simple sum of

these pulses. Multiplicity information was independently provided for both the low and high threshold discriminators. The low threshold multiplicity information was used to create the 100 PMT trigger requirement that will be described later in this chapter.

The Milagrito timing and pulse height information were encoded as a series of edges as shown in **figure 4.5**. These data were digitized using three LeCroy 1887 FASTBUS TDC modules. Each of these modules contained 8 event buffers and 96 channels that could each record up to 16 edges per event with 0.5 ns resolution. The time of each event was recorded by using a latched GPS clock.

After digitization, the data were read out with a FASTBUS smart crate controller (FSCC). The FSCC transferred the data to a pair of dual ported VME memory modules, which allowed for the simultaneous reading and writing of data. An SGI Challenge L multi-CPU computer was responsible for reading the data from the memory boards over the VME bus. Commands from this computer controlled the operation of the detector electronics. The system could be controlled remotely via the internet, and in cases that required human intervention, the automated system was capable of sending an alert to a pager carried by the collaboration member on active shift duty. This system allowed Milagrito to operate with less than 0.5% dead time with a trigger rate of ~300 Hz. The raw data and the online-processed data were saved to DLT tapes throughout the lifetime of the experiment.

There was another system that operated nearly independently of the DAQ described above. The environment monitoring system (EMS) was used to monitor the status of many aspects of the observatory and its surrounding environment. Weather information, such as air temperature, air pressure,

humidity, wind speed, and precipitation were recorded. Temperature measurements inside the counting house and within the electronics racks were also recorded. Pond water characteristics such as depth, recirculation flow rate, pressure within the filtration system, and water temperature were also recorded. Status of PMTs and their associated high voltage were recorded. Scaler counter rates from an independent CAMAC system, as well as trigger rates of the detector were also recorded. All of these data, updated at ~3 minute intervals, could be monitored remotely from a web page, and the data were archived.

## Modes of Operation

Milagrito was able to operate in several modes of operation. During this discussion, it is important to remember that all of these modes were in operation simultaneously. There was no need to switch from one mode to another during operation. The researcher merely needs to look from one data set to the other to observe in a different mode.

### 100 PMT Shower Mode

Designed as a Very High Energy (VHE) gamma ray observatory, Milagrito's baseline telescope mode of operation, which will be referred to as the 100 PMT mode, was sensitive to extensive air showers from primary hadrons and gamma rays above ~100 GeV. In this mode, Milagrito required >= 100 PMTs to trigger within a 300 ns coincidence window in order for the data acquisition

hardware to record an event. In this 100 PMT mode of operation, a PMT triggers when its pulse height exceeds the low threshold, corresponding to ~0.25 photoelectrons measured by the TOT technique. For each event, the time and pulse height in each PMT were recorded. Once these data were recorded, they

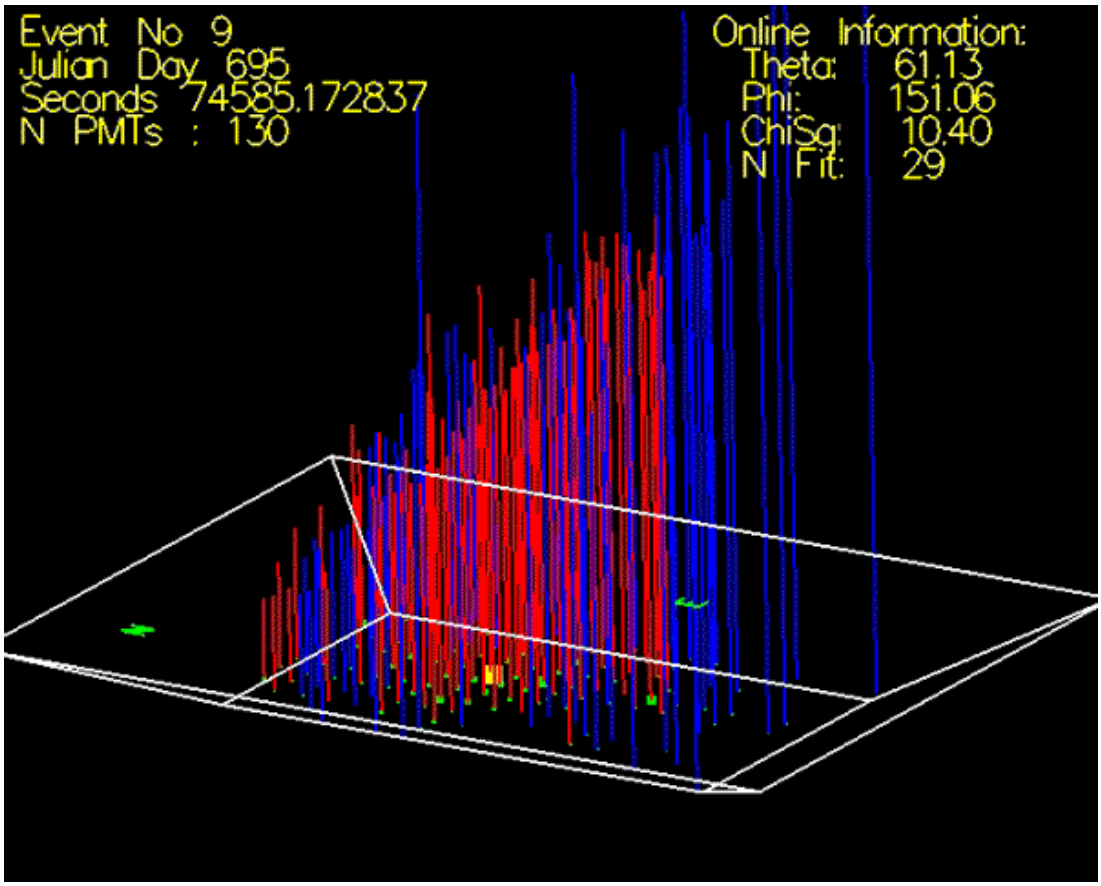


Figure 4.6 - Display of the relative timing of individual PMTs for a real event in the Milagrito data. The differences in PMT onset times, which are proportional to the heights of the lines in the figure, are used to reconstruct the shower direction for events that satisfy the 100 PMT trigger requirement. This event had 130 hit PMTs, and 29 of those PMTs were used in the fitting procedure. The plane of the shower front is visible.

could be used to reconstruct the incident direction of the primary particle with a resolution of ~1˚. The hadron-induced showers were treated as background for the gamma ray source observations for which the instrument was designed, but

these events were treated as a signal for the purposes of solar and cosmic ray physics.

In order to reconstruct the incident direction of the primary particle, the relative timing of the individual PMTs in the pond was utilized (**figure 4.6**). Before doing this, one must make a series of corrections. Timing corrections must be applied to the PMT arrival times to account for slewing effects, transit time effects, and the different timing pedestals of the individual PMTs. An additional correction must be applied to account for the curvature of the air shower. Although shower curvature was certainly present in the Milagrito data, it was not evident due to the fact that Milagrito was not capable of accurately determining the shower core position. Monte Carlo studies indicated that a fixed curvature correction of 0.04 ns/m should be applied. Once the core location was estimated for a given shower and the timing corrections were applied, the shower direction was determined by fitting the shower plane using a weighted least squares fitter ($\chi^2$). This fitting procedure was an iterative process. The first iteration used only those PMTs that had a pulse height in excess of 2 PEs. Subsequent iterations used PMTs whose contribution to the $\chi^2$ was less than 9, 6.25, and 4, respectively. This procedure was developed by studying the difference in space angle of fit for two interleaved portions of the detector, referred to as $\Delta_{eo}$. As should be expected, the value of $\Delta_{eo}$ decreases for events that have a high number of PMTs that are used in the fitting procedure.

In the 100 PMT mode, ~90% of the events that are recorded are capable of passing through this fitting procedure. These events that cannot be fit, which we refer to as NoFits, are thought to be associated with single muons that arrive

from grazing directions (zenith angle > 93˚) and single hadrons. Based on Monte Carlo studies, high zenith angle muons are thought to contribute ~6% to the 100 PMT trigger, while single hadrons are thought to contribute ~3%.

## Scaler Mode

In addition to recording these 100 PMT mode events, thus operating as a telescope, Milagrito also had a scaler mode of operation. This mode of operation is similar to that of a neutron monitor. It records a time-integrated measurement that corresponds to the rate of single PMT hits in the pond. In this scaler mode of operation, a PMT was considered to be hit when its pulse height exceeded a defined threshold. There were actually two scaler modes, the low threshold scaler mode and the high threshold scaler mode. The high threshold output, which counts only those events with pulse heights in excess of ~7.6 photoelectrons, has considerably less background fluctuation than the "low" threshold output used for the 100 PMT baseline mode. This is important when considering the large number of smaller and unreconstructable events registered in the scaler mode. For the high threshold scaler mode, the PMTs in the pond were separated into 15 patches that contained 16 PMTs each. The scalers registered the logical OR of the PMT hits within a patch by counting the number of patches that registered at least one hit during a ~45 ns interval. Thus, an event that triggers only one PMT constitutes a count in the high threshold scaler mode, and an event that triggers several PMTs (within ~45 ns of each other) within one patch of 16 PMTs will also constitute only one count in this mode. The same

method was used for the low threshold scaler mode except for the fact that the low threshold scaler mode counted the logical OR of groups of 4 PMTs, rather than the 16 PMTs OR'd by the high threshold scalers. The number of scaler hits was read with a period of 1 second.

Since the energy range most likely to be of primary interest to solar physics is <100 GeV, the scaler mode of Milagrito is extremely useful, despite the fact that imaging is not possible with the scaler mode. This mode significantly lowers the energy threshold of Milagrito by detecting the numerous muons and small showers at ground level. Even showers for which only a single muon survives to the ground level could be detected by Milagrito. This is due to the fact that a single charged particle entering the pond can trigger many tubes since its Cherenkov light cone causes a significant lateral spread of photons to many tubes throughout the pond. A substantial fraction of the scaler rate recorded by Milagrito was due to muons, as well as small showers, and an integral measurement above a threshold is performed. These data provide an excellent high energy complement to the network of neutron monitors.

To analyze the scaler data of Milagrito properly, one must first correct the ground level scaler rates for pressure, temperature, and other diurnal effects (Hayakawa 1969). Typical background cosmic ray rate fluctuations on a time scale of ~1 day are shown in **figure 4.7**. Although this figure shows the pressure at ground level, which is not as critical as the measurement of pressure at higher altitudes in the atmosphere, one can easily observe the increase in background rate as the pressure, and consequently the atmospheric overburden, decreases. Atmospheric temperature also effects the background rate, as a result of the variation of muon lifetime with temperature. Although this smaller effect can

not be seen in the figure due to the overwhelming pressure variation, the overall temperature effect can cause variations on the order of $-5\times10^{-2}$ %/˚F. Preliminary estimates of these correction factors for Milagro / Milagrito have been calculated based on observations, and they have been found to be reasonably consistent with past work with muon telescopes (Fowler et al. 1961). Accurate estimates of the pressure and temperature correction factors for Milagrito have not been calculated due primarily to the multide of variations on many timescales that

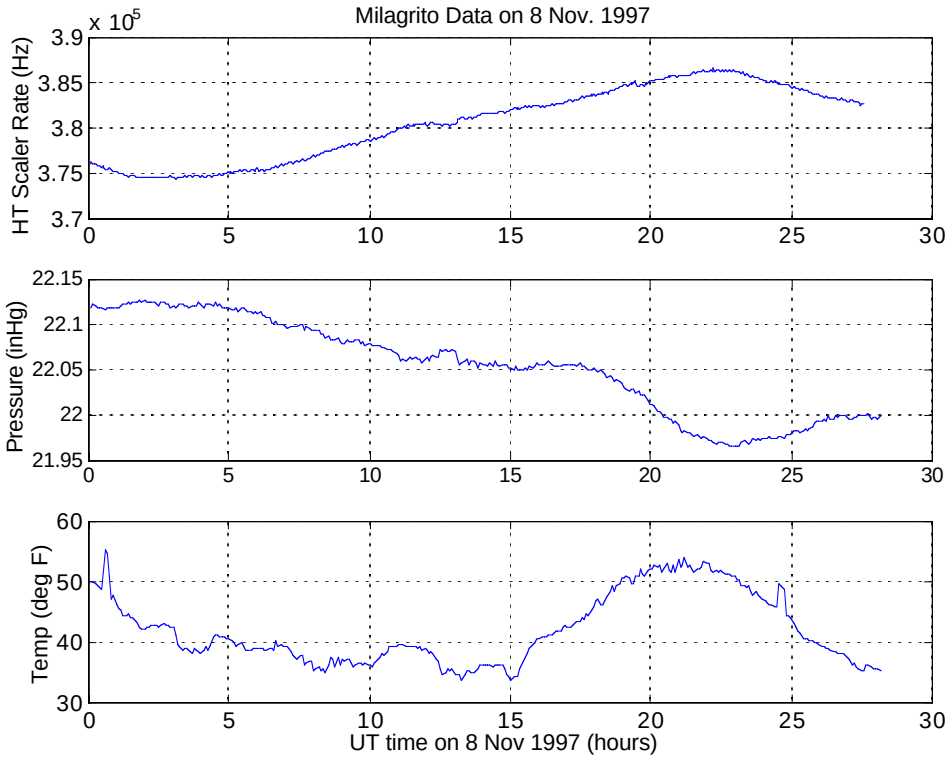


Figure 4.7 - Typical diurnal fluctuations in the Milagrito scaler rate during a time period that is relatively free of instrumental anomalies.

were prsent in the Milagrito data. This was a result of the fact that Milagrito was an engineering prototype that had significant variation in detector parameters such as water level, electronic thresholds, and light-leak integrity of the cover.

However, these atmospheric corrections are less important for fast transient events that rise above background quickly and have short durations.

## Simulation of Detector Response

The complete simulation of the detector response was performed in two steps. The initial interaction of the primary particle with the atmosphere and the generation of secondary particles was simulated with the CORSIKA air shower simulation code (Heck et al. 1998). The second step was to simulate the response of the detector itself using GEANT (CERN 1994).

Using CORSIKA, the primary particles and shower particles are tracked through the atmosphere, which is stratified into five horizontal layers. The five layers of the atmosphere are based on the US standard atmosphere. In this model, the lower four layers have an exponential dependence of density with altitude, while the upper layer has a linear dependence of density with altitude. When particles initiate a reaction or decay, the secondary particles are also tracked through the atmosphere. Electromagnetic interactions are simulated using EGS 4 code. For the hadronic interactions, the VENUS code is used at high energies, and GHEISHA is used at low energies (<80 GeV).

A wide array of particles can be simulated at many energies for zenith angles ranging from 0˚-90˚ using CORSIKA. However, at this time, particles can only be tracked for simulations with zenith angles between 0˚-60˚. This presents a problem for the estimation of Milagrito's sensitivity. Particle tracking is necessary since Milagrito's low energy signal comes from events whose

properties deviate significantly from average values. Thus, it was necessary to extrapolate the simulations between 0˚-60˚ to larger zenith angles when Milagrito's effective area was calculated. This will be discussed more in the following section on the effective area.

Once the air shower has been created using CORSIKA, the response of the detector is modeled using the GEANT package (CERN 1994). This simulation package requires the input of the detector parameters, such as PMT spacing, PMT quantum efficiency, pond size, water characteristics, optical properties of materials in pond, etc. The measurement of these parameters is important since errors can lead to systematic errors in the simulation. In particular, the simulation is sensitive to the scattering of light within the pond. Measurements of the attenuation length of the pond water were necessary. The attenuation length for 350 nm light, including both scattering and absorption was found to be ~4 m (Atkins et al. 2000). The output of GEANT can be analyzed by the offline code, and the detector triggering conditions can be imposed. Thus, a simulation of the detector response is obtained.

## Effective Area

With an analysis based on the Monte Carlo calculations, effective areas of the Milagrito instrument were computed for each of its modes. For the purpose of simulating Milagrito's response, effective area is defined as: $(N_{trigger} / N_{throw})A_{throw}$, where $A_{throw}$ is the area over which the shower core is thrown and $N_{trigger}$ and $N_{throw}$ are the number of triggers and the number of

primary particles thrown, respectively. Of particular interest for solar ground level events, as well as cosmic ray studies, are the effective areas of Milagrito to protons incident on the atmosphere isotropically, at zenith angles ranging from 0°-90° (**Figure 4.8**). The curves shown in the figure correspond to the high threshold scaler mode and the 100 PMT mode. The effective area from 60°-90° was estimated by extrapolating the area curve from the 0°-60° range. In the

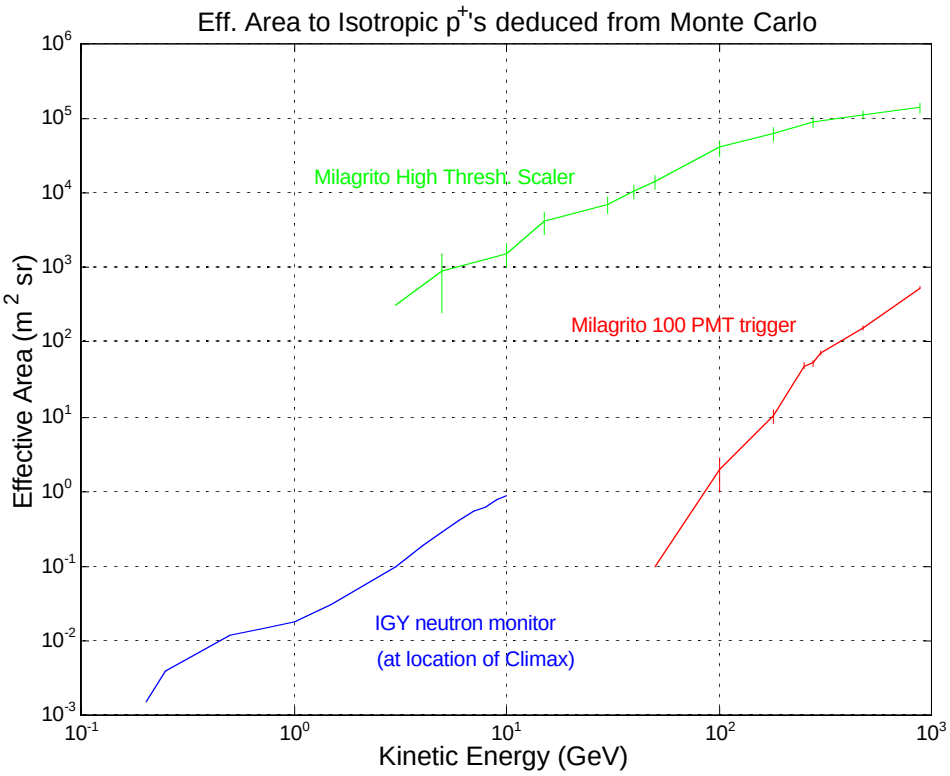


Figure 4.8 - Effective area of Milagrito to isotropic protons incident on the top of Earth's atmosphere, with an IGY neutron monitor for comparison. These calculations are based on Monte Carlo proton events thrown over zenith angles from 0˚-60˚, with extrapolated values used for zenith angles from 60˚-90˚.

absence of effects specific to large zenith angles, the majority of the contribution to the scaler mode efficiency comes from zenith angles below 60˚. An example of the relative contribution at angles above and below 60˚ for protons at 50 GeV can be seen in **figure 4.9**. Since cosmic ray showers were not simulated between 60°-

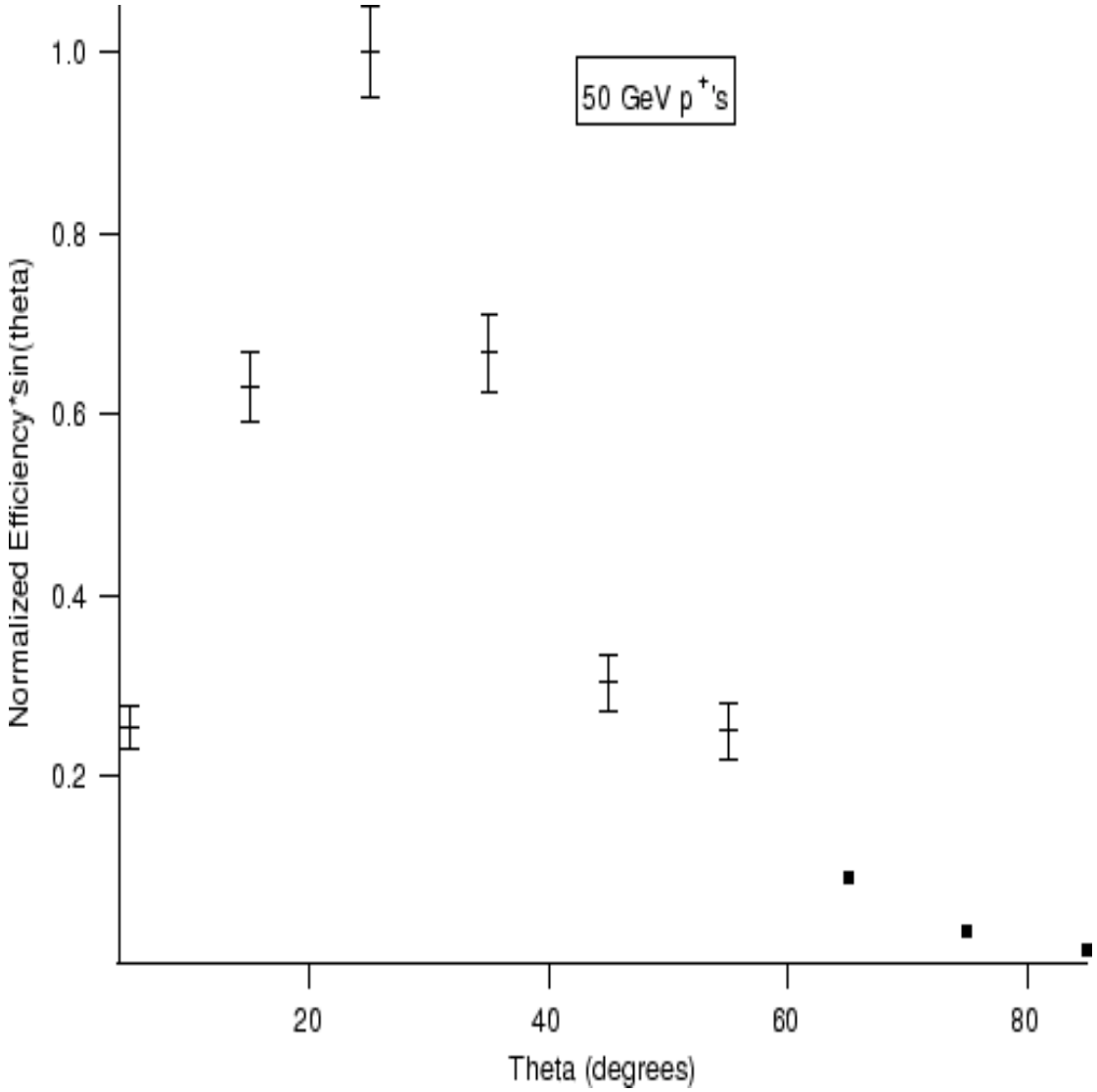


Figure 4.9 - Milagrito scaler mode differential efficiency to 50 GeV protons (from Monte Carlo) normalized to 25˚ and plotted as afunction of zenith angle. Points above 60˚ are extrapolated using a functional fit to points at lower theta. The contribution from θ>60˚ is shown to be small.

90º due to limitations of the software and time, effects that are present only at large zenith angles are not reflected in these effective area curves (the possible effect of high zenith angle muons will be discussed later). While this could have a significant impact on the analysis of the shower mode data, it should not significantly affect the scaler mode data analysis.

The systematic errors of the instrument response have been estimated by folding the known cosmic ray spectrum through the calculated response. This results in a theoretical value for the instrument's rate due to galactic cosmic rays, which comprise most of the instrument's background rate. The measured background rate in Milagrito matches this predicted value to within a factor of ~3. While this provides us with a reasonable level of confidence in the calculated effective area curves, there are still some lingering concerns. There are some concerns with using GHEISHA to simulate showers from primary particles with energies below ~20 GeV (Heck 1999). For these lower energy primary particles, it is possible that the sum of the secondary shower particles' energies can be as much as 20-30% greater than the energy of the primary hadron. While a reasonable agreement (factor of ~3) between the predicted and the measured cosmic ray rates in Milagrito shows that the effective area systematic errors are reasonably small, we are unable to assess the effect of using GHEISHA at energies below ~20 GeV. The areas in **figure 4.8** were calculated using Monte Carlo events whose shower cores were thrown randomly over a large area surrounding the Milagrito pond. To ensure that the Monte Carlo showers were thrown over a large enough area, we progressively increased the throw area until the effective area reached an asymptotic value. This occurred at approximately 7000×7000 $m^2$. **Figure 4.10** illustrates the relationship between Milagrito's predicted effective area and the shower-core throw area for proton showers. We note that the effective area of Milagrito has a significant contribution from hadronic showers with cores far (> 3 km) from the detector. This effect increased the estimated effective area at ~5-100 GeV by ~3 orders of magnitude relative to earlier estimates (Falcone et al. 1999, Ryan et al. 1999). Our

confidence in these revised effective area curves is bolstered by the fact that they predict the instrument's background rate due to cosmic rays to within a factor of ~3.

At 10 GeV, Milagrito's scaler mode effective area is ~3 orders of magnitude greater than that of a sea level neutron monitor, with the effective area rising rapidly with energy. The threshold of Milagrito is defined by the combined effects of the geomagnetic field and atmospheric attenuation. The effects of the atmosphere, for zenith angles between 0˚-60˚ degrees are

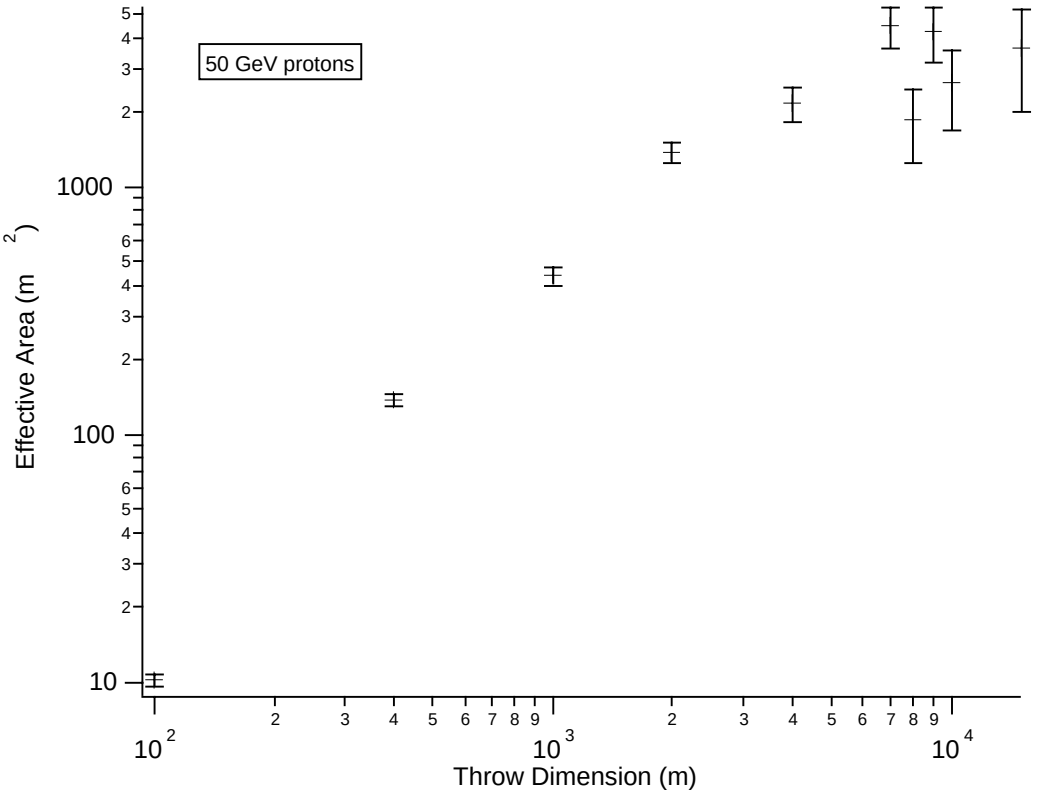


Figure 4.10 - An example, for 50 GeV proton showers, of the relationship between effective area and the spatial dimensions over which the Monte Carlo throws the shower cores. An asymptotic value is approached as the throw dimension becomes large enough to model reality.

incorporated into the effective area curves, while higher angles are assumed to be a simple extrapolation of the curve, as depicted in **figure 4.9**. The

geomagnetic effect is incorporated by assuming a hard cutoff at the calculated vertical cutoff rigidity, which is 3.86 GV. The fact that this is actually a function of zenith angle and magnetic field fluctuations should be considered when interpreting the response of the detector.

## Comparison to Other Instruments

Now that the Milagrito detector has been described, it makes sense to consider it within the context of other existing detectors. There are a wide array of satellite based detectors of cosmic rays, SEPs, and gamma rays; but the sensitivity of these detectors is severely limited by the size of detector that can be launched into space. As a result of this size constraint, satellite detectors require long integration times to be even remotely sensitive at GeV energies. Thus, ground-based techniques such as EAS arrays, ACTs, and neutron monitors dominate at energies in excess of ~ 1 GeV.

Due to the fact that Milagrito detected many air shower particles at ground level over a wide lateral range, many people would define it as an EAS array. While this is true in many ways, there was one important difference that made Milagrito the first detector of its kind, with the exception of its small prototype, Milagrissimo. By making use of the Cherenkov emission of charged particles in water, Milagrito was able to detect nearly all of the particles that crossed the surface of the pond. This included gamma rays since the processes of pair production and Compton scattering led to charged particles that produced Cherenkov emission. In contrast to this, typical EAS arrays detectors cover <1%

of the total area over which they are distributed. Thus, Milagrito was able to realize a much lower energy threshold than a typical EAS array is capable of achieving, while still retaining the abilities of an EAS to operate with all-sky coverage and ~100% duty cycle.

Imaging ACTs are more sensitive to sources than Milagrito or Milagro, thus ACTs can observe over shorter timescales with higher significance. However, ACTs must observe on clear moonless nights to minimize background light. This severely limits their duty cycle. Additionally, ACTs have a relatively small field of view so surveys and detections of transient unknown sources are difficult or impractical. Milagrito and Milagro are well suited for these types of studies due to their ~100% duty cycle and their all-sky coverage.

Neutron monitors are the closest kin to Milagrito and Milagro when considering the energy range. Neutron monitors operate as threshold instruments for detecting primary protons above a few GeV. Milagrito's scaler mode also provided a measurement above a threshold of ~3 GeV, but Milagrito operated with an effective area that was several orders of magnitude larger than that of a neutron monitor, as can be seen in **figure 4.8**. This larger effective area increased Milagrito's probability of detecting SEPs at energies in excess of those probed by neutron monitors. In order to probe anisotropy, neutron monitors rely on a network of monitors placed around the globe at locations with various rigidity cutoffs and atmospheric overburdens. The relative signals in this worldwide network of monitors can be used to determine anisotropy and can be treated as a spectrometer. In this sense, Milagrito was an excellent complement to the worldwide network of neutron monitors, but the high threshold scaler data of Milagrito also provided additional information at higher energies. At

even higher energies, the 100 PMT trigger mode of Milagrito could be utilized. If a source had high enough energy (>~100 GeV) to trigger this mode, then directional information could be obtained based on the relative timing of the hit PMTs.

# CHAPTER 5

# THE 6 NOVEMBER 1997 CME

## Introduction

Particle acceleration beyond 1 GeV due to solar processes is well established (e.g. Meyer et al. 1956, Parker 1957). However, few data exist demonstrating acceleration of particles beyond 5 GeV (Chiba et al. 1992, Lovell et al. 1998). The energy upper limit of solar particle acceleration is unknown but is an important parameter because it relates not only to the nature of the acceleration process, itself not ascertained, but also to the environment at or near the Sun where the acceleration takes place. Due to their small size, space-based instruments are inefficient at measuring the low fluxes of particles above ~1 GeV. However, neutron monitors become efficient at these energies. Neutron monitors provide an integral measurement of the particle intensity above a threshold determined by the location of the monitor. To study the solar energetic particle intensity above the equatorial neutron monitor threshold (~14 GV), other instruments are necessary.

Coronal mass ejections (CMEs) and solar flares are frequently accompanied by SEPs, but the details of the acceleration process(es) continue to elude researchers. Although SEP events are frequently categorized as either gradual or impulsive (Reames 1999, Gosling 1993), some events do not seem to

fit neatly into either category (Mobius et al. 1999, Cliver 1996). The distinctive characteristics of gradual and impulsive events were described in chapter 2, as well as the fact that some events appear to be a hybrid of these two classes. Fast (v>400 km/s) CME-driven coronal and interplanetary shocks are generally thought to be the acceleration mechanism for the gradual events (Lee 1997, Kahler 1992), while the impulsive events are frequently thought to originate at the flare site (Reames 1999). Milagrito's capability of fulfilling the function of studying these high energy SEP events by operating at higher energies with large areas prompted a search of the data at the time of the 6 November 1997 SEP event.

## Some Observations With Other Instruments

On 6 November 1997 at 11:49 UT, an X9 flare with an associated coronal mass ejection occurred on the western hemisphere of the Sun. At a longitude of 63˚, this event was magnetically well connected to the Earth, along the Parker spiral geometry of the interplanetary magnetic field. This event was well observed with many instruments, and it exhibited both gradual and impulsive characteristics.

The GOES-9 satellite detected energetic protons in excess of 100 MeV, as well as hard X-rays from the 6 November event. The proton fluxes are shown as a function of time in **figure 5.1**. The channels corresponding to interplanetary flux of protons above 10 MeV and 50 MeV also registered significant increases. The enhancement of this proton flux lasted for several days after the event. It is

also clear from **figure 5.1** that there was a SEP event on November 4 1997. The flux of interplanetary protons above 10 MeV was still enhanced relative to background at the time of the 6 November event. While the 4 November event did not produce particles with enough energy to be registered in ground based detectors, its effect on the interplanetary environment and the implications related to the 6 November event could be important so they will be discussed later.

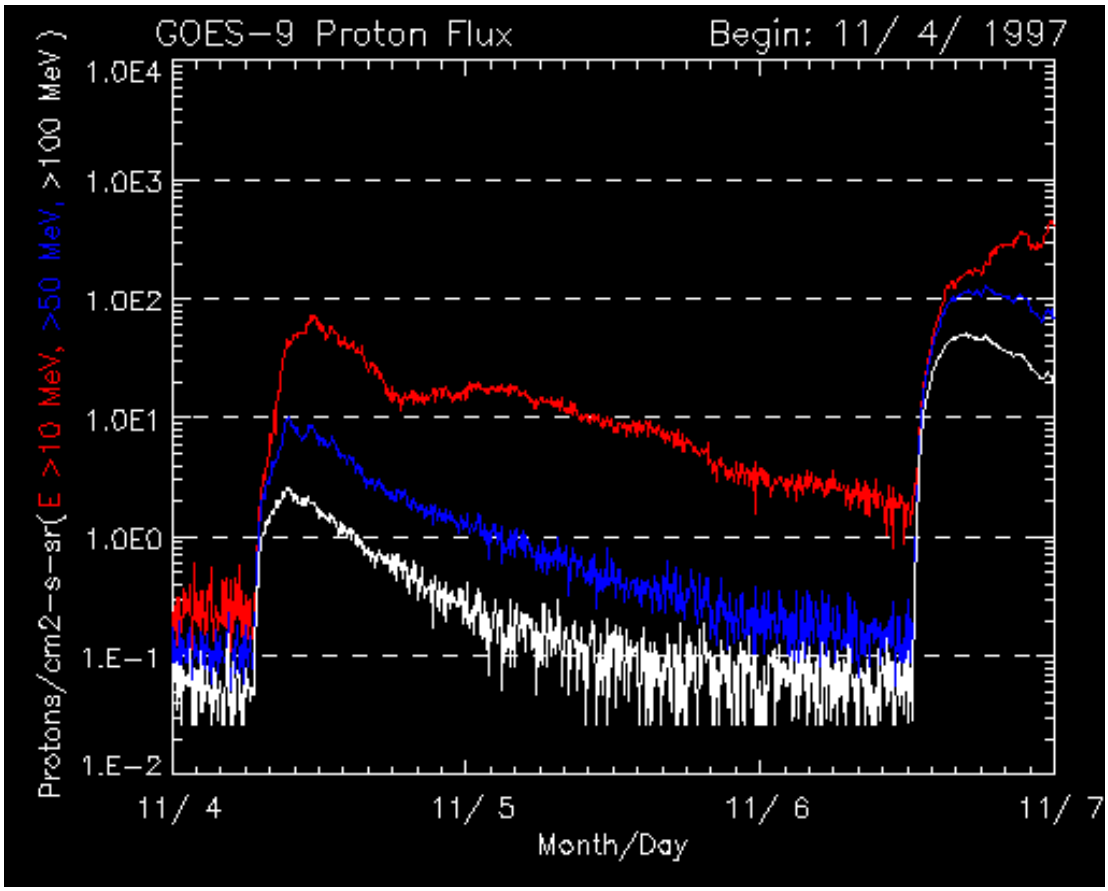


Figure 5.1 - Interpanetary proton flux observed by GOES-9 during the onset and the time period leading up to the 6 November 1997 solar energetic particle event. The three separate curves corresepond to fluxes of protons in excess of three different energy thresholds (E>10 MeV, E>50 MeV, E>100 MeV). The onsets of the 6 November event and the 4 November events are both plainly visible.

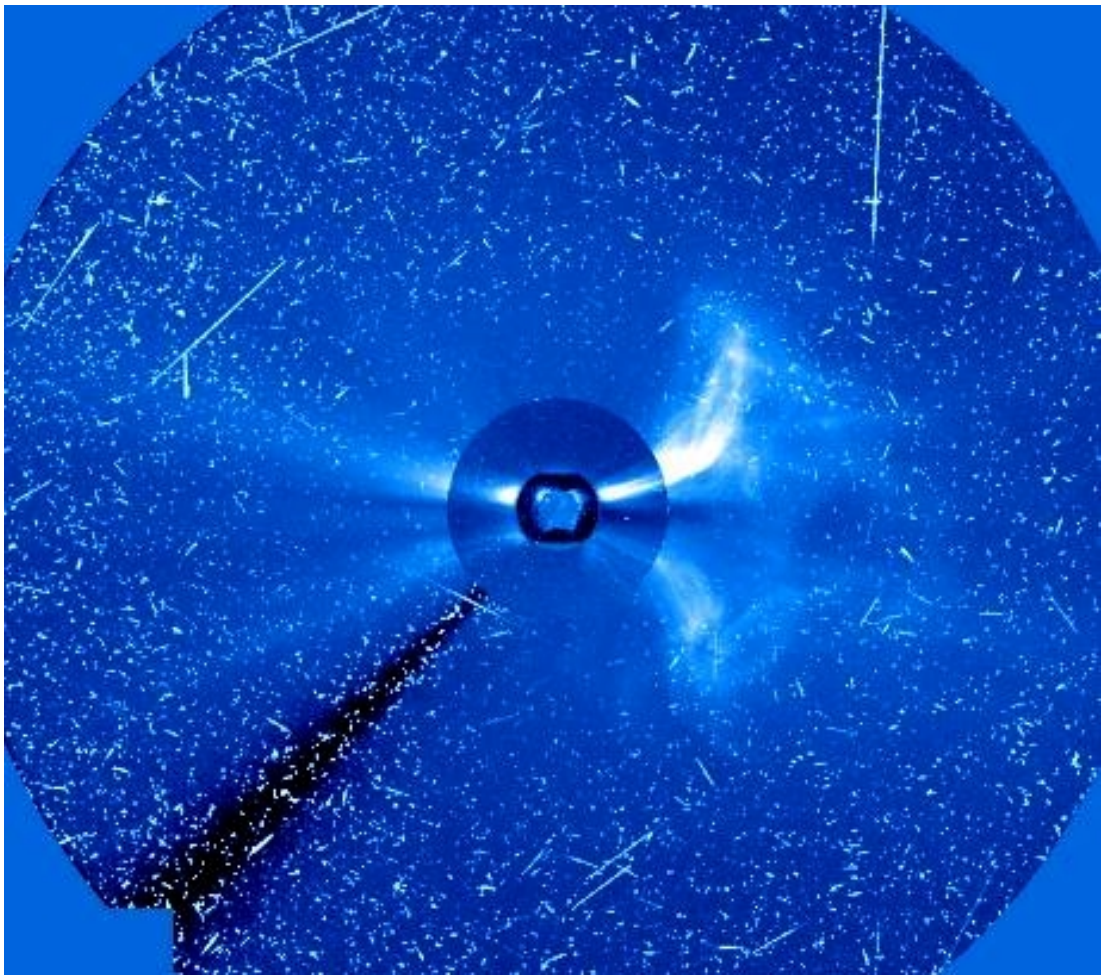

Figure 5.2 - Image of the 6 November 1997 CME using the C2 coronagraph on board SOHO. The central disk of the Sun is blocked out at the center of the image in order to view the coronal regions. The hot plasma can be seen expanding out into the corona. The small tracks dispersed throughout the image are due to energetic particles hitting the detector itself.

As shown in **figure 5.2**, the C2 coronograph on board the SOHO satellite detected the launch of the CME. Using coronograph images, the speed of the leading edge of the CME was estimated to be ~1600 km / s (St. Cyr 2001, Torsti 2000). This speed was deduced by calculating the slope of a line fit to the height-versus-time plot that is shown in **figure 5.3**. This relatively fast CME was undoubtedly driving a strong shock as it propogated since its leading edge speed

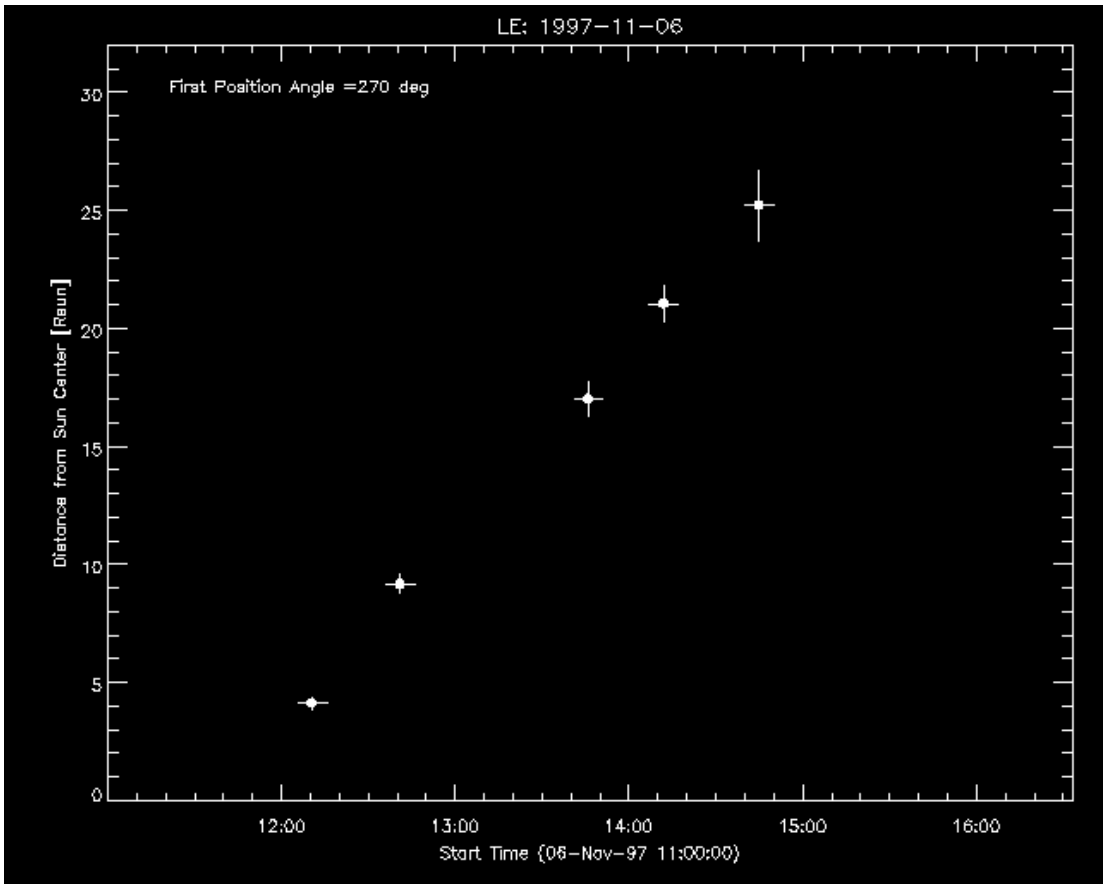


Figure 5.3 - Coronal height of CME leading edge as a function of time during the 6 November 1997 event. Data was obtained from the C2 and C3 coronagraph on SOHO. (Figure courtesy of C. St. Cyr)

was far in excess of the ambient solar wind speed. Type II and IV radio emission were also observed during this event, indicating the presence of a coronal shock.

Yohkoh recorded impulsive gamma-ray emission up to 100 MeV for approximately 5 minutes, along with the presence of gamma ray lines (Yoshimori et al. 2000). The presence of gamma ray lines is a sign that there was significant proton acceleration since the gamma ray lines are a result of nuclear interactions between ambient nuclei and high energy particles, such as protons and alpha particles. This impulsive emission of gamma rays began at 11:52 UT, which was shortly after the onset of the X-ray event.

Using ACE measurements, Cohen et al. (1999) and Mason et al. (1999) reported exceptionally hard ion spectra above 10 MeV/nuc. The SEPICA instrument on board ACE observed an increase in charge state with energy, as well as mixed charge state distributions for Fe (Mobius 1999). This has been postulated to be a result of multiple energetic particle populations. Furthermore, Fe and $^{3}$He enhancements (Fe/O~1 and $^{3}$He/$^{4}$He~4× coronal) were evident in the interplanetary particle populations. These values are greater than those expected for a gradual event, but the enhancements are not as great as those found in many impulsive events.

There were also ground-based measurements of this event. Many of the instruments in the world-wide network of neutron monitors registered a ground level enhancement (GLE) in response to high energy (>1 GeV) protons (Duldig et al. 1999). The rate increase began shortly after 12:00 UT with an anisotropic component, but the distribution approached isotropy by the time of maximum, approximately 45 minutes after the onset (Lovell et al. 1999). Low latitude monitors, such as Mexico City (cutoff rigidity ~ 8.6 GV) did not record an increase. The Climax neutron monitor, located < 400 km north of the Milagrito site with a vertical cutoff rigidity of ~3 GV, was among the monitors to record an increase.

## Observations of the 6 November 1997 Event Using Milagrito

The scaler mode and the "100 PMT" mode of Milagrito can be treated as independent data sets.

## Scaler Mode Observations

In its scaler mode, Milagrito measured a rate increase coincident, within error, with the increase observed by Climax (see **figure 5.4**). If one accounts for the background meteorological fluctuations that are present, the event duration and time of maximum intensity, as seen with Milagrito, are also consistent with

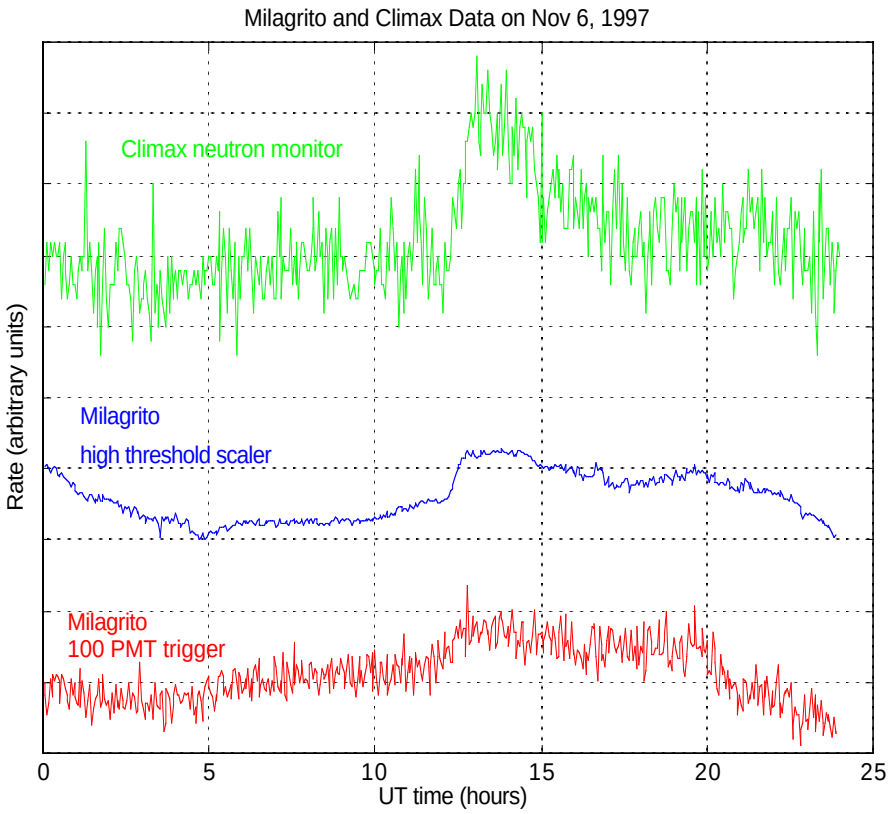


Figure 5.4 – Milagrito rate history plotted over the same timescale as the nearby Climax neutron monitor. The high threshold scaler rate increase of Milagrito was coincident with the rate increase observed by Climax. Diurnal background variations are also visible in the Milagrito data.

that of Climax. The magnitude of the scaler rate increase is ~22 times the RMS fluctuations of the instrument's background using 160 second time bins. The background scaler rate prior to the event was ~375 kHz, and the event produced a rate increase of ~0.5 % from the onset to the time-of-maximum. The RMS of observed background fluctuations, which is approximately ± 84 Hz, is nearly twice that expected from Poisson statistics. These larger fluctuations may be a result of effects such as meteorological fluctuations in the upper atmosphere and at the Milagro site. We also estimated the chance probability of an event rate increase of this magnitude, over this time scale, by looking at the data over the lifetime of Milagrito. This was done by splitting all of the Milagrito high threshold scaler data into 10 minute time bins. The difference between the average rate in any two time bins seperated by one hour from the start of one bin to the start of the next was then calculated. There were only two other rate increases of at least this magnitude during the 15 month (~20% dead time due to maintenance, etc.) lifetime of the instrument (Williams et al. 1998). One of these is a possible light leak, and the other has been identified as a power up transient effect. Based on this analysis, it has been found that the upper limit of the probability for a chance rate increase with a magnitude and timescale similar to that of the 6 Nov.1997 event is $\sim 2 \times 10^{-4}$.

While the daily variations of the background are present, as described earlier, the onset is plainly visible above this background and the fluctuations of the background. Since this event rate exhibited a fast rise above background, the need to apply pressure and temperature corrections was minimized. A rough, first-order background subtraction is shown in **figure 5.5**. This method simply

fits a line to the background rate at the times immediately preceding and following the event. Although initial estimates have been made for the pressure and temperature correction coefficients, it appears as though more upper atmosphere data, as well as observations using a more stable configuration of the

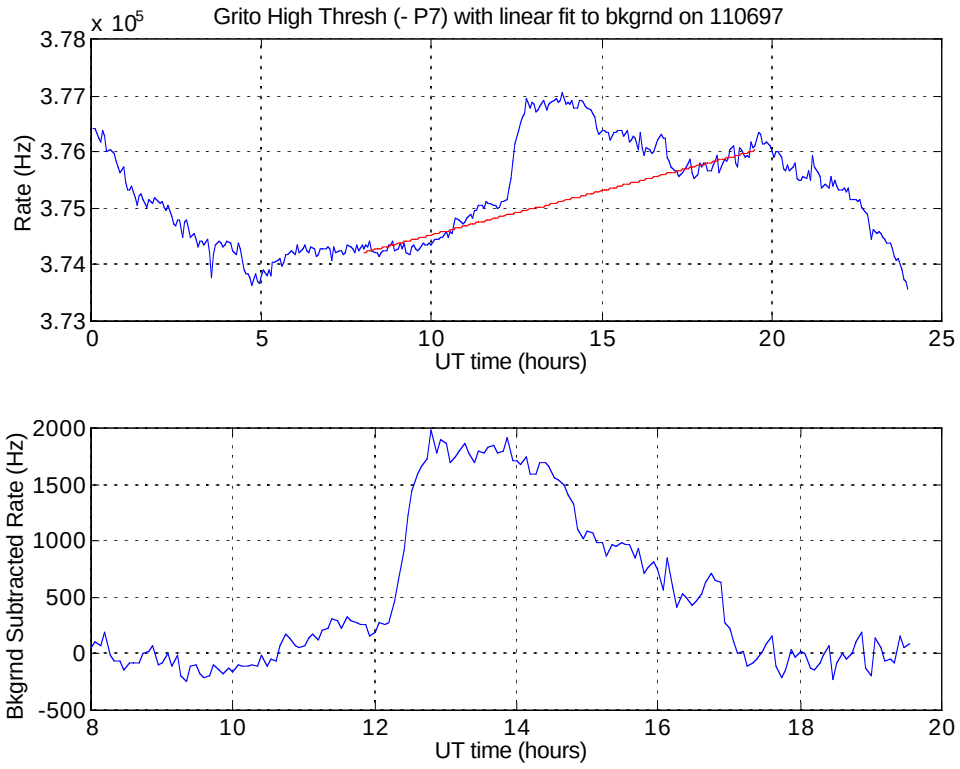


Figure 5.5 - The top panel shows the Milagrito high threshold scaler rate along with a linear fit to the background directly preceding and following the event. To first order, it can be seen that this linear fit does a fairly good job of estimating the daily variation during this time period. The bottom panel shows the background subtracted rate for the time immediately surrounding the event. Notice the different scales for the horizontal axis in the two plots.

detector than those available during Milagrito's lifetime, are necessary to make corrections that are more useful than the rough estimate shown in the figure. This does not present a problem for the analysis of the relatively fast event onset shown in this work, but it unfortunately, does not allow for an accurate estimate of the event duration. There is another effect during this event, described below,

that makes an accurate estimate of the event duration even more difficult to attain.

We note that the scaler rate plotted in **figure 5.4** does not include one of the 15 patches of the detector. This historically noisy group of PMTs, located within patch 7, exhibited an unrelated instrumental rate increase a few hours after the onset of the CME related rate increase. The difference between the rate increase with and without patch 7 can be seen in **figure 5.6**. This type of instrumental rate increase (referred to as "high-rate flashing" and thought to be

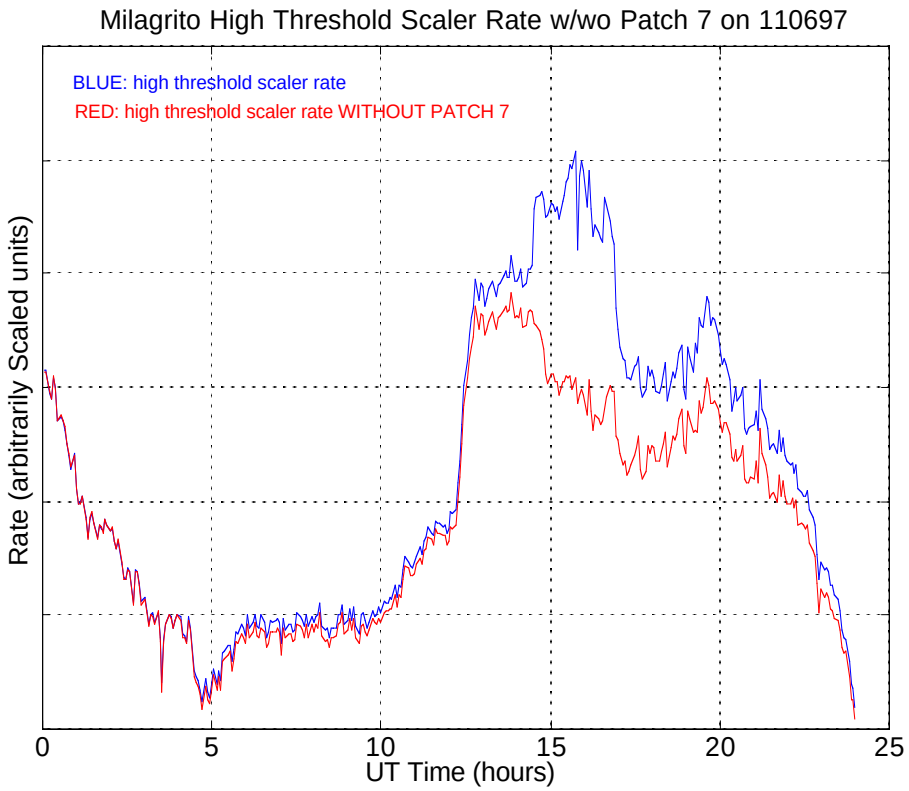


Figure 5.6 - Milagrito high threshold scaler rate on the 6 November 1997, with and without the scaler counts from patch 7 included in the sum. It can be seen that the high rate "flashing" that ocurred within patch 7 resulted in a rise in the total scaler rate at about 14:30 UT. The daily variation of rate can also be seen in this plot. These two effects conspired to make it difficult to estimate the duration of this event, but they did not significantly effect the estimation of the onset time.

caused by arcing in the base of the PMT or light emission in the tube itself) is common in some clusters of PMTs, but it can be identified and corrected based on its localized spatial characteristic. A high-rate flasher will cause a disproportionate rate increase in a local cluster of PMTs, but an air shower signal will cause a more uniform increase over the entire pond. High-rate flashing can cause scaler rate increases that are comparable in magnitude to the rate increase from the 6 November event, but they are localized to the area of the flashing PMT. Typically, the rate increase from the flashing can be attributed to only one patch, with a smaller increase in patches within the immediate vicinity of the culprit PMT. An example of a high-rate flasher increase was observed in patch 7 at ~14:30 UT on the day of the event, well after the onset of the SEP related increase (see **figure 5.6**). This patch of PMTs was known to exhibit such behavior over much of Milagrito's lifetime. During the rate increase that began shortly after 12:00 UT on 6 November 1997, all of the patches except for patch 7 experienced a uniform rate increase with an average increase of 0.48% and a standard deviation of 0.08%. Patch 7 experienced a rate increase of 1.1%. After studying the uniformity of the signal over the pond in this way and analyzing the instrument's behavior over its lifetime as described in the preceding paragraph, we concluded that most of this instrumental increase could be attributed to patch 7 and that the remaining rate increase was of solar origin.

## 100 PMT Mode Observations

The 100 PMT shower trigger rate also experienced an increase, although the significance was not as great as that in scaler mode. The magnitude of the rate increase signal to background fluctuations in 100 PMT mode was ~10% of that in the scaler mode. We expected that the 100 PMT mode would have a smaller response to an event such as this, since this mode has a higher threshold energy and has less effective area. It is not yet clear which of several possible mechanisms initiated the signal in the 100 PMT mode, so the detector's sensitivity to several possible mechanisms has been investigated. Some of the explanations for the shower mode "signal" that have been considered are isotropic proton primaries (such as those that caused the high threshold scaler increase, but with much higher energies), instrumental effects known as "flashing" PMTs, and high zenith angle muons. The magnitude of these effects influences the systematic errors in the analysis.

The 100 PMT mode provides data that is nominally more stable than that of the scaler mode. In spite of this, there are some effects that can lead to a misinterpretation of the 100 PMT mode data, while not causing an effect in the scaler mode that will be significant relative to its larger background. If a mechanism for triggering the 100 PMT mode that is not modeled by the effective area curves in figure 4.8, such as those to be listed in the following paragraphs, is present then it may lead to a small event rate increase of ~5 Hz. While this increase may appear significant in the 100 PMT mode, the corresponding rate increase in the high threshold scaler mode, which may be ~50 Hz, will not be

significant over the much larger background of the scaler mode. With this in mind, several potential mechanisms and instrumental effects have been considered with regard to the 100 PMT mode "signal."

This signal does not appear to conform to known instrumental effects, such as “flashing” PMTs. Flashers, which are caused by light emission at the base and / or in the tube of the PMT, are a common problem with water Cherenkov detectors. There are three known forms of flashers in the Milagrito data that could, in theory, contribute to the 100 PMT signal.

One of these forms of flashers is referred to as a "high PE, low $N_{fit}$" flasher. This type of flasher, which typically does not lead to high scaler rates, is characterized by particularly high photoelectron hits in individual PMTs. These flashers tend to present themselves in the data with a low number of PMTs that are useable in the fitting procedure (i.e. low $N_{fit}$), and they tend to dissapear completely if an $N_{fit}$ cut of 40 PMTs is applied (McEnery et al. 1999, McCullough et al. 1999). This type of flasher is not present at anytime during the event.

Another form of flasher is referred to as a "high PE, high $N_{fit}$" flasher. This phenomenon may actually be a result of mis-calibration of individual PMTs, rather than an actual flashing in the PMT itself. Like the previous form, these flashers typically do not lead to high scaler rates, and they are characterized by particularly high photoelectron hits in individual PMTs. The difference is that these flashers continue to appear in the data with a high value for $N_{fit}$. This form of flasher is present during the onset of the event, but this flashing is present before and after the event as well. Since the flashing, or possible calibration effect, remains constant prior to and throughout the event, it cannot be responsible for the observed rate increase.

The third form of flasher, known as a high-rate flasher, is the same one that caused the high rate flashing in patch 7 that was discussed in the earlier section on the scaler mode observations. This type of flasher is not present in the 100 PMT mode during the onset of the event, although particularly high rate flashing that contributed to the scaler rate did occur several hours later within patch 7.

The 100 PMT mode effective area curve in **figure 4.8** represents the response of this operational mode of Milagrito to isotropic protons, but the simulated response does not include effects at high (>60˚) zenith angles. It is evident from this curve that particles of much higher energies (on the order of 100 GeV or greater) are needed to induce a response in this mode, as compared to the particle energies required for a trigger in the scaler mode. Although the 100 PMT mode increase could have been caused by isotropic, very high energy primaries (>100 GeV) such as those modeled, it is unlikely. Evidence for this can be found by looking at the quality of the air shower fit to a particular incident angle during the "event." Although 100 PMTs trigger the "100 PMT" air shower mode, not all of these PMTs are suitable to be used in the angular reconstruction, also known as "fitting" the event. For example, some PMTs may trigger significantly later or earlier than expected relative to others, thus giving the impression that there is no coherent shower plane. Individual PMTs that contributed disproportionately to the $\chi^2$ of the fit were not included in the fitting procedure. As an example of the criteria used, if a PMT contributes > 9 to the $\chi^2$ of the fit during the first iteration of the fitting procedure, then it is not used. For more detail on the fitting procedure, see Atkins et al. (2000). The events that

caused the shower mode increase on 6 Nov. 1997 all had a low number of PMTs that were suitable for the fitting procedure (see **figure 5.7**), and many events could not be fit at all. In **figure 5.7**, it is clear that there is no event rate increase if

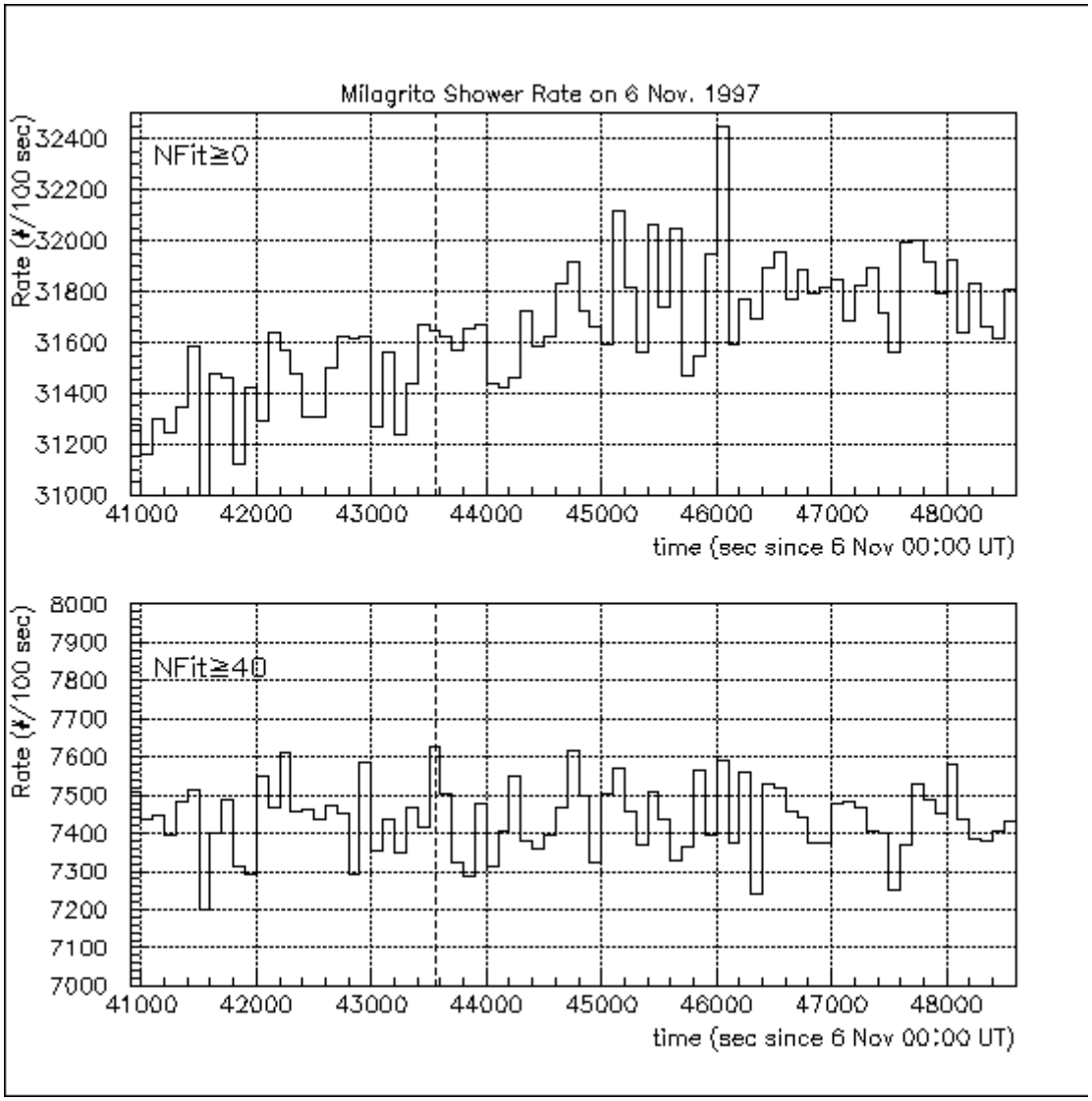


Figure 5.7 – Milagrito 100 PMT shower mode rate history at the time of the GLE. The top panel includes all events. The bottom panel, which displays no rate increase, includes only the events for which >39 tubes were suitable for use by the angle fitter. The dashed line is the event onset time according to the high threshold scalers.

it is required that 40 tubes are suitable to be usd in the fitting procedure. If this rate increase was due to an isotropic proton distribution, as that modeled between zenith angles of $0^{o}$-$60^{o}$, then greater numbers of "fittable" PMTs would

be expected since these events lead to "pancake-like" shower fronts, which have a characteristic time delay from one PMT to another. We also see (**figure 5.8**) that the fraction of events that cannot be fit increases as the event progresses. Furthermore, if this increase was due to isotropic protons, then a very hard spectrum ($P^{-2.5}$, with ~90% of the events from >200 GeV) is necessary to explain the increase. This spectrum would conflict with the spectrum inferred from the Milagrito high-threshold scaler rate increase, as well as neutron monitor and satellite data.

There is another potential mechanism by which primary protons can trigger the shower mode. High zenith-angle protons leading to secondary muons arriving from nearly horizontal directions could trigger the detector. These events were not simulated beyond $60^{o}$. The increase in the rate of "unfittable" events as the event progresses (**figure 5.8**) is evidence for high zenith-angle muons being the cause of the air shower "signal." Based on Monte Carlo events, we determined that the majority of "unfittable" events in the background rate could be attributed to muons from zenith angles > $83^{\circ}$, thus it is known that this mechanism can cause a trigger in the 100 PMT mode. However, the efficiency for converting a high-zenith-angle proton into a high-zenith-angle muon, which can subsequently trigger the 100 PMT mode, is not known. If horizontal muons contributed to this signal, they would be the result of high energy proton primaries (>30 GeV), based on estimates of muon losses in the atmospheric overburden above $83^{\circ}$, but the effective area curve in **figure 4.8** would not apply to this triggering mechanism. In order to determine the spectrum of the primary protons associated with this mechanism, extensive and

time consuming simulations, which require particle tracking through a multi-layered and spherical atmospheric model, will have to be completed.

Until more studies and simulations beyond 60˚ are performed, the details of the 100 PMT shower mode "signal" will not be known. Presently, the work on this 100 PMT "signal" remains inconclusive. Therefore, this analysis is restricted

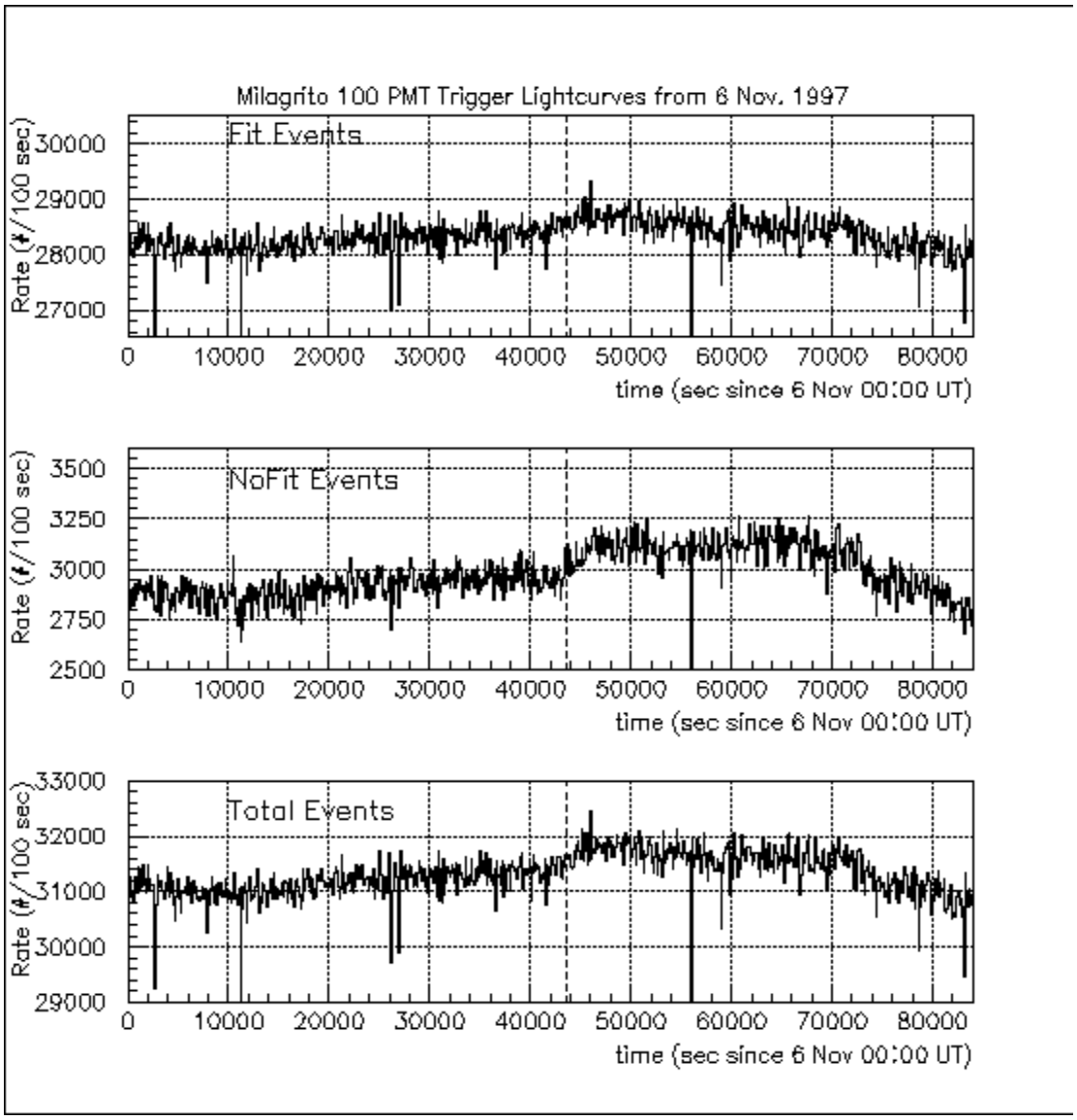


Figure 5.8 – Comparison of the 100 PMT mode time histories for fittable and unfittable events. It is apparent that the ratio of events that cannot be fit to events that can be fit increases during the time of the event. (The dashed line marks the onset according to the high threshold scalers.)

to the scaler rate increase, based on the belief that if the 100 PMT rate increase is of solar origin, it arises from a response characteristic of the instrument that has not been studied thoroughly. It is important to form the arguments in the previous paragraphs of this section in order to insure that there is no known inconsistency between the 100 PMT mode response and the scaler mode response, but any conclusions regarding the 6 November event must be based on the scaler mode analysis, which is well understood. Investigation of the instrument response to primary particles beyond 60˚, is planned.

## Proton Spectrum

Thus, using only the high-threshold scaler rate data of Milagrito, we can derive characteristics of the primary proton spectrum. We did this by folding a trial power law spectrum of protons through the response of the instrument. The trial power law spectrum is of the form:

$$f = C(P/P_o)^{-\alpha} ,$$

where $P$ is rigidity [GV] and $f$ is the differential proton flux [$m^{-2}$ $s^{-1}$ $sr^{-1}$ $GV^{-1}$]. The expected rate increase in the detector for a given $C$ and $\alpha$ is then found by integrating:

$$R = \int_{P_{cutoff}}^{\infty} f(P) A_{eff}(P) dP$$

The parameters of the trial spectra, C and $\alpha$, are then varied until a good fit to the measured rate increase is achieved. By only using the high-threshold scaler rate in this analysis, a range of acceptable values for $C$ and $\alpha$ was obtained. To

uniquely determine the parameters, another detector with a different response is necessary.

We made the assumption that the geomagnetic rigidity cutoff can be accurately represented by a single value, namely the vertical cutoff rigidity of 3.86 GV. This ignores any fluctuations in the planetary magnetic field, as well as the change in the cutoff at other zenith angles. Additionally, the pitch angle distribution of protons from the event is assumed to be isotropic. This is a reasonable assumption since it has been shown by other researchers (Lovell et al. 1999, Smart & Shea 1998) that the distribution was approaching isotropy by the time of maximum intensity, which is the time that is being analyzed here. During the onset of the event, at ~12:30 UT, the full-width-half-maximum (FWHM) of the pitch angle distribution was measured by Lovell et al. to be ~60˚, and by ~13:30, at which time the rate increase was on a plateau at maximum, the pitch angle distribution FWHM was ~105˚.

After obtaining the range of spectral parameters from the Milagrito data, we compared this to the spectrum obtained by the world wide network of neutron monitors. Neutron monitor data for this proton event, near the time of maximum intensity (~12:45-13:00 UT), indicate a rigidity power-law spectral index between approximately 5.2 and 6 in the 1-4 GV rigidity range (Duldig et al. 1999, Lovell et al. 1999). If the Milagrito derived range of spectral parameters for protons above 4 GV includes the neutron monitor spectrum at this rigidity and if an unbound power law above 4 GV is assumed, then a unique solution for the spectrum above 4 GV can be obtained. Doing this, we found that the spectral index, $\alpha$, that best fits the data is $9.0 \pm 2.3$. (The error bars for the spectral parameters are obtained by doing the above integral with the input parameters

modified by their 1σ error bars. The error is dominated by the error in the calculated effective area. Statistical errors from background fluctuations and errors arising from the fitting technique are also included, but the contribution from these error sources is insignificant compared to the effective area error.) The analysis leading to this spectral index assumes a single power law above 4 GV. We also performed the analysis with a hard upper rigidity cutoff in the proton spectrum. We varied this cutoff rigidity as a free parameter while extending the spectrum derived from the neutron monitors up into the energy


Figure 5.9 - Calculated differential flux of isotropic protons from the 6 November 1997 SEP event. Below ~4 GV, the neutron monitor derived flux spectrum is shown. Above ~4 GV, two possible spectra that are consistent with the Milagrito high threshold scaler rate increase are shown. One of these spectra involves a hard cutoff of the spectrum from lower energies, while the other curve is a broken power law. The actual spectrum is probably a gradual rollover of the rigidity power law. The circle is placed at the point where the neutron monitor and the Milagrito derived spectra were required to overlap.

range of Milagrito. In order for the Milagrito scaler data and the neutron monitor data to be consistent, the hard cutoff must occur at $4.7 \pm 0.5$ GV (error source as described above), if we assume that the $P^{-5.2}$ spectrum of Lovell et al. (1999) extends into the energy range of Milagrito.

Both of the cases described above are shown in **figure 5.9**. These results provide evidence for a cutoff or a rollover in the spectrum in the transition region between the neutron monitors and Milagrito. This is most likely of the form of a progressive spectral softening throughout the energy region above ~1 GeV.

## Event Timing

Prior to the detection of energetic particles at Earth, X-rays and gamma rays were detected by space-based instruments, and the CME-associated solar flare was categorized as X9. Yoshimori et al. (2000) reported the detection of gamma rays up to 100 MeV, with an onset time of 11:52 UT for the 10-20 MeV emission, based on Yohkoh data. **Figure 5.10** shows the onset and the completion times of this emission on a plot with the Milagrito high threshold scaler rate and the Climax neutron monitor rate for comparison. Several nuclear lines were present in the count spectrum derived from Yohkoh data, including the neutron capture line and C and O deexcitation lines. It is clear that proton acceleration was occurring at the flare site for a short period of time following 11:52 UT. The gamma ray event, as measured with Yohkoh, was over within five minutes of onset.

The time profile measured by Milagrito is consistent with that of Climax, when allowances are made for the long-term, background meteorological fluctuations (**Figures 5.4 and 5.5**). The onset of the Milagrito scaler rate enhancement, which was at 12:07 UT +/- 6 min, was simultaneous within error with the Climax neutron monitor onset time, which occurred at approximately 12:06 UT. The times of maximum intensity and the duration are also similar.

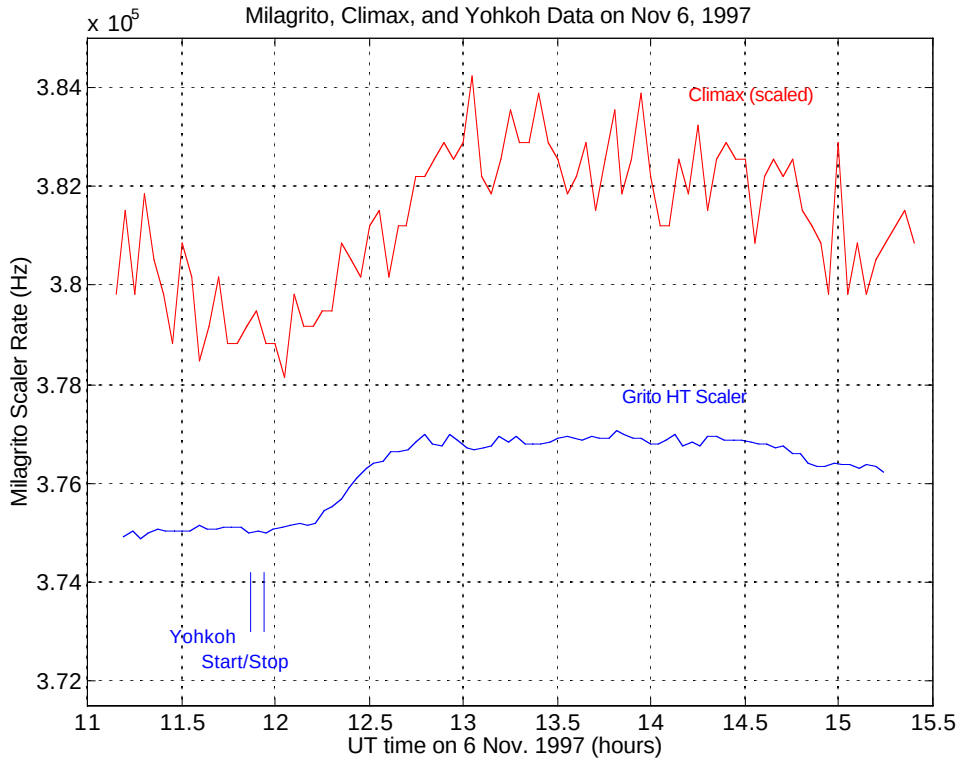


Figure 5.10 – Onset of the Milagrito high threshold scaler rate increase and the Climax rate increase, with lines marking the beginning and end of the Yohkoh γ-ray line observations for comparison.

The rate increase in Milagrito's scalers reached its maximum value at 12:44 UT ± 6 min. The GOES satellite observed an enhanced rate of protons from this event at about the same time. The >100 MeV proton emission detected by the GOES satellite lasted more than two days. GOES also detected protons from an event

that occurred on 4 November. While the >100 MeV protons had returned to their pre-disturbance flux by the time of the 6 Nov. event, the >10 MeV flux of protons was still elevated over background by ~10x, relative to its value prior to the 4 November event.

## Discussion and Conclusions Regarding 6 Nov. 1997 Event

When the short duration (~5 min) of the gamma ray line emission and the long duration (~hours to ~days, depending on energy) of the high energy proton acceleration are considered, it appears as though much of the proton acceleration does not occur in the flare itself. Protons do appear to be accelerated at the flare site during the impulsive phase, but the GeV protons, which come later, probably originate in the low corona. If a CME-driven shock was responsible for the GeV protons, then the height of the CME at the time at which protons reached these high energies can be estimated by looking at the difference in time between the gamma ray onset and the GLE onset, while accounting for the proton path length along the Parker spiral of the interplanetary magnetic field. The path length for protons is defined by the spiral IMF, which is a function of solar wind velocity, $V_{SW}$, and the angular speed of the Sun, $\Omega$. The path length, $S$, from a heliographic latitude defined by $\Lambda$ is given by Lockwood et al. (1990) as:

$$S = \frac{r\sqrt{1+\alpha r^2}}{2} + \frac{\ln\left[\alpha r + \sqrt{1+\alpha^2 r^2}\right]}{2\alpha},$$

where r is the radial distance to the observation point, and $\alpha \equiv (\Omega \cos\Lambda)/V_{sw}$.

Thus, a path length of 1.1±0.05 AU from the region around the flare site to Earth during the time of the 6 Nov 1997 event is expected, if any IMF disturbances are neglected (the error bars arise from the 1σ error bars in the input parameters, which means that kinks in the field lines and fluctuations of the magnetic field are neglected). The path length can also be affetcted by the pitch angle distribution of the particles. The path length calculation shown above does not account for the spiral path of a particle with a non-zero pitch angle. This tends to scale the path length by $(\cos \theta)^{-1}$. For instance, the path length would be double the parker spiral value for a particle with a pitch angle of 60˚. Although the event exhibited some anisotropy in its early stages, it has already been stated that Lovell et al. (1998) found that the FWHM was ~60˚ at this time However, the onset time of the event is determined by the earliest arriving particles, which were the ones with small pitch angles that were beamed along the IMF line. This leads to an estimate of ~10-20 minutes for the acceleration time of the >4 GV protons. After this amount of time, assuming a CME leading edge speed of ~1600 km / s, the leading edge of the CME was at ~2-4 solar radii. This spatial scale is reasonable, and it is consistent with prior results on GeV ion acceleration heights found for the 24 May 1990 CME event studied by Lockwood et al. (1999) and the September 1989 event studied by Kahler (1992). In these studies, which made use of similar timing arguments, particle injection heights were calculated to be ~2 solar radii and ~2.5-4 solar radii, respectively. An acceleration time of ~10 minutes for ~1-10 GeV protons is consistent with the collisionless shock model of Lee & Ryan (1986), when injection energies of ~10 MeV are present. In this model, the ratio of injection energy to accelrated particle energy as a function

of time was calculated. While this is a simple blast wave model, similar driven shock models could be applied (e.g. Lee 1997). Based on GOES data, there was an abundance of >10 MeV protons that continued to occupy interplanetary space due to the 4 November solar event. These ambient energetic protons could have provided the >10 MeV injection energies needed by the propagating CME-driven shock. While this does present a consistent interpretation, it is not definitive.

Between 10 and 60 MeV, the instruments on board the ACE satellite observed a proton spectrum of the form $E^{-2.1}$ (Cohen et al. 1999), while at higher energies, ground-based instruments observed much softer spectra. The Milagrito data, combined with neutron monitor data, leads to a proton spectrum with a rigidity power law spectral index of $9.0 \pm 2.3$, if a single power law is assumed above ~4 GV. A continuation of the $P^{-5.2}$ spectrum from Lovell et al. (1999) with a hard cutoff is also possible. These spectra are, by construction, continuous with the spectrum derived from the world wide neutron monitor network at 4 GV. In any case, the spectra derived from Milagrito and neutron monitor data provide evidence for a gradual rollover or a cutoff somewhere in Milagrito's sensitivity range above ~4 GV.

This steepened high energy spectrum is also consistent with a low corona origin based on the implied shock strength. For a differential rigidity power law spectral index of $9.0 \pm 2.3$ for relativistic protons to result from diffusive shock acceleration, one must have a shock compression ratio of ~1.2. For a fast CME, such as this, to drive a shock with this low compression ratio, the Alfven speed in the local medium must be relatively high. This shock compression ratio implies an Alfven speed on the order of 500-1000 km / s. This is on the high end of that

expected in the solar corona. This implies that the acceleration occurred low in the corona where the magnetic field and the Alfven speed were large. This is consistent with the timing arguments presented above for a low coronal origin. Once again, this presents a consistent picture, yet it is not definitive. It is also possible that the spectrum could be steepened by a transport effect after the diffusive shock acceleration occurs or that an unidentified alternative source could produce this steep spectrum.

# CHAPTER 6

## CONCLUSIONS AND THE FUTURE

Observations with Milagrito have contributed to the understanding of the 6 November 1997 SEP event, and by doing so, Milagrito has demonstrated the utility of the water-Cherenkov detection technique. The conclusions regarding the 6 November 1997 event presented in the last chapter provide an enhanced understanding of the processes that lead to SEP acceleration. In particular, Milagrito has made observations at the extreme end of the energy spectrum which have identified the source location and provided compelling evidence for the mechanism of CME-driven shock acceleration. The observation of this event with Milagrito has provided a detection of a cutoff, or a rollover, in the energy spectrum of SEPs at the highest detectable energies. While measurements of an event during the last solar maximum in September of 1989 with underground muon telescopes provided evidence for a cutoff (Lovell et al. 1998), Milagrito has used a new technique with a significantly increased effective area relative to both muon telescopes and neutron monitors. Due to this increased area, Milagrito was able to unambiguously detect the 6 November event and provide evidence for the existence of a spectral softening, rather than simply providing an upper limit measurement. Milagrito was the world's first EAS particle detector sensitive below 1 TeV, and these findings are indicative of the abilities of the water-cherenkov technique used by Milagrito. This technique will continue to be utilized by the full-scale Milagro detector.

The Milagro instrument, for which Milagrito was a prototype, is currently taking data. With its increased number of PMTs, multiple layer design, and increased effective area, Milagro may provide exciting results in the future. There are already some preliminary results that indicate the detection of several Forbush decrease events in the Milagro data, as well as at least one SEP event in April 2001.

The second layer of PMTs, as shown in **figure 6.1**, can give Milagro the ability to reconstruct the directions of single muons and small showers in the pond. In the future, this second layer could also be used to incorporate advanced triggerring mechanisms. By using the pulse height information on the bottom layer of the pond, one can identify the penetrating muons. Timing information can then be used to reconstruct the incident direction of these muons. This technique will lower the energy threshold for reconstructable events. Proposed enhancements to the data acquisition system, which would allow Milagro to record this higher rate data and reconstruct hadronic events down to primary energies of ~3 GeV, can increase Milagro's capabilities. This proposed higher-rate DAQ system would enhance Milagro's baseline mode as well as its ability to study solar energetic particles (Ryan et al. 2000).

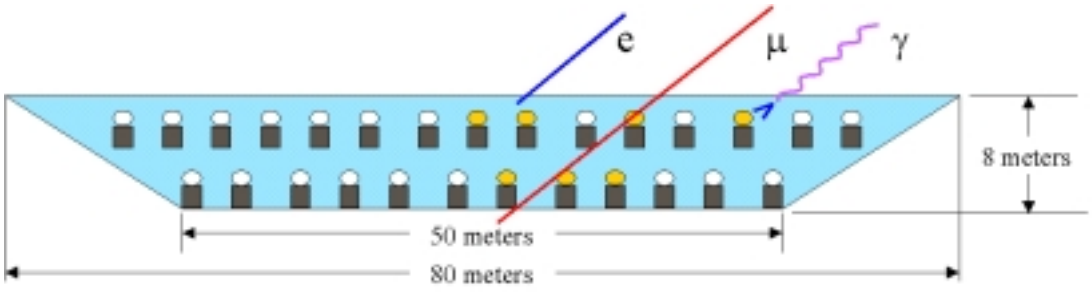


Figure 6.1 - Cross-sectional view of the Milagro PMT layout.

Other changes that have been made to Milagro are the number of PMTs and the addition of baffles that now surround each PMT. The number of PMTs has been increased to 723, and the area of the air shower layer has been increased. This results in an increase in the effective area. Each PMT in Milagro has a collar-like baffle around its base. This reflective baffle is designed to reduce light that has scattered and reflected throughout the pond. It should reduce effects of late light in the PMT, and it should also minimize the cross-talk between PMTs. As a result, the problems associated with flashers should be minimized in Milagro. Additionally, each PMT base now has a black cover, which should reduce any flashing that may arise from arcing in the base of the tube. The actual effects of these measures should be evaluated with the data from Milagro.

Another major difference between Milagro and Milagrito is the philosophy that governs their operations. Although Milagrito took useful data, it was a prototype that operated as an engineering test bed. This means that the configuration of the detector was frequently changed, and stable operation was not the primary concern. On the other hand, Milagro is being operated with a philosophy that places a high priority on live-time and stable operation. This should allow for more consistent data that can be interpreted with more ease, relative to Milagrito. Additionally, this stable operation should allow for one to study variations of scaler and trigger rates on a variety of timescales. The diurnal and meteorological fluctuations, as well as possible seasonal variations, should be relatively straight-forward to evaluate due to the constant configuration of Milagro relative to that of Milagrito. That is not to say that this

work will be easy since new and mysterious variations will almost certainly present themselves.

Other work that can enhance Milagro's ability to study SEP and cosmic ray variations will be the calculation of more detailed instrument response curves. Due to the inability of Corsika to track particles through the more complex atmospheric model required above zenith angles of 60˚, the current Milagrito effective area curves rely on an extrapolation at these high zenith angles. By using updates to Corsika, or exploring alternative Monte Carlo simulation options, the calculation of the effective area can be significantly improved. The extension to higher zenith angles will also allow one to analyze the response of the instrument to effects particular to this zenith angle range, such as high zenith-angle muons.

Additionally, faster processing time will allow for more calculations at low energies, which are critical to analysis of SEPs and cosmic rays at energies of a few GeV. With more calculations at low energies and a variety of zenith angles, the effects of atmospheric attenuation on the lower energy limits of the effective area should present themselves. Additional calculations of the geomagnetic effects can also be carried out to further the understanding of Milagro's response at its lowest detection energies. The analysis presented in this thesis relied on the vertical cutoff rigidities, but the cutoff rigidity is actually a function of zenith angle at the site location. This additional knowledge regarding atmospheric and geomagnetic effects should lead to a greater understanding of the low energy response of Milagro.

By combining the enhanced hardware configurations and operational stability of Milagro with additional calculations, the currently operating detector

should provide interesting contributions to our understanding of SEP acceleration and cosmic ray propogation in the heliosphere.

## References


Aid, S., et al. 1995, Z. Phys. C, **69**, 27.

Atkins, R., et al. 2000, *Nuclear Instruments & Methods in Physics Research A*, **449**, 478.

Auger, P. 1939, *Rev. Mod. Phys.*, **11**, 288.

Biermann, L. 1951, *Z. Astrophys.*, **29**, 274.

Carmichael, H. 1964, Cosmic Rays, IQSY Instruction Manual No. 7, IQSY Secretariat, London.

Carrington, R.C. 1860, *Monthly Notices Royal Astron. Society*, **20**, 13.

CERN Application Software Group 1994, CERN W, 5013, Version 3.21.

Chapman, S. 1957, *Smithsonian Contrib. Astrophys.*, **2**, 1.

Chapman, S. 1950, *Journ. Geophys. Res.*, **55**, 361.

Chiba, N., et al. 1992, *Astroparticle Physics*, **1**, 27.

Cliver, E.W. 1996, *High Energy Solar Physics*, AIP Conf. Proc. 374, ed. Ramaty, R., Mandzahavidze, N., & Hua, X.-M., AIP Press, New York, 45.

Cliver, E.W., Kahler, S.W., McIntosh, P.S. 1983, *Astrophys. Journ.*, **264**, 699.

Cohen, C.M.S., et al. 1999, *Geophys. Res. Lett.*, **26**, 149.

Cronin, J.W., Gibbs, K.G., & Weekes, T.C. 1993, *Ann. Rev. Nuc. & Particle Sci.*, **43**, 883.

Cummings, A.C. & Stone, E.C. 1998, *Space Science Reviews*, **83**, 51.

Debrunner, H. 1994, in *AIP Conf. Proc. # 294: High Energy Solar Phenomena*, Ryan, J.M. & Vestrand, W.T. eds., AIP Press, New York.

Duldig, M.L. and Humble, J.E. 1999, in *Proc. XXVI Int. Cosmic Ray Conf*, **6**, 403.

Falcone, A.D., et al. 1999, *Astroparticle Physics*, **11**, 283.

Fermi, E. 1949, Phys. Rev., **75**, 1169.

Forbush, S.E. 1946, Phys. Rev. Lett., **70**, 771.

Fowler, G.N., Wolfendale, A.W., and Flugge, S., eds. 1961, *Cosmic Rays I.*

Gosling, J.T. 1993, Journ. of Geophys. Res., **98**, 18937.

Greisen, K. 1966, Phys. Rev. Lett., **16**,748.

Hale, G.E. 1931, *Astrophys. Journ.*, **73**, 379.

Hayakawa, S. 1969, *Cosmic Ray Physics* (New York: John Wiley and Sons).

Heck, D. 1999, *private communication*.

Heck, D., et al. 1998, *Corsika: A Monte Carlo Code to Simulate Extensive Air Showers*, Forschungszentrum Karlsruhe Report FZKA 6019.

Hess, V.F. 1913, Phys. Z., **13**, 1084.

Hillas, A.M. 1972, *Cosmic Rays*, Pergamon Press, Oxford.

Hoffman, C.M., Sinnis, C., Fleury, P., & Punch, M. 1999, *Rev. Mod. Phys.*, **71**, 897.

Hudson, H. & Ryan, J. 1995, *Ann. Rev. Astron. & Astrophys.*, **33**, 239.

Hundhausen, A. 1999, in *The Many Faces of the Sun: A Summary of Results from NASA's SMM*, Strong, K., Saba, J.L.R., Haisch, B.M., et al., eds. (New York: Springer Verlag), 143.

Kahler, S.W. 1994, *Astrophys. J.*, **428**, 837.

Kahler, S.W. 1992, Ann. Rev. Astron. & Astrophys., **30**, 113.

Kahler, S.W., Cliver, E.W., Cane, H.V., et al. 1987, *Proc. XX Int. Cosmic Ray Conf.*, **3**, 121.

Kahler, S.W., Sheeley, N.R., Jr., Howard, R.A., et al. 1984, *Journ. Geophys. Res.*, **89**, 9683.

Kahler, S.W., Hidner, E., & Van Hollebeke, M.A.I. 1978, *Solar Phys.*, **57**, 429.

Lee, M.A. 1997, in *American Geophys. Union Monograph 99: Coronal Mass Ejections*, eds. Crooker, N., Joselyn, J., & Feynman, J., 227.

Lee, M.A., and Ryan, J.M. 1986, *Astrophys. J.*, **303**, 829.

Lin, R.P., & Hudson, H.S. 1976, *Solar Phys.*, **50**, 153.

Linsley, J. 1983, Proc. 18$^{th}$ Internat. Cosmic Ray Conf. (Bangalore), **12**, 135.

Lockwood, J.A., Debrunner, H., & Ryan, J.M. 1999, Astroparticle Phys., **12**, 97.

Lockwood, J.A. & Debrunner, H. 1999, Space Science Reviews, **88**, 483.

Lockwood, et al. 1990, *Astrophys. Journ.*, **355**, 287.

Longair, M.S. 1992, *High Energy Astrophysics, 2nd Ed.*, Vol 1, Cambridge Univ. Press, Cambridge.

Lovell, J.L., et al. 1999, *Adv. Space Res.*

Lovell, J.L., Duldig, M.L., Humble, J.E. 1998, *Journ. of Geophys. Research*, **103**, 23733.

Mason, G.M., et al. 1999, *Geophys. Res. Lett.*, **26**, 141.

McEnery, J., et al. 1999, *internal Milagro Collaboration Memo.*

McCullough, J.F., et al. 1999, in *Proc. XXVI Int. Cosmic Ray Conf.*, **2**, 369.

McCullough, J.F. et al. 1999, *internal Milagro Collaboration Memo.*

Medina-Tanco, G. 2001, Astrophys. Journ., **549**, 711.

Meyer, P., Parker, E.N., & Simpson, J.A. 1956, Phys. Rev., **104**, 768.

Mobius, E, et al. 1999, *Geophys. Res. Lett.*, **26**, 145.

Newton, H.W. 1943, *Monthly Notices Royal Astron. Society*, **103**, 244.

Ong, R. 1998, *Phys. Rep.*, **305**, 93.

Pallavicini, R., Serio, S., & Vaiana, G.S. 1977, *Astrophys. Journ.*, **216**, 108.

Parker, E.N. 1957, *Physical Review*, **107**, 830.

Reames, D.V. 1999, Space Science Reviews, **90**, 413.

Robinson, R.D., Stewart, R.T., Sheeley, N.R. Jr., et al. 1986, *Solar Phys.*, **105**, 149.

Ryan, J.M. et al. 2000, in *AIP Conf. Proc. 528: Acceleration and Transport of Energetic Particles Observed in the Heliosphere*, eds. Mewaldt, R.A., et al., 197.

Ryan, J.M. et al. 1999, in *Proc. of the XXVI International Cosmic Ray Conf.*, **6**, 378.

Sheeley, N.R., Jr., Howard, R.A., Koomen, M.J., et al. 1983, *Astrophys. Journ.*, **272**, 349.

Sheeley, N.R., Jr., Bohlin, J.D., Brueckner, G.E., et al. 1975, *Solar Phys.*, **45**, 377.

Simpson, J.A. 1983, Ann. Rev. Nucl. Part. Sci., **33**, 330.

Simpson, J.A. 1957, Ann. I.G.Y., part 7, Pergamon Press, London.

Simpson, J.A. 1948, Phys. Rev., **73**, 1389.

Smart, D.F. & Shea, M.A. 1998, in *Proc. Spring American Geophys. Union Mtg.*

St. Cyr, C. 2001, *private communication*.

Torsti, J. et al. 2000, Astrophys. Journ., **544**, 1169.

Webber, W.R. 1983, in *Composition and Origin of Cosmic Rays*, Shapiro, M.M. ed., Dordrecht Reidel, Dordrecht.

Weekes, T.C. 1996, *Space Science Reviews*, **75**, 1.

Weekes, T.C., et al. 1989, *Astrophys. Journ.*, **342**, 379.

Williams, D., et al. 1998, *internal notes Milagro Collaboration Meeting (October)*.

Yoshimori, M., et al. 2000, in *AIP Conf. Proc. 528: Acceleration and Transport of Energetic Particles Observed in the Heliosphere*, eds. Mewaldt, R.A., et al., 189.

Zatsepin, G.T. & Kuzmin, V.A. 1966, Soviet Phys. - JETP Lett., **4**, 78.